

THREE DIMENSIONAL CRYSTALLINE SILICON SOLAR CELLS

A THESIS SUBMITTED TO  
THE GRADUATE SCHOOL OF NATURAL AND APPLIED SCIENCES  
OF  
MIDDLE EAST TECHNICAL UNIVERSITY

BY

GÜLSEN BAYTEMİR

IN PARTIAL FULFILLMENT OF THE REQUIREMENTS  
FOR  
THE DEGREE OF DOCTOR OF PHILOSOPHY  
IN  
PHYSICS

DECEMBER 2018



Approval of the thesis:

**THREE DIMENSIONAL CRYSTALLINE SILICON SOLAR CELLS**

submitted by **GÜLSEN BAYTEMİR** in partial fulfillment of the requirements for the degree of **Doctor of Philosophy in Physics Department, Middle East Technical University** by,

Prof. Dr. Halil Kalıpçılar  
Dean, Graduate School of **Natural and Applied Sciences**

\_\_\_\_\_

Prof. Dr. Altuğ Özpınece  
Head of Department, **Physics**

\_\_\_\_\_

Prof. Dr. Raşit Turan  
Supervisor, **Physics, METU**

\_\_\_\_\_

**Examining Committee Members:**

Prof. Dr. Ayşe Çiğdem Erçelebi  
Physics, Middle East Technical University

\_\_\_\_\_

Prof. Dr. Raşit Turan  
Physics, Middle East Technical University

\_\_\_\_\_

Prof. Dr. Hamit Topuz  
Industrial Engineering, Maltepe University

\_\_\_\_\_

Assoc. Prof. Dr. Alpan Bek  
Physics, Middle East Technical University

\_\_\_\_\_

Assist. Prof. Dr. Tunay Tansel  
Institute of Nuclear Sciences, Hacettepe University

\_\_\_\_\_

Date: 28.12.2018

**I hereby declare that all information in this document has been obtained and presented in accordance with academic rules and ethical conduct. I also declare that, as required by these rules and conduct, I have fully cited and referenced all material and results that are not original to this work.**

Name, Surname: Gülsen Baytemir

Signature:

## ABSTRACT

### THREE DIMENSIONAL CRYSTALLINE SILICON SOLAR CELLS

Baytemir, Gülsen  
Ph.D., Department of Physics  
Supervisor: Prof. Dr. Raşit Turan

December 2018, 148 pages

Three-dimensional crystalline silicon solar cells have been attracting attention with its remarkable electrical and optical performance. In this geometry, nano/micropillars allow minority carrier collection in the radial direction and shorten the path length of the photogenerated carriers. Furthermore, with appropriate geometry of the pillars the solar cell efficiency is enhanced due to the reduced surface reflectance and increased light harvesting.

Throughout this study, metal assisted etching (MAE), a top-down method was applied through photolithography to fabricate micropillars. Firstly, radial junction cells with different micropillar lengths, including the longest  $\sim 6 \mu\text{m}$ , were fabricated by applying different etching durations. The maximum efficiency value, 15.90 %, was obtained from the cell with longest micropillars since with the increase in pillar length, higher  $J_{sc}$  values were obtained due to the reduced surface reflection and higher junction area.

Radial and planar junction solar cells were then fabricated using Si wafers contaminated with Au impurities having U-shape diffusion profile in Si. The efficiencies of the radial junction solar cells, which allow photogenerated carriers to

be collected over shorter distances, were less affected by contamination than planar junction solar cells. This is consistent with the expectation that the cells with radial geometry are less sensitive to the quality of the material used.

Moreover, the solar cells with different thicknesses were fabricated to increase the proportion of the region containing micropillars in the cell and to reduce the fabrication cost by allowing the use of thin Si substrates. Firstly, longer micropillars were obtained by increasing HF concentration in the MAE solution to suppress the lateral etching and instead of H<sub>2</sub>O, using ethanol which has a lower surface tension to obtain smoother etching. The efficiency value of 17.27 %, one of the highest efficiency values in radial junction cells, was obtained from the cell containing 11.5 μm micropillars. By decreasing the thickness of the cells, it was observed that the efficiency values were less affected in three dimensional solar cells than in planar junction cells due to less decrease in V<sub>oc</sub> and J<sub>sc</sub> values.

Keywords: Radial p-n Junction, Metal Assisted Chemical Etching, Photolithography, Metal Contamination, Thin Si Solar Cells

## ÖZ

### ÜÇ BOYUTLU KRİSTAL SİLİSYUM GÜNEŞ HÜCRELERİ

Baytemir, Gülsen  
Doktora, Fizik  
Tez Danışmanı: Prof. Dr. Raşit Turan

Aralık 2018, 148 sayfa

Üç boyutlu kristal silisyum güneş hücreleri, dikkate değer elektriksel ve optik performansıyla ilgi görmektedir. Bu geometride, nano/mikro sütunlar, fotojenlenmiş taşıyıcıların radyal doğrultuda, daha az mesafe katederek toplanabilme olasılığı artırılır. Ayrıca, uygun geometride sütunların tasarımıyla, yüzey yansımalarının azalması ve ışık Emilimi artırılması sağlanarak hücredeki verimlilik yükseltilir.

Bu çalışmada boyunca, Si mikro sütunların üretimi için yukarıdan aşağıya bir yöntem olan metal destekli aşındırma (MAE), fotolitografi yardımı ile uygulanmıştır. İlk olarak, farklı aşındırma zamanları uygulanarak, en uzun  $\sim 6$   $\mu\text{m}$  sütunlar içeren, farklı sütun uzunluklarında radyal eklem güneş hücreleri üretilmiştir. Sütun uzunluğundaki artmayla birlikte, azalmış yüzey yansıması ve daha uzun eklem alanı nedenleriyle daha yüksek Jsc değerleri elde edildiğinden en yüksek verimlilik değeri olan % 15.90, en uzun sütunlar içeren hücreden elde edilmiştir.

Sonrasında, Si içerisinde U şeklinde difüzyon profiline sahip Au ile kontamine edilen Si pullar kullanılarak hücreler üretilmiştir. Fotojenlenmiş taşıyıcıların daha kısa mesafe katederek toplanabilmesini sağlayan radyal geometrili hücrelerin verimlilikleri, düzlemsel hücrelere göre kontaminasyondan çok daha az

etkilenmişlerdir. Bu, radyal bir geometriye sahip hücrelerin malzemenin kalitesine daha az duyarlı olması beklentisiyle uyumludur.

Ayrıca, mikro sütunların oluşturduğu bölgenin oranını artırmak ve ince silisyum kullanımına olanak sağlanmasıyla maliyeti azaltmak amacıyla farklı kalınlıklarda hücreler üretilmiştir. MAE çözeltisi içerisindeki HF konsantrasyonu artırılarak yanal aşındırma, H<sub>2</sub>O çözücüsü yerine yüzey gerilimi daha düşük olan etanol kullanılarak daha pürüzsüz bir aşındırma sağlanmıştır. ~11.5 µm sütunlar içeren hücrelerden, bilinen en yüksek değerlerinden olan % 17.27 değerinde hücre verimi elde edilmiştir. Hücrelerin kalınlığının azaltılmasıyla, üç boyutlu hücrelerde, düzlemsel hücrelere kıyasla, Voc ve Jsc değerlerindeki azalışın çok daha az olmasından dolayı verimlilik değerlerinin daha az etkilendiği gözlemlenmiştir.

Anahtar Kelimeler: Radyal p-n Eklemi, Metal Destekli Kimyasal Aşındırma, Fotolitografi, Metalik Kontaminasyon, İnce Si Güneş Hücreleri



*To the memory of my beloved sister...*

## ACKNOWLEDGMENTS

First of all, I would like to express my sincere gratitude to my supervisor Prof. Dr. Raşit Turan for the continuous support of my Ph.D study and related researches, for his patience, motivation, and immense knowledge. His guidance helped me throughout the research and writing of this thesis. I could not have imagined having a better advisor and mentor for my Ph.D study. In addition to being a supervisor, he has a special place for me as the director of Center for Solar Energy Research and Applications (GÜNAM) where I have performed all the experiments of this Ph.D study.

Besides my supervisor, I would like to thank my thesis progress committee: Assoc. Prof. Dr. Alpan Bek and Assist. Prof. Dr. Tunay Tansel, for their insightful comments and encouragement, but also for the challenging questions which incentivized me to widen my research from various perspectives.

I would also like to extend my gratitude to my M.Sc. supervisor Prof. Dr. Osman Yılmaz who always supported me and guided me to join this group when I have completed my master studies and was trying to find a new direction for my future life.

In addition, I will never forget the assistance of Prof. Dr. Bayram Tekin during the Ph. D courses and qualifying exam. In my eyes, he will always be the instructor who is the best at teaching. Whenever I struggle with a question, I found myself in his office and he always tries to answer all my questions willingly.

I have to admit the fact that, in order to complete some of my experiments on time, for several nights, I have used the experimental equipment of Prof. Dr. Mehmet Parlak. Even after reading these words, I hope that he will continue to respond all my questions with sincerity. For that I am grateful.

I could not forget the assistance of Hande Çiftpınar for the processes involving some parts of my work. Many thanks to Olgu Demircioğlu, who lead me to work on the metallization line of GÜNAM, for the long days we have spent together on

metallization process. Also, I would like to thank Dr. Fırat Es; it is not possible to forget the sleepless nights and tiresome weekends we spent together in the lab.

I would like to thank Özden Başar Balbaşı, who is like a brother to me. Whenever I needed help, he has assisted me with his deep knowledge. Special thanks to my beloved friend and officemate Çiğdem Doğru for the times we have laughed together and being there for me at my worst.

I will never forget my time at METU Physics Department, where I have worked for 7 years as a teaching assistant. I would like to thank all the people I shared something with. I am deeply grateful to my previous talented officemates Assoc. Dr. İpek Koçer Güler and Dr. Fatma Acar Çakırca for their valuable friendship besides working together. How can I forget our department secretaries Gülşen Özdemir Parlak and Zeynep Lale Eke who are always there for me as sisters.

Dear Makbule Terlemezoğlu, you have a very special place in my heart as my first friend in GÜNAM. My kind-hearted friends, Dr. Pantea Aurang and Dr. Arezoo Hosseini, I miss you very much and thank you for your lovely friendship. Thanks to the members of the best newcomer band, the Impurities, Arman Aytaç, Salar Habibpur Sedani, Gence Bektaş for the lovely moments we have shared together. Thank you all for the things we have shared, Harun Tanık, Assoc. Dr. Mustafa Kulakçı, Dr. Mehmet Karaman, Ergi Dönerçark, Mustafa Ünal, Dr. Hasan Hüseyin Güllü, Dr. Mücahit Yılmaz, Dr. Bülent Arıkan, Dr. İsmail Kabaçelik, Cansu Emir, Dr. Hisham Nasser, Dr. Ihor Pavlov, Mona Zolfoghari Borra, Parisa Sharif, Nardin Avishan, Nasim Seyedpour, Behrad Radfar, Alp Ege Aytaç, Dr. Özge Bayraklı, Gamze Kökbudak, Beran Acar, Efe Orhan, Zeynep Demircioğlu, Ezgi Genç, Ozan Akdemir, Baran Utku Tekin, I will always remember you. I would also like to thank our talented technicians, Yücel Eke, Tayfun Yıldız, Nevzat Güngör, Dursun Erdoğan, Mutlu Karagülle, and to our secretary, the sweetest elder sister, Bukent Gökbakan, all of whom are an essential part of GÜNAM.

Special thanks to my friends Duygu Ergüden Karaatlı, Duygu Sözen and Özden Özaltın who are always there for me. Heartfelt thanks to Sinem Uysal and Derya Yazıcı who are my valuable confidants. I am very thankful to Op. Dr. Ümit Taşdemir, who is more of a psychiatrist than a surgeon to me ☺. Many thanks to Assoc. Dr. Barbaros Özdemir and Prof. Dr. Kıymet İkbâl Bakal Karadavut, who always recommend the most reasonable behavior for all situations. Special thanks to my dear friends Osman Gürlevik, Gözde Gürlevik, Görkem Çıkmaz, Neşe Sönmez who have joined my life a little late but have been one of the greatest people in my life. I hope we will continue to explore the life together and have happy days.

I would also like to thank Turkish Scientific and Technological Research Council (TUBİTAK) for supporting this study under 1003 - Primary Subjects R&D Funding Program Grant project number 113M941.

Last but not the least, main source of my life energy: my family. We have cherished every great moment together and they have been supporting me whenever I needed. And I need to thank them in Turkish now...

Tüm aileme, özellikle de elinden geldiğince hiçbir desteği esirgemeyen annem Zeynep Baytemir ve sevgili babam Ramazan Baytemir'e bütün teşekkürlerim az kalır. Böylesine güzel bir aileye sahip olduğum için çok şanslı hissediyorum. Tüm bu süreç boyunca, aslında hayatım boyunca verdiğiniz destek için minnettarım. Sevgili teyzelerim, canım dedem Mustafa Güzel, ve başta Kadir, Emel ve Ozan Yavuz Baytemir olmak üzere, yeryüzündeki en büyük kuzen popülasyonuna sahip olduğum için isimlerini tek tek yazamadığım canım kuzenlerim ☺, tüm desteğiniz için hepinize sonsuz teşekkürler.

## TABLE OF CONTENTS

|   |      |
|---|------|
| ABSTRACT .....  | v    |
| ÖZ .....  | vii  |
| ACKNOWLEDGMENTS .....   | x    |
| TABLE OF CONTENTS .....   | xiii |
| LIST OF TABLES .....  | xvi  |
| LIST OF FIGURES .....   | xvii |
| CHAPTERS  |      |
| 1. INTRODUCTION .....   | 1    |
| 1.1. Energy Crisis, Climate Change and the Demand of Renewable Energy ..... | 3    |
| 1.2. Photovoltaic Solar Energy .....  | 5    |
| 1.3. The Solar Cell Device .....  | 7    |
| 1.3.1. The Operating Principle of the Solar Cells .....                     | 9    |
| 1.3.2. Current-Voltage Characteristics .....                                | 11   |
| 1.3.3. The Shockley-Queisser Limit .....                                    | 14   |
| 1.4. Crystalline Silicon Solar Cells .....                                  | 18   |
| 1.4.1. Fabrication of c-Si Solar Cells .....                                | 18   |
| 1.4.2. Low Cost Routes in c-Si Solar Cell Technology .....                  | 27   |
| 2. RADIAL JUNCTION FOR SOLAR CELLS .....                                    | 33   |
| 2.1. Introduction .....   | 33   |
| 2.2. Literature Review .....  | 34   |
| 2.2.1. Enhanced Carrier Collection .....                                    | 34   |
| 2.2.2. Improved Light Absorption .....                                      | 36   |

|   |    |
|---|----|
| 2.2.3. Fabrication of Radial Geometry .....   | 40 |
| 2.3. Challenges in Radial Junction Solar Cell Technology .....  | 45 |
| 3. METAL ASSISTED ETCHING THROUGH PHOTOLITHOGRAPHY:<br>MICROPILLARS ON P-TYPE MONOCRYSTALLINE SILICON .....     | 49 |
| 3.1. Introduction.....  | 49 |
| 3.2. Metal Assisted Etching .....   | 50 |
| 3.2.1. Catalyst Types and Their Reaction Mechanisms .....   | 51 |
| 3.2.1.1. Liquid Phase Catalyst .....  | 51 |
| 3.2.1.2. Solid Phase Catalyst .....   | 53 |
| 3.2.2. Mass Transport .....   | 55 |
| 3.3. Application of MAE Through Photolithography .....  | 56 |
| 3.3.1. Sample Preparation.....  | 56 |
| 3.3.2. Photolithography .....   | 57 |
| 3.3.3. Thermal Evaporation .....  | 61 |
| 3.3.4. Metal Lift-off.....  | 61 |
| 3.3.5. Metal Assisted Etching of Si .....   | 62 |
| 4. SILICON MICROPILLARS FOR SOLAR CELL APPLICATIONS: RADIAL<br>JUNCTION ON P-TYPE MONOCRYSTALLINE SILICON ..... | 65 |
| 4.1. Introduction.....  | 65 |
| 4.2. Experimental Procedures .....  | 66 |
| 4.3. Results and Discussion .....   | 69 |
| 4.3.1. Photolithography and Metal Assisted Etching .....  | 69 |
| 4.3.2. Reflectance .....  | 71 |
| 4.3.3. Optimization of Co-firing Process for Metallization.....   | 74 |

|  |     |
|--|-----|
| 4.3.4. Solar Cell Results.....   | 77  |
| 4.4. Conclusion.....   | 81  |
| 5. GOLD IMPURITIES IN CRYSTALLINE SILICON: RADIAL JUNCTION SOLAR CELLS ON LOW QUALITY CRYSTALLINE SILICON WAFERS ..... | 83  |
| 5.1. Introduction .....  | 83  |
| 5.2. Metal Impurities in Crystalline Silicon .....   | 84  |
| 5.2.1. Solubilities and Diffusivities of Metal Impurities .....  | 85  |
| 5.2.2. Diffusion Mechanisms .....  | 85  |
| 5.3. Experimental Procedures: Radial Junction Solar Cells on Low Quality Silicon Wafers .....                          | 86  |
| 5.4. Results and Discussion.....   | 89  |
| 5.5. Conclusion.....   | 95  |
| 6. RADIAL JUNCTION SOLAR CELLS ON THIN CRYSTALLINE SILICON WAFERS .....  | 97  |
| 6.1. Introduction .....  | 97  |
| 6.1.1. Towards Radial Junction, Thin c-Si Solar Cells.....   | 97  |
| 6.1.2. Si Wafer Thinning.....  | 99  |
| 6.2. Experimental Procedures.....  | 100 |
| 6.3. Results and Discussion.....   | 102 |
| 6.4. Conclusion.....   | 116 |
| 7. CONCLUSIONS .....   | 119 |
| REFERENCES.....  | 123 |
| CURRICULUM VITAE.....  | 145 |

## LIST OF TABLES

|   |     |
|---|-----|
| Table 1.1. Record single-junction terrestrial cell efficiencies measured under the global AM 1.5 spectrum (1000 W/m <sup>2</sup> ) at 25°C. ....  | 17  |
| Table 2.1. A summary of different types of radial junction solar cell results. ....   | 46  |
| Table 4.1. The performance parameters of the 500 μm thick planar solar cells with respect to different firing belt speeds at 900 C peak temperature. ....   | 76  |
| Table 4.2. Performance Values of Radial Junction Solar Cells with different micropillar length.....   | 77  |
| Table 5.1. Performance parameters of Au contaminated and uncontaminated planar and radial junction solar cells as a function of firing belt speed. ....   | 92  |
| Table 5.2. The average of the performance parameters of Au contaminated and uncontaminated planar and radial junction solar cells.....  | 93  |
| Table 6.1. Performance parameters of the radial junction solar cells with different micropillars length. The averages of the performance values of the planar solar cell are given as a comparison..... | 109 |
| Table 6.2. J-V curves of planar and radial junction solar cells with various thicknesses. ....  | 115 |



## LIST OF FIGURES

|   |    |
|---|----|
| Figure 1.1. Decrease in some fossil fuel reserves over the years [3].   | 3  |
| Figure 1.2. Annual greenhouse gas emissions by different gases [5].   | 4  |
| Figure 1.3. Comparison of finite and renewable energy reserves [6].   | 5  |
| Figure 1.4. Band gap energy of metal, semiconductor and insulator materials.  | 7  |
| Figure 1.5. First solar cell sketch from Russel Ohl's patent [16].  | 8  |
| Figure 1.6. An image from the original publication of 6% efficient first silicon solar cell fabricated at Bell Telephone Laboratories [18].                         | 9  |
| Figure 1.7. (a) Solar cell structure, (b) the band diagram.   | 10 |
| Figure 1.8. Equivalent circuit diagram of solar cell in a) ideal case, b) realistic case.   | 12 |
| Figure 1.9. Current–voltage characteristics of a typical solar cell in dark and illuminated condition.  | 13 |
| Figure 1.10. Fundamental loss components for solar cells and the efficiency limits of the solar cells as a function of band gap energies [22, 23].                  | 15 |
| Figure 1.11. The highest confirmed single-junction terrestrial cell efficiencies measured under the global AM1.5 spectrum (1000 W/m <sup>2</sup> ) at 25°C [24-66]. | 16 |
| Figure 1.12. Fabrication process of conventional crystalline Si solar cells.  | 19 |
| Figure 1.13. Absorption coefficient and depth of intrinsic Si at 300 °K as a function of wavelength [74].   | 20 |
| Figure 1.14. Schematic of reflection of light from a) flat and b) textured Si wafer surfaces.   | 21 |
| Figure 1.15. Schematic cross-sectional view of a tubular diffusion furnace for solid state diffusion.   | 22 |
| Figure 1.16. Reflectance spectra of flat and textured Si with and without ARC.  | 24 |
| Figure 1.17. (a) Schematic of resistive components and current flow directions, b) Top contact schemes.   | 26 |

Figure 1.18. Schematic of a solar cell, before and after edge isolation by laser grooving..... 27

Figure 1.19. Conventional, planar solar cell design. The cell thickness  $L$  should be greater than the optical thickness  $1/\alpha$  and minority electron diffusion length  $L_n$  should be long enough that minority carriers could reach the junction region before recombination. .... 29

Figure 1.20. Vertical Multijunction (VMJ) solar cell design. The cell thickness  $L$  should be greater than the optical thickness  $1/\alpha$ , but with this design, the low minority carrier diffusion lengths  $L_n$  can be obtained so that any minority carrier is within the diffusion length..... 30

Figure 1.21. Parallel Multijunction (PMJ) solar cell design. It is necessary that the cell thickness  $L$  should be greater than the optical thickness  $1/\alpha$ , but with this design, the low minority carrier diffusion lengths  $L_n$  can simply be obtained so that any minority carrier is within the diffusion length. Although this minority carrier diffusion and light harvesting direction are parallel, this design has the basic properties of VMJ design. .... 31

Figure 1.22. Radial p-n junction solar cell design. It is necessary that the cell thickness  $L$  should be greater than the optical thickness  $1/\alpha$ , but as in the PMJ and VMJ designs, the low minority carrier diffusion lengths  $L_n$  can be obtained so that any minority carrier is within the diffusion length..... 32

Figure 2.1. Schematic of a) planar and b) radial junction geometries. .... 35

Figure 2.2. Efficiency as a function of cell thickness  $L$  and minority-electron diffusion length  $L_n$  for a) planar p-n junction silicon cell and b) radial p-n junction silicon [89]. .... 36

Figure 2.3. a) Schematic of the periodic silicon wire array structure. b) Absorptance of the wires with  $L=1.16, 2.33, \text{ and } 4.66 \mu\text{m}$  ( $d=50 \text{ nm}$ ). The absorptance of a thin film is included as a reference [103]..... 37

Figure 2.4. (a) Absorptance, (b) reflectance, and (c) transmittance spectra of  $20 \mu\text{m}$  long Si wires with radii of  $50 \text{ nm}, 200 \text{ nm}$  and  $3 \mu\text{m}$ . The parameters of  $6$  and  $20 \mu\text{m}$  thick Si films are shown for comparison. The filling fraction is fixed at  $0.3$  [104].. 38

|  |    |
|--|----|
| Figure 2.5. (a) Experimental C–V measurement on the wire array structure and reference cells. Wire array solar cells represent two kind of junction: Radial and Planar. (b) Geometry of radial p–n junction structure [100].   | 39 |
| Figure 2.6. Radial p–n junction fabrication process. (a) VLS-grown with Cu catalyst, p-Si microwire array structure. (b) Catalyst removal, thermal oxide growth and PDMS layer deposition. (c) Removal of the thermal oxide. (d) Removal of the PDMS and phosphorus diffusion [116].   | 41 |
| Figure 2.7. Wire array fabrication process (top). SEM images of (a) single layer of silica beads on a silicon wafer, (b) completed ordered silicon nanowire radial p-n junction and edge of finger contact (inset), (c) cross-sectional SEM of the solar cell. (d) Optical image silicon wire radial junction solar cell [109].                | 43 |
| Figure 2.8. Schematic illustration of (CNMW) of MWs and tapered NWs: (1) Deposition of Ag nanoparticles by galvanic displacement following the formation of antidot photoresists. (2) Wire structure formation by MAE. (3) Formation of the CNMW structure by KOH etching (4) Further KOH tapering to obtain only nanowire residues [99].      | 44 |
| Figure 3.1. Schematic illustration of electroless Ag deposition and etching process on Si wafer immersed in HF/AgNO <sub>3</sub> solution.   | 52 |
| Figure 3.2. Schematic illustration of metal assisted etching of silicon via solid phase catalyst; pillars, holes, sheets a) pre-etching b) after etching.  | 54 |
| Figure 3.3. Schematics of proposed mass transport mechanisms for MAE. (a) the reagent and byproduct diffuse along the noble metal and Si substrate interface. Si atoms are oxidized in this interface. (b) Si atoms are dissolved and diffuse through noble metal to the metal and solution interface and are then oxidized in this interface. | 55 |
| Figure 3.4. Schematic illustration of micropillar array structure fabrication steps.   | 56 |
| Figure 3.5. Comparison of a) undercut sidewall profile that causes discontinuities in coating and easier lift-off and b) overcut sidewall profile.   | 58 |
| Figure 3.6. Schematic illustration of obtaining undercut sidewall profile by image reversal process  | 59 |

|  |    |
|--|----|
| Figure 3.7. AZ 5214 E PR thickness as a function of spin speed.....  | 60 |
| Figure 3.8. Scanning electron microscope image of PR patterns with undercut sidewall profile on Si substrate .....   | 60 |
| Figure 3.9. Optical microscope images of (a) PR patterns before lift-off, (b) Au layer with the circular holes after lift-off process.....   | 62 |
| Figure 3.10. Scanning electron microscope images of micropillars on the surface of silicon wafers at two different magnifications.....   | 63 |
| Figure 4.1. Process sequence for radial junction solar cell production. ....   | 67 |
| Figure 4.2. Phosphorus diffusion profile measured by SIMS method at EAG Laboratuaries. The inset shows schematics of radial geometry after doping. ....  | 68 |
| Figure 4.3. Image of the well-ordered photoresist dots on the sample after photolithography.....   | 69 |
| Figure 4.4. Micropillar length with respect to duration of MAE by [HF] = 1.8 M, [H2O2] = 0.4 M, H2O solution. ....   | 70 |
| Figure 4.5. Low-magnification and higher-magnification (insets) cross-sectional SEM images of silicon micropillar arrays at length of (a) 1.7 $\mu\text{m}$ (10 min. etching), (b) 2.3 $\mu\text{m}$ (20 min. etching), (c) 3.2 $\mu\text{m}$ (30 min. etching), (d) 5.0 $\mu\text{m}$ (40 min. etching), (e) 6.1 $\mu\text{m}$ (50 min. etching), (f)13.9 $\mu\text{m}$ (90 min. etching). .... | 71 |
| Figure 4.6. Reflectance spectrum for samples having different length of micropillars a) before ARC and b) after ARC. Reflection results of planar and pyramid textured samples were inserted for comparison.....   | 72 |
| Figure 4.7. Average reflectance for each micropillar length before and after ARC. The length zero is for planar samples. Reflection results of pyramid textured samples were inserted as reference lines.....  | 73 |
| Figure 4.8. A typical co-firing temperature profile for $\sim 180 \mu\text{m}$ thick solar cells ....  | 75 |
| Figure 4.9. The performance parameters with respect to different firing profiles for 500 $\mu\text{m}$ thick planar solar cells.....   | 76 |
| Figure 4.10. J-V curves of radial junction solar cells for different micropillar length. ....  | 77 |
| Figure 4.11. Jsc, Voc and Efficiency curves as a function of micropillar length .....  | 78 |

|   |     |
|---|-----|
| Figure 4.12. IQE spectrum for the Radial Junction Solar Cells with different micropillar length.....  | 79  |
| Figure 4.13. (a) Semilog, (b) Linear dark J-V characteristics of solar cells with planar and radial junction having 6,1 $\mu\text{m}$ micropillar length.....   | 80  |
| Figure 5.1. Process sequence for planar and radial junction solar cell productions on Au contaminated and uncontaminated Si wafers.....   | 88  |
| Figure 5.2. Photoluminescence lifetime mapping and after 20 nm $\text{Al}_2\text{O}_3$ deposition and activation. (a) reference sample, (b) 10 nm Au coated and diffused at 800C for 1 h (c) 10 nm Au coated, diffused at 800C for 1 h and 10 $\mu\text{m}$ etched from both sides..... | 90  |
| Figure 5.3. Performance parameters of Au contaminated and uncontaminated planar and radial junction solar cells as a function of firing belt speed.....   | 91  |
| Figure 5.4. Circuit current density vs. voltage graph obtained from the averages of the parameters of Au contaminated and uncontaminated planar and radial junction solar cells.....  | 94  |
| Figure 5.5. Averages of Internal Quantum Efficiencies of Au contaminated and uncontaminated Planar and Radial Junction Solar Cells as a function of wavelength.....   | 95  |
| Figure 6.1. Schematic of radial junction solar cell with thin, flexible substrate.....  | 98  |
| Figure 6.2. (a) Isotropic, (b) Partially Anisotropic, (c) Completely Anisotropic etchings.....  | 99  |
| Figure 6.3. Process sequence for planar and radial junction solar cell productions at various thicknesses.....  | 101 |
| Figure 6.4. The cross-sectional SEM images of the etched samples with $[\text{HF}] = 1.8, \text{M}$ $[\text{H}_2\text{O}_2] = 0.4 \text{ M}$ , (a) $\text{H}_2\text{O}$ (b) Ethanol; the etching duration was 60 min.....   | 103 |
| Figure 6.5. Low-magnification and higher-magnification (insets) SEM images of the etched samples with $\text{H}_2\text{O}-[\text{H}_2\text{O}_2] = 0.4 \text{ M}$ and (a) $[\text{HF}] = 1.8 \text{ M}$ , and (b) $[\text{HF}] = 5.4 \text{ M}$ ; the etch duration was 60 min.....     | 104 |
| Figure 6.6. Low-magnification and higher-magnification (insets) SEM images of the samples after the application of 1% KOH etching at 75-80 $^\circ\text{C}$ for, (a) 0, (b) 1, (c) 5,   |     |

|   |     |
|---|-----|
| (d) 10, (e) 20, (f) 30 seconds following MAE with [HF] = 5.4 M [H <sub>2</sub> O <sub>2</sub> ] = 0.4 M, Ethanol solution; the etching duration was 300 min. ....   | 105 |
| Figure 6.7. The cross-sectional SEM images of the samples etched for (a) 60, (b) 180, (c) 300, (d) 720, (e) 1200 minutes with [HF] = 5.4 M [H <sub>2</sub> O <sub>2</sub> ] = 0.4 M, Ethanol solution. .... | 106 |
| Figure 6.8. Micropillar length with respect to duration of MAE by [HF] = 5.4 M, [H <sub>2</sub> O <sub>2</sub> ] = 0.4 M, Ethanol solution.....   | 106 |
| Figure 6.9. Weighted reflectance for each micropillar length after ARC. The length zero is for planar samples. Reflectance results of pyramid textured sample was inserted as reference line. ....          | 107 |
| Figure 6.10. Current Density vs Voltage curves of the radial junction solar cells with different micropillars length. The J-V curve of planar junction solar cell is also given as comparison. ....         | 108 |
| Figure 6.11. External Quantum Efficiency Spectra of Radial Junction Solar Cell with various micropillars length. ....   | 110 |
| Figure 6.12. Internal Quantum Efficiency and Reflectance Spectra of Radial Junction Solar Cell with various micropillars length. ....   | 111 |
| Figure 6.13. The cross-sectional SEM images of a) 1 h b) 2 h c) 3h etched radial junction solar cells, d) Ag finger on micropillars, e) SEM image, f) picture of thinnest planar solar cell.....            | 112 |
| Figure 6.14. EQE spectra of unetched and etched a) planar and b) radial junction solar cells with metallization problem.....  | 113 |
| Figure 6.15. J-V curves of planar and radial junction solar cells with various thicknesses. ....  | 114 |
| Figure 6.16. The change in a) J <sub>sc</sub> and b) V <sub>oc</sub> values of planar and radial junction solar cells with respect to cell thicknesses. ....  | 115 |
| Figure 6.17. IQE and reflectance spectra of a) planar and b) radial junction solar cells as a function of wavelength with respect to cell thicknesses.....  | 116 |

## CHAPTER 1

### INTRODUCTION

*“We are like tenant farmers chopping down the fence around our house for fuel when we should be using Nature’s inexhaustible sources of energy — sun, wind and tide...”*

*I'd put my money on the sun and solar energy. What a source of power!*

*I hope we don't have to wait until oil and coal run out before we tackle that.”*

Thomas Alva Edison,

in conversation with Henry Ford and Harvey Firestone (1931).

Many years ago, Thomas A. Edison, the inventor of the light bulb, recognized the capacity of the sun as an almost unlimited source of energy. Although the depletion of fossil fuel reserves has been getting closer, the full potential of solar power is yet to be controlled by humanity. Solar energy could be harvested using different methods. Photovoltaic energy conversion remains the most appealing approach since it converts the readily available energy source, solar energy, directly into electrical energy [1, 2]. Hence, solar photovoltaic (PV) devices could be more practical and applicable than other renewable energy sources, i.e. wind power, fuel cells, geothermal energy, and biofuels. On the other hand, larger device areas are necessary for efficient collection of solar energy in comparison with fossil fuels which can be burned in small stations. However, PV applications can be small, local and distributed that can ultimately eliminate the need for the construction of large grids.

When considering different energy resources, we see that the cost of energy generation is perhaps the important factor determining their wide spread usage. Despite their catastrophic damage to the environment, almost 85% of energy demand are still supplied from fossil fuels. On the other hand, although we know that solar energy is clean, infinite, available almost everywhere, its use has been limited mainly due to the high cost of energy generation from solar radiation. However, in the last two decades, tremendous decrease in the manufacturing cost and improvement in the efficiency of the devices have made solar electricity generated by PV systems very competitive with the other resources. The so-called Levelized Cost of Electricity (LCOE) from PV has reached the level of 4-5 c\$/kWh in Turkey which is lower than almost all other energy resources including coal, nuclear power and natural gas. So, the solar energy is on its way to become the cheapest energy source. In this journey, there are still some economical, physiological and technical problems that need to be overcome. Therefore, for an ultimate victory, more effort in the development of technically feasible and low-cost photovoltaic devices is required.

This thesis focuses on a non-conventional device architecture providing a high efficiency and hopefully a low-cost alternative to present devices. This new solar cell design consists of radial p-n junction micropillar arrays and allows separate optimization for the design requirements of light absorption and carrier collection, the conditions required for efficient energy conversion in a photovoltaic device.

This thesis is composed of 7 chapters. In this first chapter, the motivation in photovoltaics and the suggested solar cell design concept are mentioned and discussed. In Chapter 2, literature review about the studies on enhanced carrier collection, improved light absorption and fabrication of radial junction solar cells is given. In the 3<sup>rd</sup> chapter, metal assisted etching method used to fabricate radial geometry in this thesis is detailed and the process steps are explained. In chapter 4, fabrication and the results of radial junction solar cells with different geometry are mentioned. Chapter 5 and 6 demonstrate the comparison of the conventional and radial junction solar cells on high- and low-quality materials, and on thin Si substrate,



respectively. In the 7<sup>th</sup> chapter, the last chapter, the studies of this thesis are concluded with a summary of the previous chapters.

### 1.1. Energy Crisis, Climate Change and the Demand of Renewable Energy

In recent years, the science community and the popular news media have had many discussions about the energy crisis and climate change. These debates originate from the fact that the use of fossil fuels preferred due to their low cost has been increased along with population growth and they have started to run out.

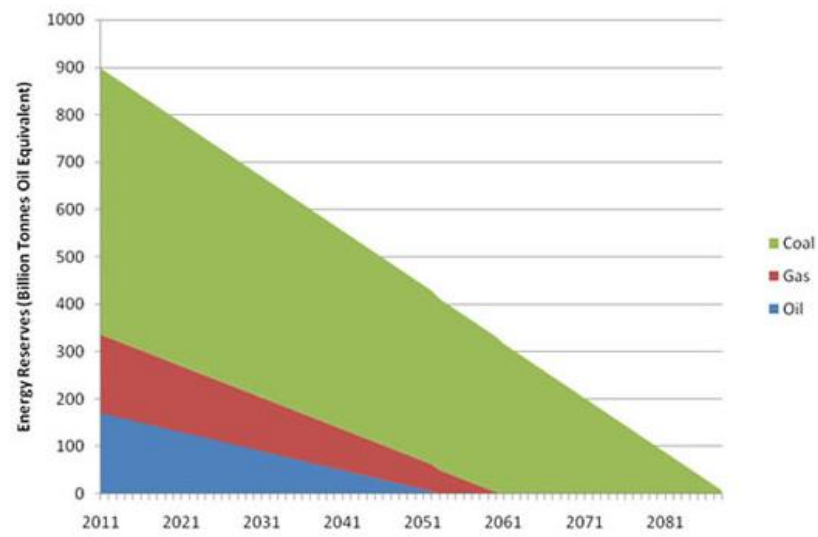


Figure 1.1. Decrease in some fossil fuel reserves over the years [3].

According to Central Intelligence Agency (USA) reports, the annual consumption of oil in fossil fuels is more than 4 billion tons. Even if the increase in population is ignored altogether, the total oil will completely run out in 2052. The natural gas is another fossil fuel with higher reserves, but the dependence of gas is likely to increase due to the decrease in oil reserves. As a result, the gas is expected to run out by the year 2060. Even though the coal is expected to last longer, by the year 2088 it will

also be depleted (Figure 1.1). When new fuel reserves are discovered, this process can be extended slightly [3, 4]. As fossil fuels begin to run out, the dependence of the world on remaining fossil fuels will be accelerated. For this reason, new energy sources are required and this issue, which concerns the whole world, is a matter of political and scientific debate.

Furthermore, the socioeconomic dimensions of the current climate change are menacing. Greenhouse gas emissions have risen to extremely high levels, despite increased policies for climate change mitigation.

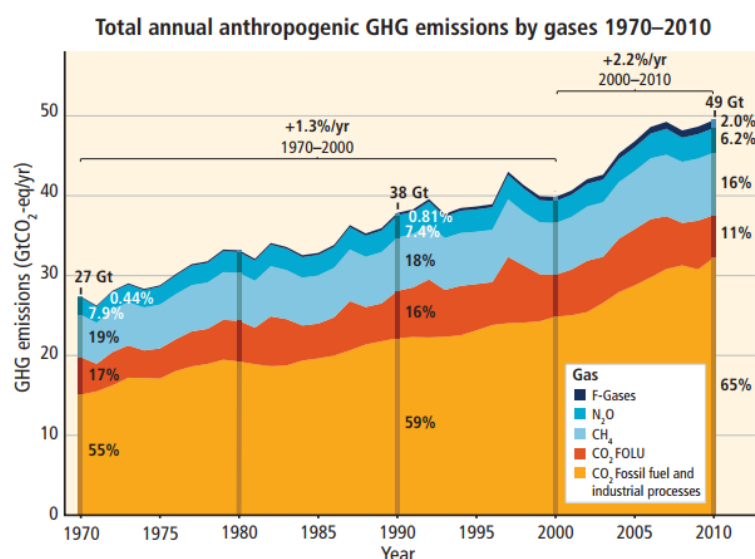


Figure 1.2. Annual greenhouse gas emissions by different gases [5].

According to the Fifth Assessment Report of the Intergovernmental Panel on Climate Change (IPCC) 2014: Synthesis Report, CO<sub>2</sub> emissions from fossil fuels and industrial processes accounted for 78% of total greenhouse gas emissions growth between 1970 and 2010, and a similar percentage (high confidence rate) curve was introduced between 2000 and 2010 (Figure 1.2). CO<sub>2</sub> emissions per year have reached 32 GtCO<sub>2</sub> for fossil fuels and grown further by 3% between 2010 and 2011 and 1 to 2 % between

2011 and 2012. In 2010, CO<sub>2</sub> remained to be the largest greenhouse gas emission, with a value of 76% of total human greenhouse gas emissions in 2010 [5].

When all these underlying reasons of scientific and political debates are combined, renewable and carbon-free energy sources have gained attention. The use of renewable and carbon-free energy resources is becoming more and more necessary to stabilize the CO<sub>2</sub> levels in the disturbed atmosphere. Figure 1.3 shows a comparison of the amount of energy sources available from different energy sources [6]. No renewable energy source other than solar energy has the capacity to create such an enormous energy. For this reason, photovoltaic technologies have been gaining more and more recognition by public and politicians as well as financial and industrial sectors.

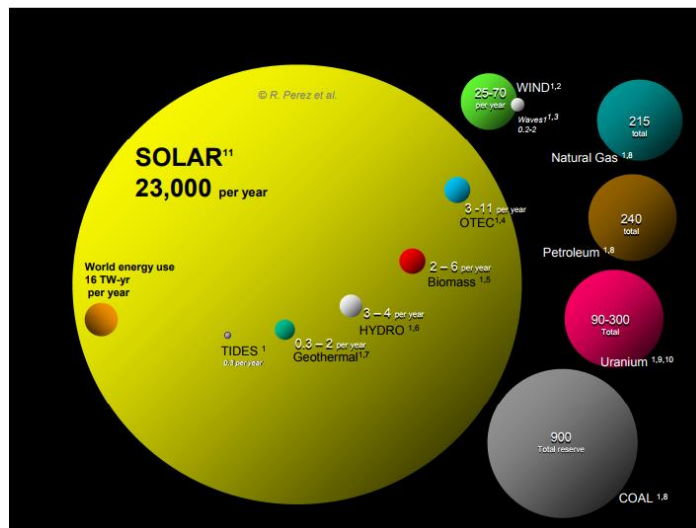


Figure 1.3. Comparison of finite and renewable energy reserves [6].

## 1.2. Photovoltaic Solar Energy

The photovoltaic solar energy (PV) is one of the thriving industries all over the world due to the fact that it directly converts solar energy into electricity with the benefit of being carbon-free. Solar thermal and photoelectrochemical cells are the alternative

devices for the solar energy conversion. While solar thermal devices use solar radiation in order to heat a liquid that is later used to drive a turbine to generate electricity, photoelectrochemical cells use a photoactive electrode to start the chemical reaction to produce electricity. Among solar energy devices, PV is considered to be the first choice as it offers low cost and flexible options in the sense that it can be used in small scales as well as large scales. In addition, it is modular; and exhibits long term stability and relatively high efficiency. In order to accelerate the usage of PV systems, studies focusing on materials, devices, and systems are intensively continuing around the world. The aim of the most of these studies is to reduce the cost of manufacturing and increase the efficiency by discovering alternative device designs with superior performances [7, 8].

The working principle of PV systems, conversion of solar radiation into electricity, is based on the photoelectric effect which was first observed by French physicist, Edmund Becquerel, in 1839 [7-13]. In photoelectric effect, the photons are absorbed by electrons present in the valence band of the material. If the absorbed photons have enough energy to excite these electrons to the conduction band, the basis of the electric current in the circuit is formed. These electrons should be transported to the contacts and collected by the external circuit.

Materials can be classified as metals, semiconductors and insulators. Presence of a forbidden energy gap and its value play an important role in determining the electrical and optical properties of materials. As it shown in Figure 1.4, in metals, the valence and the conduction bands are overlapped. Therefore, all electrons can participate in the conduction process making the material very conductive. In the case of an insulator, the band gap energy between the valence and conduction electrons is very large, which means that a large amount of energy is required to excite the electrons to the conduction band. The lack of electrons in the conduction band makes the conduction very difficult and sometimes impossible. Moreover, photons with high wavelength may not be energetic enough to excite electrons to the conduction band. In semiconductors, there exists a small enough gap between the valence and

conduction bands that allows control of conduction via thermal or optical excitement of the electrons.

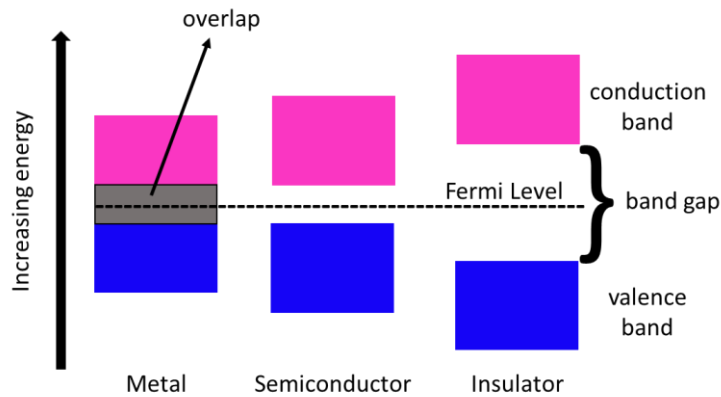


Figure 1.4. Band gap energy of metal, semiconductor and insulator materials.

If the energy of the photons is higher than the band gap energy, the electrons can easily be excited. For this reason, in general, semiconductor materials which are able to absorb a large part of the solar spectrum are used for fabrication of solar cells [10].

### 1.3. The Solar Cell Device

After the discovery of photoelectric effect by Becquerel in 1839 [9], in 1876, it was reported in a solid for the first time: under illumination, the conductivity of selenium changes. Later William Grylls Adams (who succeeded by Maxwell as professor) and his student showed that under illumination, electrical power can be generated [14].

Soon after, the first solar cell panel was fabricated by the New Yorker inventor Charles Fritts in 1883. Between 1-2% conversion efficiency was obtained by coating selenium with a thin layer of gold [15].

June 25, 1946.

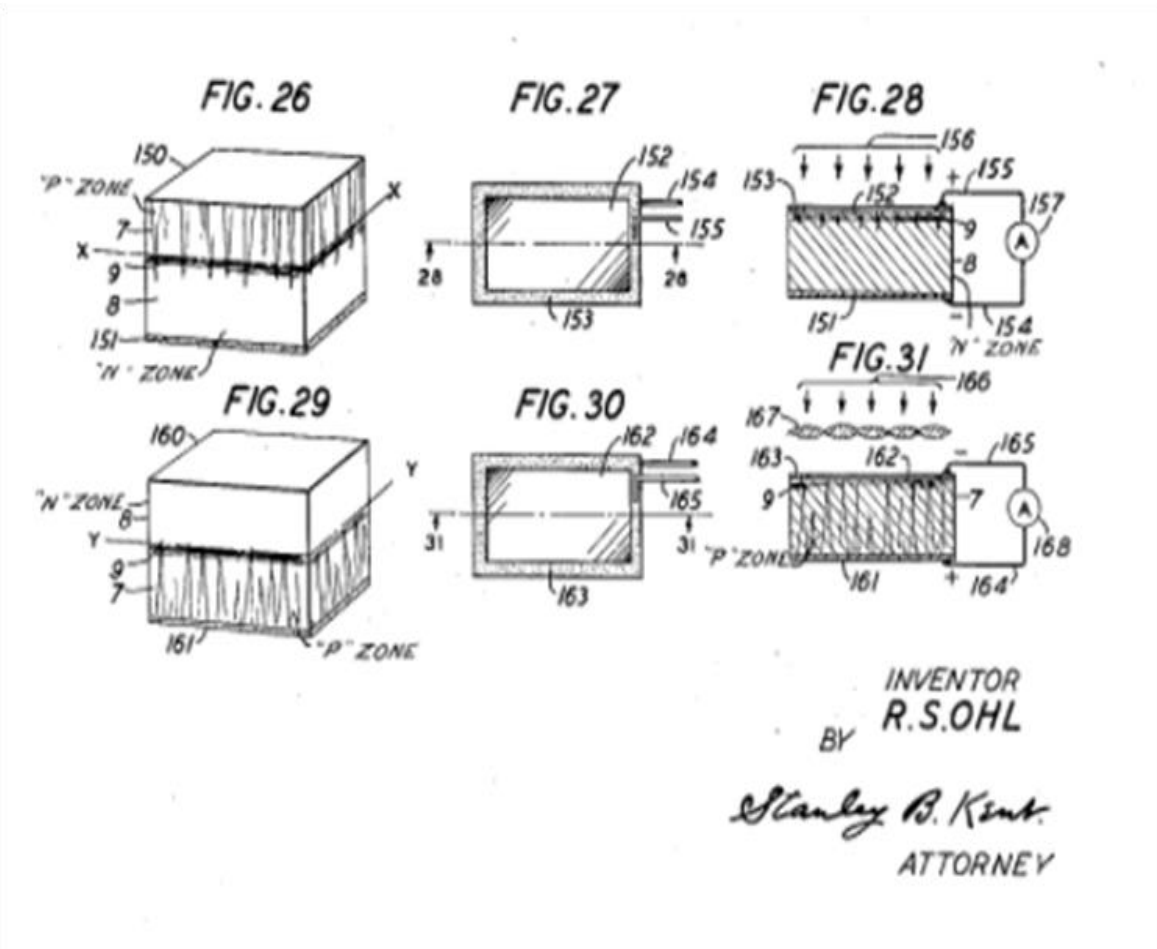
R. S. OHL

2,402,662

LIGHT-SENSITIVE ELECTRIC DEVICE

Filed May 27, 1941

5 Sheets-Sheet 3



INVENTOR  
R.S.OHL

BY  
*Stanley B. Kent*  
ATTORNEY

Figure 1.5. First solar cell sketch from Russel Ohl's patent [16].

The pioneers of photovoltaic effect were not able to understand PV effect well enough to develop solar cells further. However, the discovery of photoelectric effect and quantum physics in 1905 by Albert Einstein led to the understanding of the basic scientific principles of PV and thus improving it. In 1941, the first solar cell made of

silicon was patented by Russel Ohl [16, 17]. The sketch of the first p-n junction solar cell is shown in Figure 1.5.

However, it took years to improve solar cells beyond 1-2% efficiency. The first silicon p-n junction solar cell with an efficiency of 6% was fabricated in 1954 at Bell Laboratories (Figure 1.6).

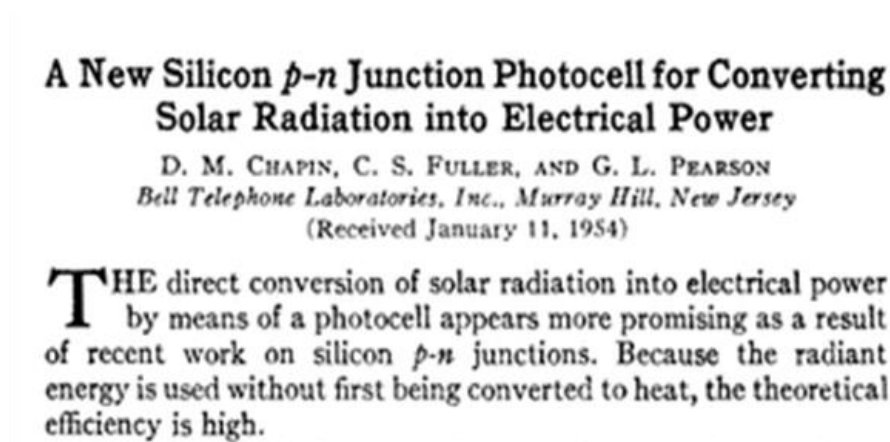


Figure 1.6. An image from the original publication of 6% efficient first silicon solar cell fabricated at Bell Telephone Laboratories [18].

The performance of PV devices has been improved through the years with the development of the necessary production techniques as well as a better understanding of the quantum processes. Today, PV technology has become a big industry with total installed capacity of 400 GW. The capacity of PV is expected to increase even further towards being one of the primary energy resources of human kind.

### 1.3.1. The Operating Principle of the Solar Cells

The working principles of a solar cell are based on carrier generation and collection mechanisms. This is usually implemented by a p-n junction in a semiconductor, which

provides an electric field to separate electron and hole pairs. A simple solar cell structure and the band diagram is shown in Figure 1.7 (a) and (b).

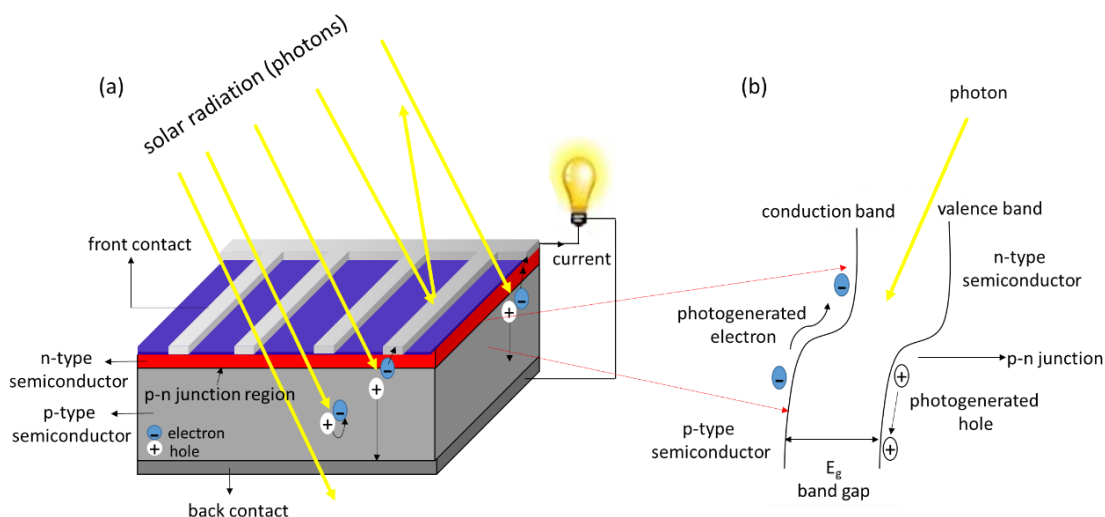


Figure 1.7. (a) Solar cell structure, (b) the band diagram.

When a p-n junction is formed, free electrons of n-type semiconductors and holes from the p-type region near the contact undergo a recombination process leaving behind positively and negatively charged dopant atoms on the n-side and p-side, respectively. This region which resembles an electric dipole system (i.e., a parallel plate capacitor) and depleted from free carriers is called the depletion region. An electric field is then developed across the region. A p-n junction without any external input is in equilibrium between carrier generation, recombination, diffusion and drift in the presence of electric field in the depletion region. Due to the electric field which creates an obstacle to the diffusion of the carriers, the majority carriers which enter the depletion region move back towards the region they originate. However, some majority carriers with high velocities may cross the junction region by diffusion despite the presence of the electric field. Carriers that cross the junction represent minority carriers. In equilibrium, these minority carriers may travel a distance equal



to the diffusion length before they recombine. In equilibrium, the current caused by the diffusion of the carriers, diffusion current, is equal to the current which enables the minority carriers reaching the edge of the diffusion region to be swept across due to the electric field in the junction region, drift current. Therefore, in equilibrium, the electron drift current and electron diffusion current, the hole drift current and the hole diffusion current balance out and there is no net current passing through the device. However, when a voltage is applied across the solar cell device, such that the electric field generated by the p-n junction decreases, it enables the diffusion of the carriers and leads to an increase in the diffusion current, i.e. forward bias. When a voltage is applied to increase the electric field, diffusion current decreases, i.e. reverse bias. With the applied voltage, while the change in the diffusion current is observed, the drift current remains almost unchanged. In fact, the width of the depletion region varies with the applied voltage. In the forward bias condition, there will be a small increase in drift current as the depletion region width increases. On the other hand, there is a small decrease in drift current for reverse bias condition due to the decrease of the width of the depletion region. However, in silicon solar cells, the change in drift current is a second order effect.

Here, it should be noted that only photons with higher or equal energy to the semiconductor bandgap energy are absorbed and create e-h pair generation and photogenerated current.

### 1.3.2. Current-Voltage Characteristics

When the solar cell is connected to the load that biases the junction in forward direction, photogenerated current ( $J_L$ ) causes voltage drop across the load. The biased p-n junction results in bias diode current ( $J_D$ ) in opposite direction to the  $J_L$ . Therefore, the total current under the illumination condition is,

$$J = J_D - J_L = J_0 \left[ \exp\left(\frac{qV}{kT}\right) - 1 \right] - J_L \quad (1.1)$$

where  $J_0$  is reverse saturation current,  $k$  is the Boltzmann constant,  $q$  is charge of the electron and  $T$  is the temperature. However, this equation is for the ideal case whose equivalent circuit diagram is shown in Figure 1.8-a. In the real case, shunt resistance,  $R_{sh}$  which accounts for various leakage currents due to different recombination effects and series resistance,  $R_s$  which accounts for ohmic losses in the bulk material, metal contacts during the current collection and the metal-semiconductor interface affect the performance of the cell. Then the modified version of the current equation under illumination is,

$$J = J_D - J_L = J_0 \left[ \exp\left(\frac{q(V - J R_s)}{n k T}\right) - 1 \right] + \left(\frac{V - J R_s}{R_{sh}}\right) - J_L \quad (1.2)$$

Where  $n$  is the ideality factor which accounts for the nonideal p-n junction diode. The equivalent circuit diagram for the realistic case is shown in Figure 1.8-b.

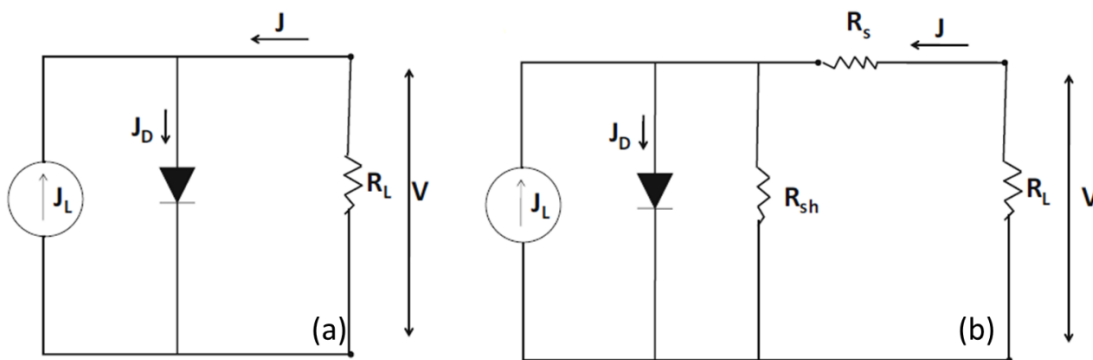


Figure 1.8. Equivalent circuit diagram of solar cell in a) ideal case, b) realistic case.

A typical J-V characteristic of a solar cell under dark and illuminated conditions is given in Figure 1.9. The photogenerated current  $J_L$  would be zero under dark condition. The J-V curve is shifted downward with the photocurrent generated.

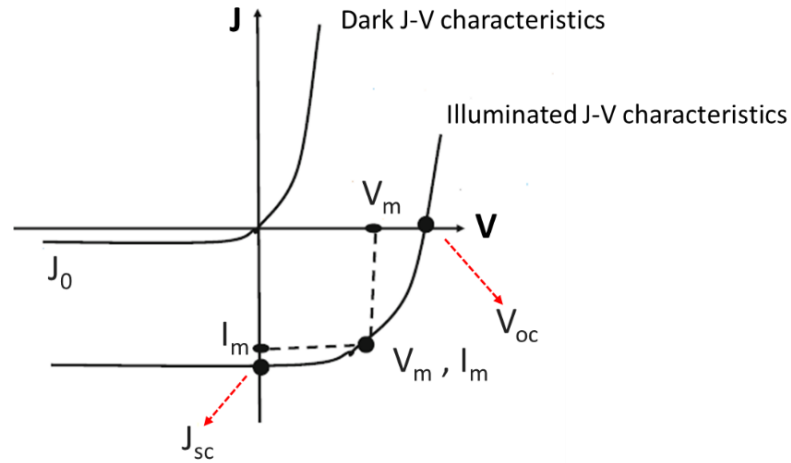


Figure 1.9. Current–voltage characteristics of a typical solar cell in dark and illuminated condition.

The overall performance of a solar cell is evaluated by using the device parameters as listed below,

- 1- The current density at zero bias, short circuit current ( $J_{sc}$ ),
- 2- The voltage at zero current, open circuit voltage ( $V_{oc}$ ), and
- 3- MPP, where the maximum power can be obtained. Two important figures of merit are calculated from these three quantities. The first one is the fill factor (FF) which is defined as [1],

$$FF = \frac{V_{MPP} J_{MPP}}{V_{OC} J_{SC}} \quad (1.3)$$

where  $V_{MPP}$  and  $J_{MPP}$  are the voltage and current at MPP, respectively. The second one is the power conversion efficiency ( $\eta$ ) defined as [1],

$$\eta = \frac{V_{MPP} J_{MPP}}{P_{in}} = \frac{J_{SC} V_{OC} FF}{P_{in}} \quad (1.4)$$

### 1.3.3. The Shockley-Queisser Limit

Since the first practical photovoltaic device fabricated at Bell Laboratories in 1954 [18], many studies have been conducted in order to increase the efficiency of solar cells. However, as emphasized in the famous article of William Shockley and Hans Queisser, [19], there exists a certain limit to the efficiency of solar cell devices. In 1960, when the maximum energy efficiency obtained from the solar cells was 9-10%, they calculated the maximum efficiency with some assumptions to be 30% for an energy band gap of 1.1 eV. They applied detailed balance limit using the feel of thermodynamics, to calculate this limit. One of their assumptions was to consider absorption as a step function. For every photon absorbed by the solar cell with energy equal or greater than band gap energy, one e-h pair is generated. The photons whose energies are below band gap energy cannot be absorbed by the solar cell. Their argument depends on the reciprocity between absorption and emission: if a material is absorptive, then due to the Kirchhoff's law of thermal radiation, this material is emissive in thermal equilibrium. The solar cell and the sun are modelled as blackbody in their argument, at 300 K and 6000 K respectively. Another assumption was that the only recombination loss comes from the radiative recombination.

The Shockley-Queisser limit places the maximum solar conversion efficiency around 33.7% for a single p-n junction device with a band gap of 1.34 eV and using an AM 1.5 G solar spectrum.

However, unlike the assumption of the Shockley-Queisser limit, not all photons with energy higher than the band gap energy, in fact, can be absorbed by the solar cells which causes low  $J_{sc}$  values. For instance, some photons may disappear due to high front reflection or poor absorption. Low absorption problems occur in solar cells which contain substrates with poor absorption properties or some thin film solar cells [1] owing to their small thickness. In order to reduce the reflection and to increase the optical path of photons circulating in the device, some advanced optical designs have been suggested [20, 21]. Radiative recombination which is the dominant loss

mechanism for solar cells close to Shockley-Queisser limit, can be effectively suppressed to increase  $V_{oc}$ . The photogenerated carriers can radiatively recombine to create a photon per electron-hole pair. These photons can be re-absorbed, however, most of them are disappeared by leaving the device or being parasitically absorbed by non-photovoltaic sides or backside mirror. With design improvements, emitted photons can be re-absorbed, and the photon recycling can be provided.

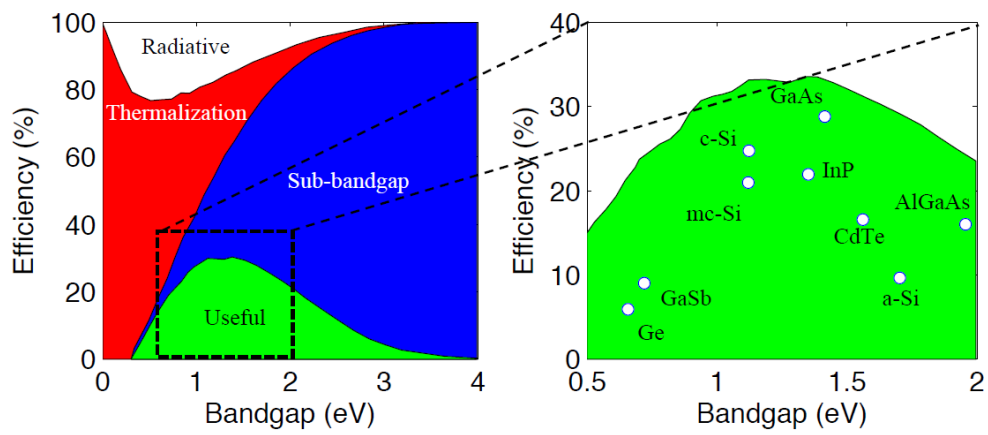


Figure 1.10. Fundamental loss components for solar cells and the efficiency limits of the solar cells as a function of band gap energies [22, 23].

Fundamental loss components and the efficiency limits of the solar cells which consist of common semiconductor materials as a function of band gap energies are shown in Figure 1.10. Thermalization loss originates from the absorption of a photon with considerably higher energy than material band gap. For solar cells fabricated from semiconductors with low band gap energies, thermalization losses are dominant. The sub-bandgap loss mechanism is dominant for the solar cells fabricated from high bandgap semiconductors. Accordingly, for ideal solar cells, the band gap is required to be between 1.1 and 1.7 eV.

In Figure 1.11, available record efficiencies and the efficiency improvements of solar cells from the most commonly used materials are shown [24-66]. Also, Table 1.1

summarizes the highest achieved efficiencies from the materials used to fabricate solar cells in the last years [66].

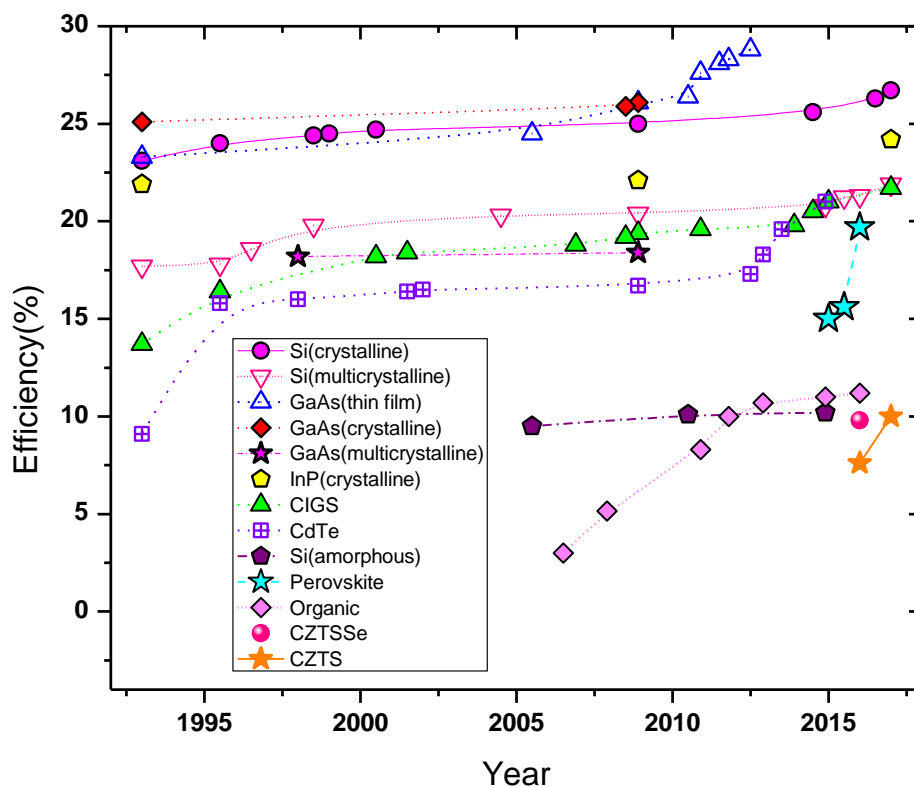


Figure 1.11. The highest confirmed single-junction terrestrial cell efficiencies measured under the global AM1.5 spectrum (1000 W/m<sup>2</sup>) at 25°C [24-66].

Among all the materials used to fabricate solar cells, GaAs and Si are the most remarkable materials since the cells containing these materials have the highest efficiency values. Nowadays, GaAs solar cell has the closest value to its own Shockley-Queisser limit with the efficiency value of 28.8%, while with 26.7% efficiency, Si solar cell is still below its ultimate limit value [66].

Moreover, although none of them have higher efficiency values than the conventional ones yet, there are lots of alternatives to the Shockley-Queisser single junction limit

reported such as, multi-exciton generation [67], intermediate band gap states [68] and hot carrier collection [69].

*Table 1.1. Record single-junction terrestrial cell efficiencies measured under the global AM 1.5 spectrum (1000 W/m<sup>2</sup>) at 25°C.*

| Substrate               | Efficiency (%) | Area (cm <sup>2</sup> ) | V <sub>oc</sub> (V) | J <sub>sc</sub> (mA/cm <sup>2</sup> ) | FF (%) | Company, Description  |
|-------------------------|----------------|-------------------------|---------------------|---------------------------------------|--------|-----------------------|
| Si (crystalline)        | 26.7 ± 0.5     | 79                      | 0.738               | 42.65                                 | 84.9   | Kaneka, n-type IBC    |
| Si (multicrystalline)   | 22.3 ± 0.4     | 4                       | 0.674               | 41.08                                 | 80.05  | FhG-ISE, n-type       |
| GaAs (thin film)        | 28.8 ± 0.9     | 0.9                     | 1.122               | 29.68                                 | 86.5   | Alta Devices          |
| GaAs (crystalline)      | 26.4 ± 0.8     | 1.006                   | 1.030               | 29.8                                  | 86.0   | Fraunhofer ISE        |
| GaAs (multicrystalline) | 18.4 ± 0.5     | 4                       | 0.994               | 23.2                                  | 79.7   | RTI, Ge substrate     |
| InP (crystalline)       | 24.2 ± 0.5     | 1.008                   | 0.939               | 31.15                                 | 82.6   | NREL                  |
| CIGS                    | 22.9 ± 0.5     | 1.041                   | 0.744               | 38.77                                 | 79.5   | Solar Frontier        |
| CdTe                    | 21.0 ± 0.4     | 1.062                   | 0.876               | 30.25                                 | 79.4   | First Solar, on glass |
| Si (amorphous)          | 10.0 ± 0.2     | 1.001                   | 0.896               | 16.96                                 | 69.8   | AIST                  |
| Perovskite              | 20.9 ± 0.7     | 0.991                   | 1.125               | 24.92                                 | 74.5   | KRICT                 |
| Dye Sensitized          | 11.9±0.4       | 1.005                   | 0.744               | 22.47                                 | 71.2   | Sharp                 |
| Organic                 | 11.2 ± 0.3     | 0.992                   | 0.780               | 19.30                                 | 74.2   | Toshiba               |
| CZTS                    | 10.0 ± 0.2     | 1.113                   | 0.708               | 21.77                                 | 65.1   | UNSW                  |

Also, as the Table 1.1 indicates, the solar cells fabricated from all the materials except crystalline silicon are in the laboratory scale. Studies on crystalline silicon solar cells continue to achieve higher efficiencies and to improve its availability in industry.

#### **1.4. Crystalline Silicon Solar Cells**

Crystalline silicon (c-Si) based solar cells remain to be the most remarkable photovoltaic solar cell technology, accounting for about 95% of the photovoltaic market [70] because of silicon's several beneficial properties: 1. The second most abundant element in the earth's crust. 2. Its sensitivity to the electromagnetic spectrum range emitted by the sun with band gap energy of 1.12 eV. 3. Its non-toxicity and stability. 4- Silicon based solar cells are readily square with the silicon-based microelectronics such as integrated circuits and transistors [71-73]. Among c-Si solar cells, single c-Si cells attract attention with their excellent conversion efficiency.

##### **1.4.1. Fabrication of c-Si Solar Cells**

c-Si solar cells are usually composed of an p-n junction of n-type emitter ( $< 1\mu\text{m}$ ) on a thick (usually  $>100\ \mu\text{m}$ ) p-type c-Si wafers. Although it is available commercially today, solar cells made on n-type substrate are less common. Figure 1.12 demonstrates the fabrication steps of standard c-Si solar cells fabricated on p-type substrate. Fabrication process steps are also described below.



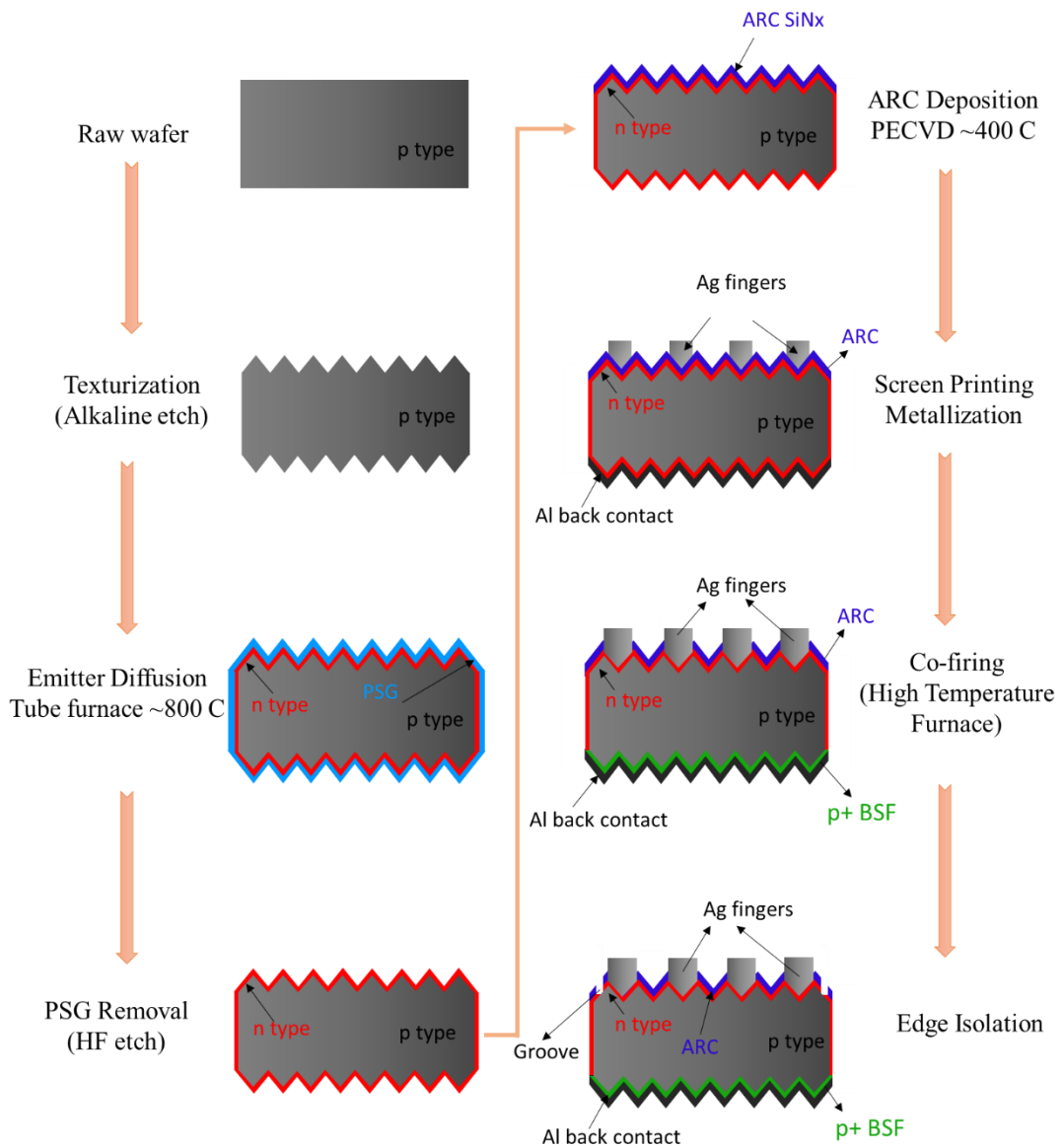


Figure 1.12. Fabrication process of conventional crystalline Si solar cells.

**Surface Texturing:** The band gap energy of silicon (1.12 eV) corresponds to a wavelength of 1100 nm. The photons whose energy are less than 1.12 eV, i.e., high wavelength region of the solar spectrum, are not absorbed by Si to create electron-hole pairs. As a result, almost 50% of solar radiation cannot be absorbed by Si. As it is understood from the Figure 1.13, if the Si wafer has enough thickness, then it can

absorb the photons up to 1100-1200 nm. When the thickness of Si is increased, the light absorption is enhanced, however, the possibility of carrier recombination also increases due to longer path length of the generated carriers.

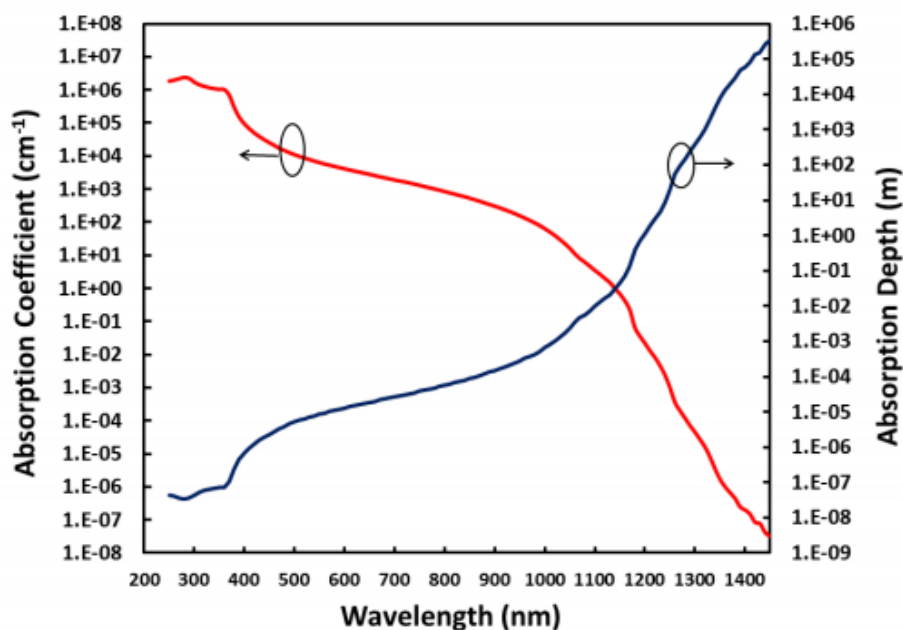


Figure 1.13. Absorption coefficient and depth of intrinsic Si at 300 °K as a function of wavelength [74].

The optical path length is defined by the distance travelled by the photon before it leaves the material. In order to increase the amount of absorption in Si, the path length should be increased either by increasing the thickness of the wafer or employing some light trapping strategies. Increasing the thickness brings along additional cost which is not desirable. Hence, a mechanically thin but optically thick device needs to be developed.

One effective strategy is the texturing of Si surface by wet chemical anisotropic etching of potassium hydroxide (KOH) solution. At the textured Si wafer surface, incoming light is refracted at an angle, not perpendicular to the surface, so that the

light undergoes internal reflections within the material as illustrated in Figure 1.14. As a result, the possibility of absorption of light and thus the carrier generation is increased.

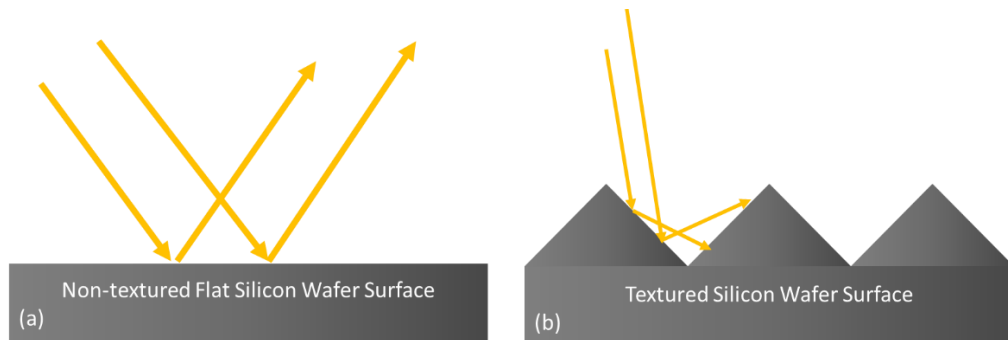


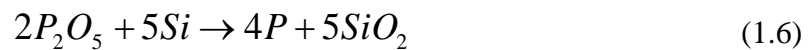
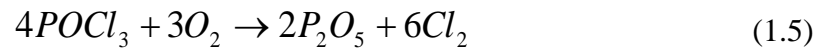
Figure 1.14. Schematic of reflection of light from a) flat and b) textured Si wafer surfaces

**Solid State Diffusion:** P-n junction formed by solid state diffusion is considered to be one of the most critical steps of the solar cell production.

The electrical properties of a crystalline material can be changed via the doping process by adding impurity atoms to the crystal. Si is in the fourth group of the periodic table and forms four covalent bonds with the nearest neighbor atoms. N-type doping of Si is obtained by the fifth group elements such as phosphorus (P), arsenic (As) or antimony (Sb) with five valence electrons. When a five-valence electron atom is added to the system, the four valence electrons establish covalent bonds with the Si atoms. However, the fifth electron, which is not tightly connected to atom, can move easily through the lattice even at room temperature, increasing the conductivity of Si. For p-type doping of Si, third group elements such as boron (B) are widely used. These trivalent electrons cause the formation of covalent bonds with Si atoms, and likewise, the missing electron or excess hole provides an increase in the conductivity.

Doping is achieved by breaking the lattice bonds and rearranging the bonds between the other lattice or impurity atoms. Breaking the lattice bonds and reformation the bonds require high temperature, therefore doping process is usually performed around

800-900°C. In fabrication of a standard solar cell, liquid phosphorus oxychloride (POCl<sub>3</sub>) is used as a P source to form an n-type layer on a p-type Si. POCl<sub>3</sub> is carried to the furnace with nitrogen (N<sub>2</sub>) gas and oxygen gas (O<sub>2</sub>) used to assist in the deposition of POCl<sub>3</sub>:



The P atoms are first implanted in the oxide layer and then diffuse towards the wafers by the concentration gradient. Schematic of diffusion furnace for doping of Si is shown in Figure 1.15. After the doping process, the phosphosilicate glass (PSG) formed on the surface of the wafer is removed from the surface by HF solution.

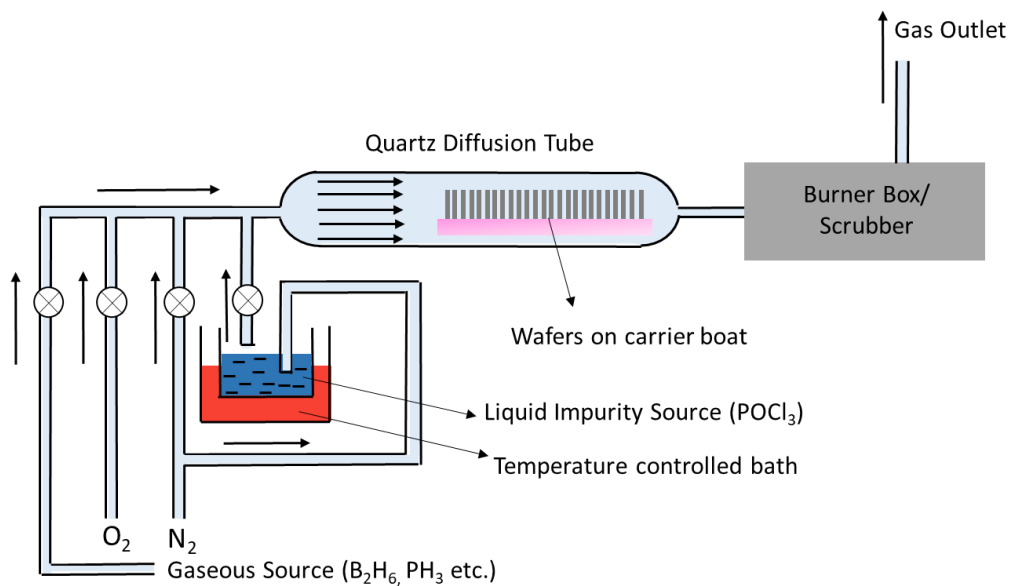


Figure 1.15. Schematic cross-sectional view of a tubular diffusion furnace for solid state diffusion.

**Antireflective Coating:** In solar cell devices, it is desirable to reduce the reflectance ratio as the reflective losses reduce the photovoltaic conversion efficiency. This results in an increase in the number of photons absorbed and hence an increase in the efficiency of the device. In addition to the texturing, which reduces the reflection to certain level, an anti-reflection coating (ARC) is also applied to reduce the reflection values even further. An anti-reflection coating, which is usually a thin layer of dielectric material with a specifically selected thickness, reduces reflection from the surface by an interference effect such that the phase difference between the wave reflected from the top surface of the antireflective coating and the semiconductor surface leads to a destructive interference for certain wavelengths and enabling a net decrease in the reflectance.

When the light enters a semiconductor surface with a refractive index of  $n_s$  from a medium with a refractive index of  $n_0$ , the reflectance,  $R$  is as in Equation 1.7, whereas when this semiconductor surface is deposited with an AR layer with a refractive index  $n_a$ ,  $R$  is given by Equation 1.8:

$$R = \left( \frac{n_0 - n_s}{n_0 + n_s} \right)^2 \quad (1.7)$$

$$R = \frac{(n_0 - n_s)^2 + \left( \frac{n_0 n_s}{n_a} - n_a \right)^2 \left( \tan \left[ \frac{2\pi n_a t \cos \theta}{\lambda} \right] \right)^2}{(n_0 + n_s)^2 + \left( \frac{n_0 n_s}{n_a} + n_a \right)^2 \left( \tan \left[ \frac{2\pi n_a t \cos \theta}{\lambda} \right] \right)^2} \quad (1.8)$$

where  $\theta$  is the angle of incidence. The reflectance takes its minimum for normal incidence ( $\theta = 0$ ), at:

$$n_a = \sqrt{n_s n_0} \quad (1.9)$$

The minimum thickness of an AR coating required for destructive interference is given as:

$$t = \frac{\lambda}{4n_a} \quad (1.10)$$

The refractive index and the thickness of the AR film for lowest reflectance can be calculated using Equations 1.9 and 1.10. Assuming  $n_s = 3.44$  for Si and  $n_0 = 1$  for air, the optimum ARC refractive index is calculated as 1.87. The lowest reflectance at 600 nm which is the highest spectral irradiance of the solar spectrum, is found to be 80.2 nm.

The reflectance spectrum for bare and textured Si with and without deposition of an AR film as a function of wavelength are shown in Figure 1.16. It is deduced from the figure that in the visible range (400-700 nm) the average reflectance of bare Si is ~35%, while the average reflectance of the AR film deposited bare Si is below 15%. When combined with texturing, the average reflectance of the AR film deposited Si is below 10 % and almost zero at 600 nm. This demonstrates the importance of using ARC for more efficient solar cell fabrication.

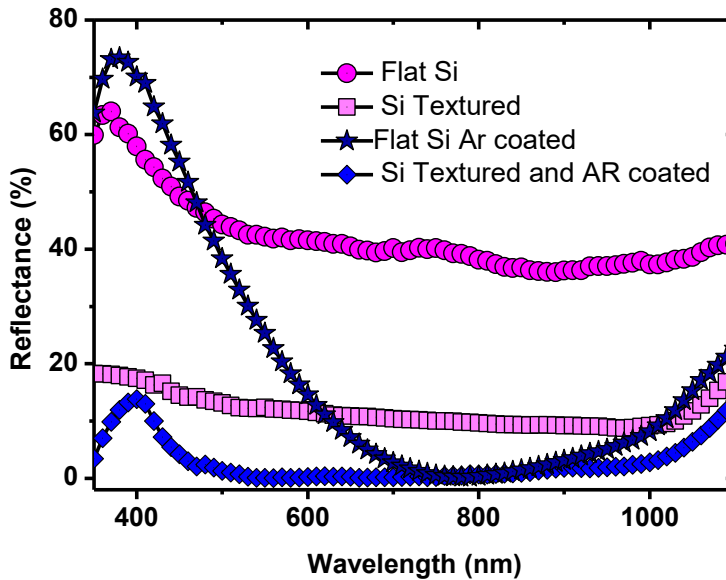
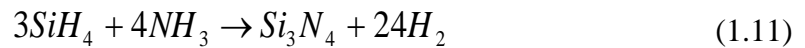


Figure 1.16. Reflectance spectra of flat and textured Si with and without ARC.

In conventional c-Si solar cells, a thin Si nitride layer with a refractive index of  $n_a = 2.00$  is commonly used as AR coating. Following the considerations given above, the nitride layer has the lowest reflectance at 75 nm for a wavelength of 600 nm. Si nitride deposition is carried out with a PECVD system at a temperature of 300-400°C using silane ( $\text{SiH}_4$ ) and ammonia ( $\text{NH}_3$ ) gases with the chemical process;



**Metallization:** In order to collect the generated carriers from the solar cell, metal contacts are necessary. To obtain high efficiency solar cells, the metal grids should be carefully designed and fabricated. Electrically, it influences the fill factor due to grid line resistance and the series resistance through the contact. On the other hand, optically, the metal gridline with high reflecting properties reduces the absorption and hence the short circuit current.

As shown in Figure 1.17 (a), the top contact is composed of busbars and fingers. The current collected from fingers is delivered to busbars which is directly connected to the external load. In order to improve the performance of the solar cells, following crucial points should be taken into the consideration for an optimum top contact design: 1- The larger distance between the fingers causes the greater resistive losses in the emitter. For this reason, the distance between the fingers should be as short as possible. On the other hand, a shorter spacing between the fingers means more fingers on the surface causes more shadowing losses. 2- The greater resistance the metal contacts have, the greater resistance the grid has. Therefore, low resistance metals should be preferred and fingers with high aspect ratio should be formed as shown in Figure 1.17 (b).

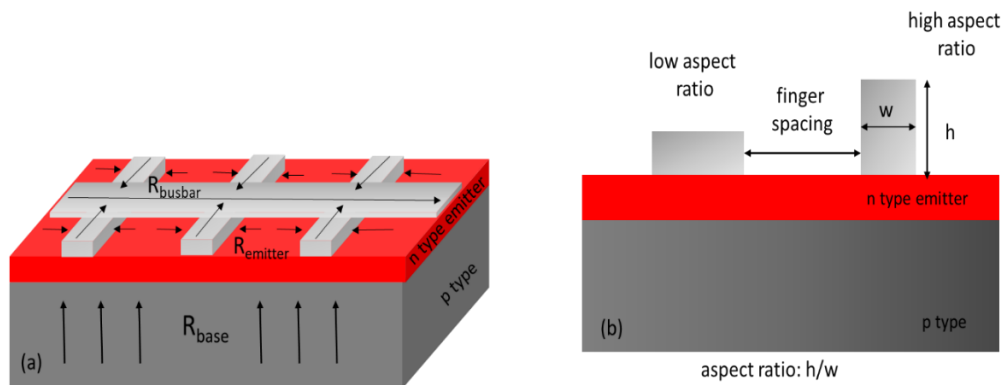


Figure 1.17. (a) Schematic of resistive components and current flow directions, b) Top contact schemes.

In solar cell fabrication, the top and the back contacts are usually formed by screen printing metallization method. In this method, in order to print the grid pattern on the wafer, a squeegee is used to apply force to the metal paste through the mask. Paste quality, pressure and the speed of the squeegee, snap off between screen and sample play an important role in the quality of printing. For front side metallization, grid pattern mask is used to form silver (Ag) finger and busbar contacts while back side metallization mask allows the entire back of the cells to be covered with aluminum (Al). Back surface field (BSF) formation and Ag diffusion through Si nitride layer, ARC, take place in firing process which is one of the most important steps of metallization. Usually, a conveyor belt furnace with multiple heating zones is used for this process. Belt speed and zone temperatures are the crucial parameters to be carefully adjusted for a successful firing process.

**Edge Isolation:** The front contact is connected to the back contact through the emitter around the edge of the solar cell. As a result, the solar cell performance is decreased due to the electron-hole recombination at the edges of the cell.



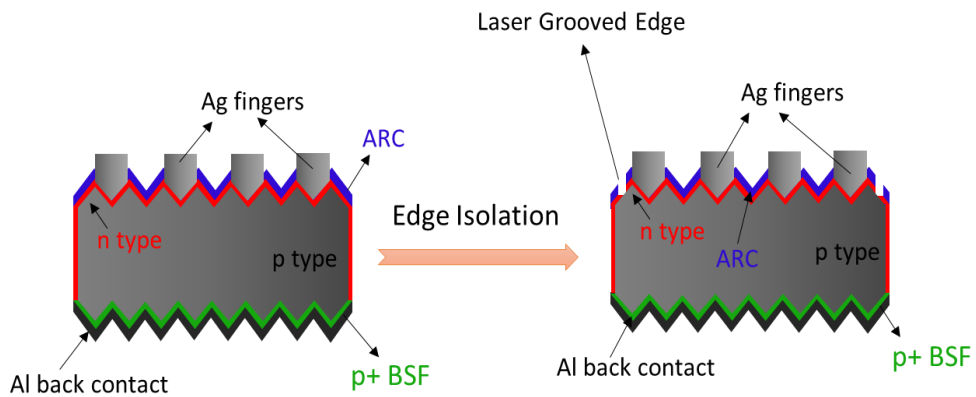


Figure 1.18. Schematic of a solar cell, before and after edge isolation by laser grooving.

By electrically isolating the front and back sides of the cell, short-circuiting problem at the edge can be solved. As illustrated in Figure 1.18, this can be accomplished by laser grooving of the front surface edges until the p-type region is reached.

#### 1.4.2. Low Cost Routes in c-Si Solar Cell Technology

Solar cells are produced on both monocrystalline silicon (mono-Si) and polycrystalline silicon (also specified as multicrystalline, mc-Si) wafers [75, 76]. Mono-Si wafers are generally grown by the Czochralski method [10, 11], while mc-Si wafers are grown by directional solidification. Solar cells fabricated on mono-Si generally have higher efficiency than the cells fabricated on mc-Si due to the crystal defects, however, excellent crystal structure of mono-Si results in high production costs [10-12, 77-80].

Efforts to improve the production rate of the photovoltaic industry while reducing cost have led to the development of new crystallization methods. Thus, solar cells based on mc-Si have arisen as a good alternative. The use of mc-Si has become alluring due to the lower manufacturing cost. However, mc-Si solar cells have lower efficiency values than single c-Si solar cells. Hence, new approaches to improve the performance

are needed. An improved mc-Si solar cell will lead to low cost, high efficiency c-Si solar cell manufacturing, which is highly desirable.

Many PV specialists around the world are working on improvement of the solar cell technology to improve the performance/cost ratio towards the victory of solar energy over the other energy resources. One promising approach in doing so is to develop new solar cell structures which permits the use of relatively lower quality materials like metallurgical Si instead of high-quality electronic grade Si. Low quality materials often have high-level impurities or high density of defects, which lead to low minority carrier diffusion lengths. When they are used as an absorbent base in a planar p-n junction solar cell geometry, carrier collection becomes limited by the high carrier recombination rate. In a solar cell, before carrier collection, a photon creates an electron-hole pair which is separated by a built-in electric field. For the current to be accumulated, generated charge carriers should be able to cross the thickness of the device. That is, for a planar solar cell having a p-type base,

$$L_n > \frac{1}{\alpha} \quad (1.12)$$

and,

$$L > \frac{1}{\alpha} \quad (1.13)$$

where  $L_n$  is the electron diffusion length for p-type base,  $L$  is the thickness of the cell shown in Figure 1.19 and  $1/\alpha$  is the optical thickness of the Si material (from the integration of absorption co-efficient  $\alpha(\lambda)$  over all the wavelengths,  $\lambda$ s).

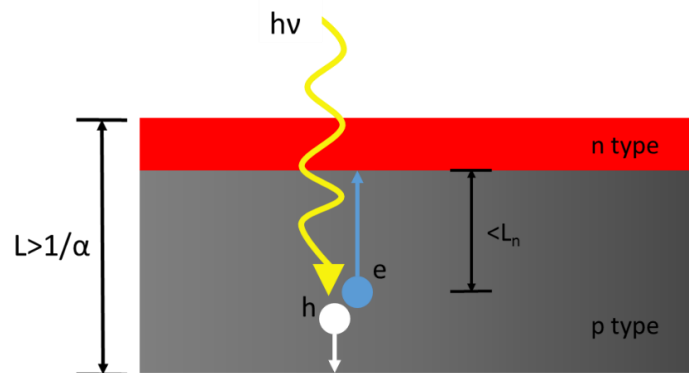


*Figure 1.19. Conventional, planar solar cell design. The cell thickness  $L$  should be greater than the optical thickness  $1/\alpha$  and minority electron diffusion length  $L_n$  should be long enough that minority carriers could reach the junction region before recombination.*

In a planar p-n junction geometry, to produce highly efficient solar cells, the optical thickness of the material should be small enough to collect all carriers generated. However, with its indirect band structure and low absorption property, the thickness of the wafer should be high to maximize the absorption. This dilemma can be solved by introducing light trapping structure that can increase the optical path length through multiple scatterings before the light beam leaves the device. In the case of low-quality material with low diffusion length, it is hardly possible to fabricate high efficiency solar cell with conventional geometry and texturing on thick crystal wafer. In this case, a new device geometry enabling charge collection with short carrier diffusion needs to be developed [81-83].

One potential solution for the design is to separate the directions of light absorption and collection of carriers into orthogonal spatial directions. Orthogonalizing the direction of light and minority carrier transportation was first proposed in 1966, in the form of J. F. Wise's "vertical multi-junction" (VMJ) solar cell [84, 85]. This device has vertical junction concept, i.e. incident light is parallel to junction, rather than a horizontal junction in which incident light is normal to the junction. The advantage of such a device, seen in Figure 1.20, is that many vertically structured junctions provide

higher collection probability for generated minority carriers, hence increase the collection efficiency.

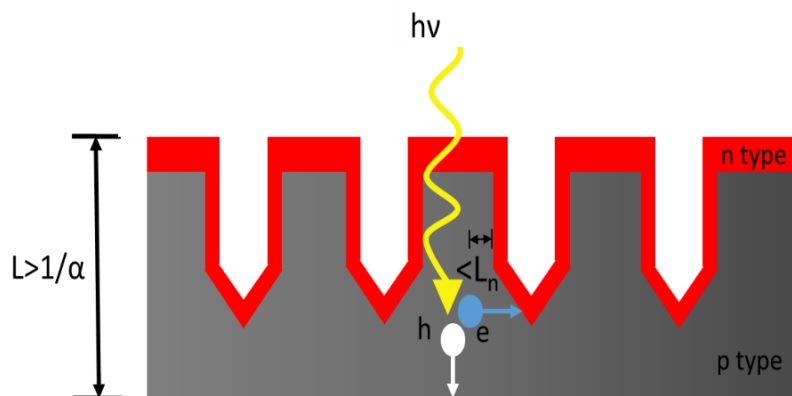


*Figure 1.20. Vertical Multijunction (VMJ) solar cell design. The cell thickness  $L$  should be greater than the optical thickness  $1/\alpha$ , but with this design, the low minority carrier diffusion lengths  $L_n$  can be obtained so that any minority carrier is within the diffusion length.*

A similar idea for increasing the probability of carrier collection was put forward in 1994 [86]. However, as opposed to the vertical multi-junction (VMJ), it was designed in such a way that the junctions would be perpendicular to the incident light, just as in the conventional planar p-n junction solar cells. This idea emerged in the form of a "parallel multi-junction" (PMJ) solar cell, in which the solar cells are composed of consecutive polarity n- and p-type, by connecting similar layers of polarity in parallel, shown in Figure 1.21.

Both designs are similar in that, even in optically thick cells which have low minority carrier diffusion length, the light generated minority carriers are arbitrarily close to charge separation region. Theoretically, in the case of multi junction cells formed with layers thinner than the minority carrier diffusion length, the collection of photogenerated carriers is provided. Moreover, as the material quality is reduced, the performance of the conventional single junction cell is greatly decreased, while multi-junction cell performance remains nearly unchanged. It is also contemplated that multi-junction cells have tolerance to metallic impurities [87]. However, fabrication

of PMJ cells is quite challenging and is not possible with standard Si technology processes. A more realistic structure is to use so called radial junction solar cell structures which will be explained below.

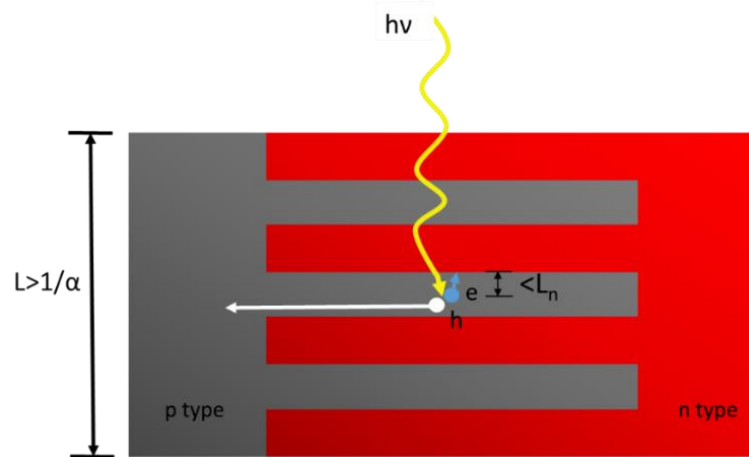


*Figure 1.21. Parallel Multijunction (PMJ) solar cell design. It is necessary that the cell thickness  $L$  should be greater than the optical thickness  $1/\alpha$ , but with this design, the low minority carrier diffusion lengths  $L_n$  can simply be obtained so that any minority carrier is within the diffusion length. Although this minority carrier diffusion and light harvesting direction are parallel, this design has the basic properties of VMJ design.*

In this thesis, the solar cell device consisting of arrays of c-Si micropillars, each with a radial p-n junction, is proposed as a method to provide high efficiency and low cost by enabling the use of low-quality material. The p-n junctions in the radial direction will allow the separation of light absorption and carrier collection in orthogonal spatial directions, as in vertically (VMJ) and parallel multi-junction (PMJ) solar cells. Each individual p-n junction of the cell can be long, where the light enters to the cell, allows optimal light absorption and also the collection of generated carriers on the other direction shown in Figure 1.22.

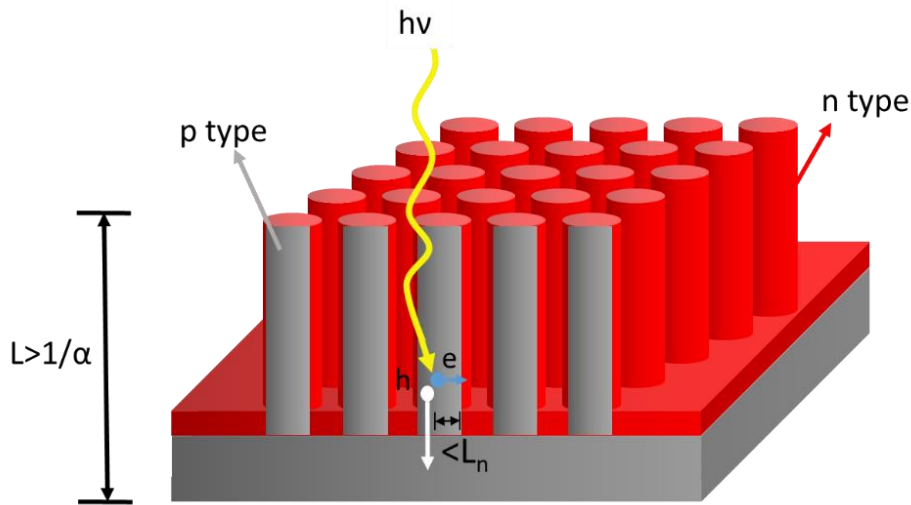


*Figure 1.22. Radial p-n junction solar cell design. It is necessary that the cell thickness  $L$  should be greater than the optical thickness  $1/\alpha$ , but as in the PMJ and VMJ designs, the low minority carrier diffusion lengths  $L_n$  can be obtained so that any minority carrier is within the diffusion length.*

This thesis focuses on the demonstration of radial junction concept using micropillar structures shown in Figure 1.22 and its application to low quality material. A comparison with the planar cells is also given. How radial junction cells can be formed on thin substrates that are highly desirable for lowering the cost is also investigated. Fabrication of micropillars on large surface areas is also a challenging and interesting task from technological point of view. In order to fabricate radial junction solar cells containing micropillars, metal assisted chemical etching (MAE) through photolithography has been employed. The experimental process of forming the radial structure with MAE, the formation of the radial p-n junction solar cell on the high- and low-quality materials, and radial junction cells on thin substrates are discussed.

## CHAPTER 2

### RADIAL JUNCTION FOR SOLAR CELLS

*"I have no doubt that we will be successful in harnessing the sun's energy. If sunbeams were weapons of war, we would have had solar energy centuries ago."*

George Porter

#### 2.1. Introduction

Solar cells are devices that convert the sunlight into the electricity. In crystalline Si solar cells, to achieve this photovoltaic transformation, it is necessary that firstly, electron-hole pairs are generated in the material with absorption of sunlight and then these charges are separated from each other by Coulomb force owing to the electric field built in the space charge region in p-n junction and thus photovoltaic current is created. However, most of the photogenerated carriers are formed outside of the space charge region because in c-Si, this region is usually shallower than the length of the light absorption. Thus, it is necessary for minority carriers to diffuse long enough to reach into the space charge region in order to be separated by the electric field. Therefore, the semiconductor which is used for the device fabrication should be single crystalline and should have as high purity as possible. In this wise, the photogenerated carriers can diffuse further and are more likely to be collected before they recombine. During the production of a solar cell device, it is also important to keep production and material costs as low as possible. However, high purity materials are expensive, and inexpensive materials have high density of defects or impurities.

In recent years, radial junction Si solar cells have been proposed as an alternative device geometry to reduce the cost of fabrication of crystalline Si photovoltaics. This structure has a high-density array of Si pillars enabling to separate the direction of carrier collection from the direction of light absorption [88, 89]. Therefore, it is not required to use high quality but expensive Si material which has a long minority carrier diffusion length. In addition, it has been shown in previous studies that, it is possible to increase the light absorption and the optical path length to values above the classical limit by means of appropriate design in array geometries and with photon management [90].

## **2.2. Literature Review**

### **2.2.1. Enhanced Carrier Collection**

In planar solar cells, in order to ensure efficient absorption of the solar spectrum, the absorption length in c-Si needs a thick absorber layer (Figure 2.1-a), usually thicker than 100  $\mu\text{m}$ . Therefore, in order to increase the collection efficiency, it is necessary to use high-purity, single c-Si for high minority carrier diffusion length. Si material with high impurity and crystalline defects will have a short minority carrier diffusion length due to recombination of electrons and holes [91, 92]. The solar cells, formed from radial p-n junction, enable the directions of the carrier collection and light absorption to be separated orthogonally and thus, makes the length the minority carriers should travel very short [89]. As can be seen in Figure 2.1 -b, the Si material can be thick enough in the light absorbing direction, but thin for carrier collection in the radial direction.



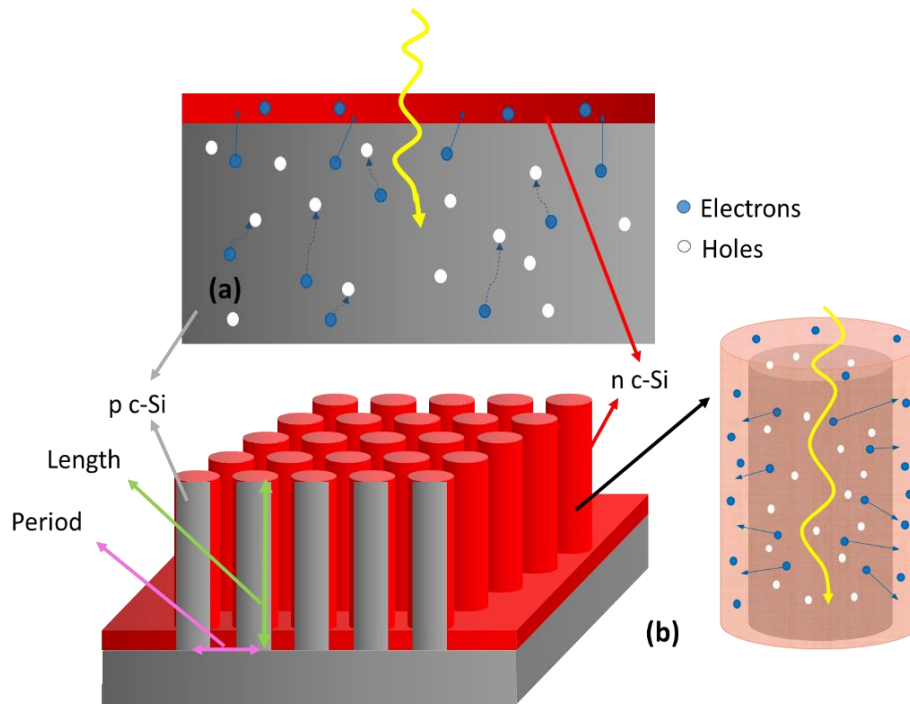


Figure 2.1. Schematic of a) planar and b) radial junction geometries.

Kayes *et. al.* have developed a device physics model for a rod solar cell, each rods with a p-n junction in the radial direction. According to this model, the high aspect ratio in the rods allows the use of a material of enough thickness to provide short collection lengths for generated carriers that facilitate efficient collection of the photogenerated carriers in materials having low minority carrier diffusion lengths. When the carrier recombination rate in the depletion region is not too high i.e., the carrier lifetime is longer than 10 ns, it is mentioned that the radial junction solar cell should provide a great improvement in efficiency compared to planar solar cells. As it is understood from Figure 2.2-a, planar geometries result in low efficiencies due to the traps which exist even only in quasineutral region. However, high efficiency values can be obtained in radial junction geometry despite the traps that exist not only in quasineutral but also in the depletion region. As it is seen in Figure 2.2-b, the high

efficiency values can still be obtained with radial p-n junction geometry even if the trap density in the depletion region is large [89].

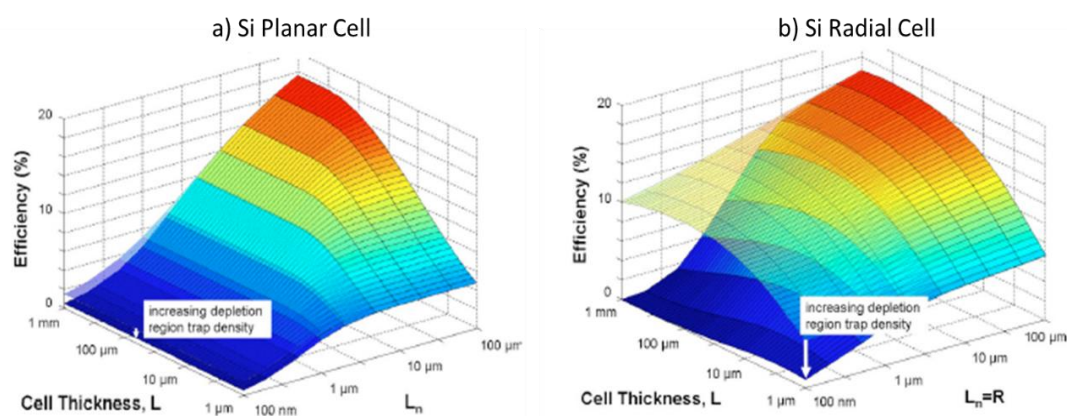


Figure 2.2. Efficiency as a function of cell thickness  $L$  and minority-electron diffusion length  $L_n$  for a) planar p-n junction silicon cell and b) radial p-n junction silicon [89].

Later, M. Gharghi has demonstrated a model based on the collection probability of the generated carriers for radial junction. In that study, the optimum range of the radius of the rods depending on the cell parameters and material qualities was derived. According to the results of the model, the improved efficiency of the cells decreases quickly at the rod radius below the carrier diffusion length [93]. Moreover, both experimentally and theoretically, there are lots of studies in literature about how the radial junction geometry enhances the collection probability and conversion efficiency of the solar cells [90, 94-102].

### 2.2.2. Improved Light Absorption

In order to obtain high efficiency results, improvement in light absorption is important as much as enhanced carrier collection. Previous studies have shown that appropriate design in radial junction solar cells improves the optical absorption [100, 102-105].

In the study of L. Hu and G. Chen the design and optimization process of the periodic silicon wire array structure for optical absorption were analyzed. The effect of different wire lengths on light absorption was investigated. Moreover, a Si thin film which has the same length for the optical absorption,  $2,33 \mu\text{m}$ , was analyzed for comparison. Light absorption results with respect to the photon energy are shown in Figure 2.3. As a result of their calculations, interaction between wires explains the approved absorption of photons in the high frequency regime. Hence, compared to thin films, periodic array structure has small reflection advantage at high frequencies. On the other hand, the enhancement on light absorption at low frequencies could not be achieved since Si has small extinction coefficient at this region. However, using the structures which have longer wires or applying light trapping techniques, higher light absorption can also be achieved at low frequency regime [103].

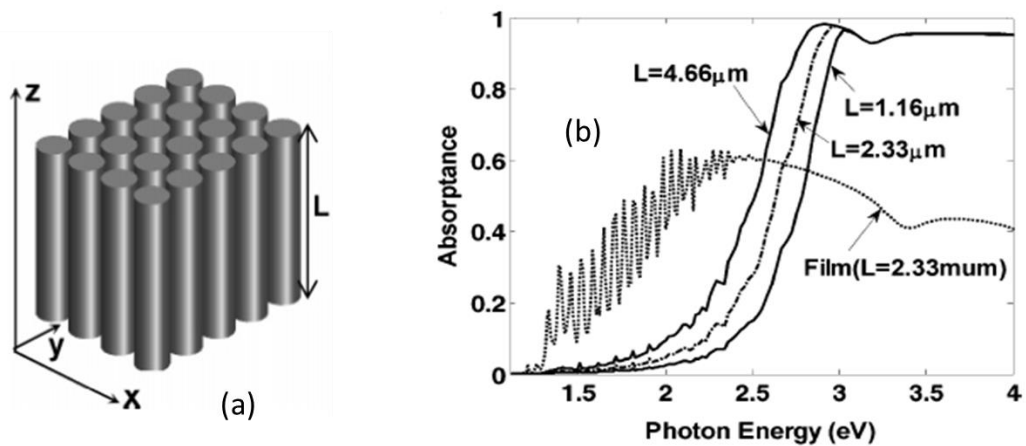


Figure 2.3. a) Schematic of the periodic silicon wire array structure. b) Absorbance of the wires with  $L=1.16, 2.33, \text{ and } 4.66 \mu\text{m}$  ( $d=50 \text{ nm}$ ). The absorbance of a thin film is included as a reference [103].

In another theoretical study [104], the researchers have examined the dimensions of the silicon wires including the diameter, the length of the wires and the filling ratio to determine the optimal geometry for maximum light absorption. According to their

calculations, proper wire diameter and the filling ratio could enhance the light absorption in the structure, by getting electric field through the wires. In their study, the wire length was fixed at  $20\ \mu\text{m}$ , while for the wire radius  $50\ \text{nm}$ ,  $200\ \text{nm}$  and  $3\ \mu\text{m}$  were used. The filling ratio was set to 30%. For comparison, scattering parameters of  $6\ \mu\text{m}$  and  $20\ \mu\text{m}$  thick Si films were investigated.

In Figure 2.4, absorptance, reflectance and transmittance values with respect to wavelength are shown. According to these graphs, wire array geometry has lower reflectance at shorter wavelengths therefore it has higher absorptance than Si film. Moreover, when the radius of the wire is increased, absorption rate decreases.

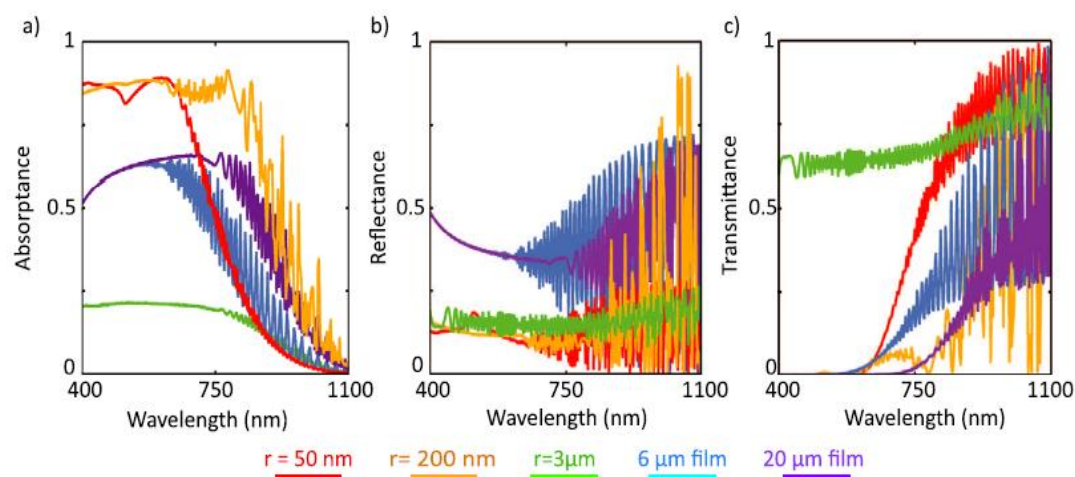


Figure 2.4. (a) Absorptance, (b) reflectance, and (c) transmittance spectra of  $20\ \mu\text{m}$  long Si wires with radii of  $50\ \text{nm}$ ,  $200\ \text{nm}$  and  $3\ \mu\text{m}$ . The parameters of  $6$  and  $20\ \mu\text{m}$  thick Si films are shown for comparison. The filling fraction is fixed at 0.3 [104].

An experimental study on light trapping ability of the wire-array structure provides crucial information on the design of the radial structure [100]. In that work, both planar and radial junctions were investigated using wire array structures. In other words, wire arrays were formed from nano and microwires and as a result, planar and radial junctions were obtained. According to their results, some parameters such as wire diameter and length are also important, however, forming radial junction is a

prerequisite to enhance the performance of the cells. Using capacitance-voltage measurements, these two possible junctions were identified. When the depletion region was very thin, the max capacitance was obtained. As it can be understood from Figure 2.5, The C-V measurements of the 1  $\mu\text{m}$  and 2  $\mu\text{m}$  wire array solar cells show a larger  $C_{\text{max}}$  in comparison to planar and 0.5  $\mu\text{m}$  wire array cell. It was concluded that in the presence of radial junction, larger  $C_{\text{max}}$  is obtained.

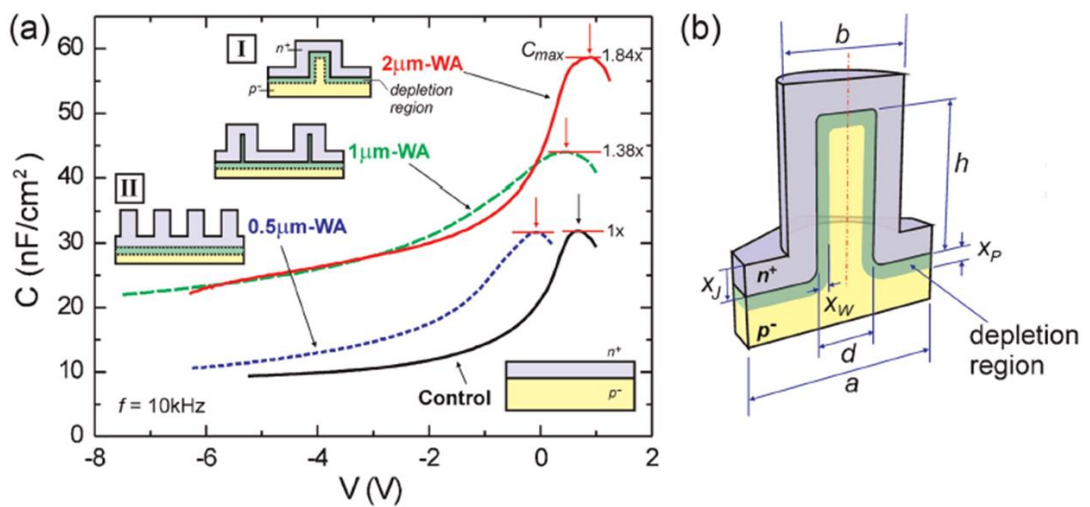


Figure 2.5. (a) Experimental C–V measurement on the wire array structure and reference cells. Wire array solar cells represent two kind of junction: Radial and Planar. (b) Geometry of radial p–n junction structure [100].

According to the result of the theoretical and experimental studies, it is possible to obtain cells with high efficiency by increasing the light absorption and the carrier collection in a cost-effective way using wire array-radial junction cells. However, the important factor here is that the geometry of the radial structure should be suitable for high efficiency. Therefore, the fabrication methods of wire array structure should be examined to obtain the desired geometry.

### 2.2.3. Fabrication of Radial Geometry

At present, there exist two main methods to prepare the wire array structures on substrates (such as Si wafers or glasses), known as “top-down” such as metal-assisted electroless etching [99, 106, 107] and deep reactive ion etching [108, 109]; and “bottom-up” such as vapor-liquid-solid (VLS) growth [90, 106, 110-116], and metal-organic chemical vapor deposition [117].

The first wire array solar cell which consists of p-type/intrinsic/ n-type (p-i-n) coaxial silicon nanowire arrays was fabricated with the help of VLS method [110]. In this approach, which is based on chemical vapor deposition (CVD), a catalyst, mostly an Au film is used to mediate the growth. Firstly, Au film is deposited onto Si substrate. Then the wafer is annealed at temperatures higher than the Au-Si eutectic point to create Au-Si alloy on the wafer surface. As the liquid alloy becomes supersaturated with Si originated from the CVD deposition, Si starts to precipitate to form a wire shape.

In the first wire array solar cell study mentioned above, after the single c-Si wire p-core was synthesized by a nanocluster-catalyzed VLS method, a Si shell of n-type Si was formed using CVD. After the growth of main device structure, SiO<sub>2</sub> was deposited as front surface passivation by means of plasma enhanced chemical vapor deposition (PECVD). Standard electron beam lithography, KOH selective etching to expose p-core and contact deposition on the p-core and n-shell via thermal evaporation were applied to fabricate coaxial nanowire devices having selective contact points on the p-core and n-shell regions. These first wire array cells with single core/shell structure had 230 mV open circuit voltage and the conversion efficiency value up to 3,4% [110]. Later, it was shown that the radial p-n junction of Si wires produced by VLS method is very promising for photoelectrochemical (PEC) solar cells [112, 113].

However, the conversion efficiency values obtained from the radial structured solar cells produced by the VLS method up to that time were below the expected 15% photovoltaic efficiency of the device physics models [89, 95]. In 2010, Putnam et al.

reported up to 7.9% efficiency value via VLS method, using Si substrate whose active volume is equivalent to 4  $\mu\text{m}$  thick wafer [116]. Moreover, their cells had better performance values,  $V_{oc}$  of 500 mV,  $J_{sc}$  values of up to 24  $\text{mA}/\text{cm}^2$  and FF values of above 65%. Figure 2.6 shows the schematic of the radial p–n junction fabrication processes applied. As a catalyst, Cu was used. After wire arrays were formed, samples were etched to remove the catalyst along with a thin layer from the Si surface before the growth of 200 nm thick oxide layer with thermal evaporation. A polydimethylsiloxane (PDMS) layer was coated at the bottom of the wires in order to prevent bottom of the wires to be etched during the oxide removal in HF solution. After removing the PDMS, radial p–n junctions were formed only in the upper region of the Si microwires by phosphorus diffusion with a junction depth of 80 nm.

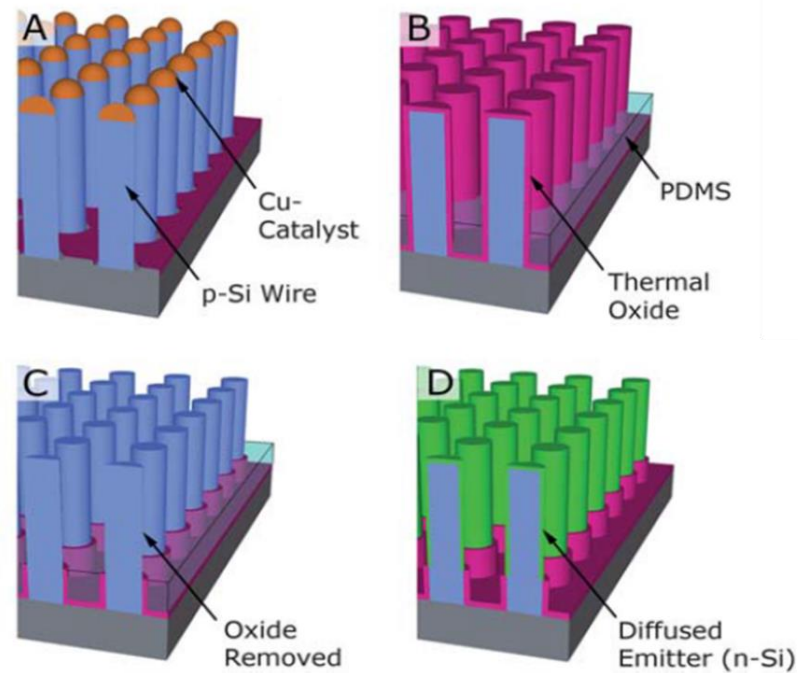


Figure 2.6. Radial p–n junction fabrication process. (a) VLS-grown with Cu catalyst, p-Si microwire array structure. (b) Catalyst removal, thermal oxide growth and PDMS layer deposition. (c) Removal of the thermal oxide. (d) Removal of the PDMS and phosphorus diffusion [116].

Even though VLS growth mechanism is widespread among the bottom up approaches, other mechanisms are also possible for wire growth such as vapor-solid-solid (VSS), vapor-solid (VS) and dislocation-mediated growth [118-121]. The catalyst abides solid rather than forming a eutectic liquid during the VSS process. The precursor disintegration is accelerated by the catalyst due to the phase difference. VS mechanism is based on surface energy difference between the crystal planes on top of the wires to ensure growth rather than using catalysts. The dislocation mediated mechanism relies on defect sites to join the atoms along a threading dislocation causing the growth in the same way.

In the case of bottom-up approach, impurities are introduced during growth, which then cause recombination. Therefore, this approach is not a very suitable for the manufacturing of solar cells. Moreover, the growth requires temperatures to be usually higher than 320<sup>0</sup>C [122]. On the other hand, in the case of top-down approach, Si micro and nanowires are formed by etching Si wafer near room temperature. The resultant wires have the same crystal structure as the initial material. This is a clear advantage of the top-down techniques as the standard Si wafers have perfect crystal structure with low impurity and defect concentration. A lithography step such as e-beam, optical lithography, micro/nano imprint or nanosphere lithography is used to create the mask pattern on the surface [123-125]. After lithography, the patterned surface is etched by deep reactive ion etching (DRIE) or metal assisted etching methods [99, 106-109, 125].

One of the reported studies is summarized as an example here. In this work [109], radial p-n junction silicon solar cells were fabricated by DRIE method. The production steps to obtain radial junction cells were, bead synthesis, dip coating to form single bead layer on the surface, DRIE to obtain wire array geometry, and p-n junction formation by diffusion as shown in Figure 2.7. The SEM image of close-packed silica beads assembled on a silicon wafer is shown in (a). Single-layer silica beads films acted as a mask for (DRIE) with SF<sub>6</sub> to obtain periodic wire arrays seen in (b) and (c).



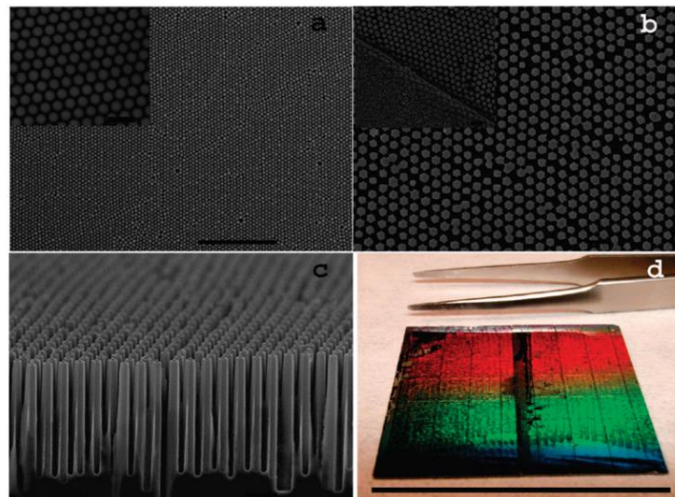
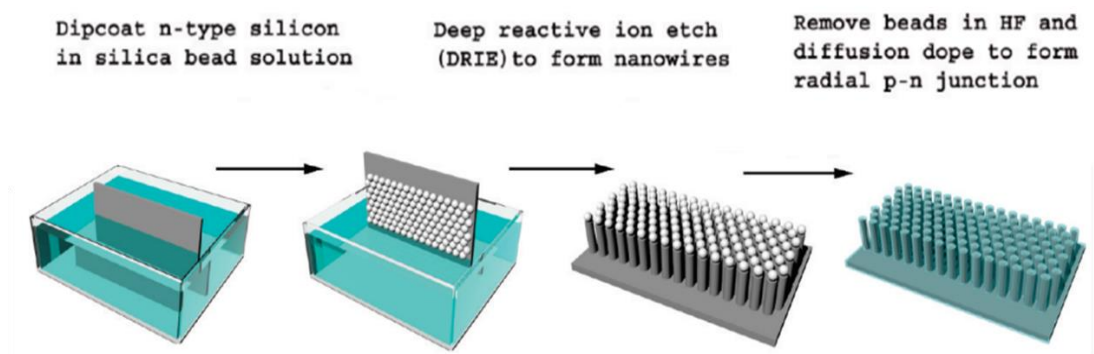
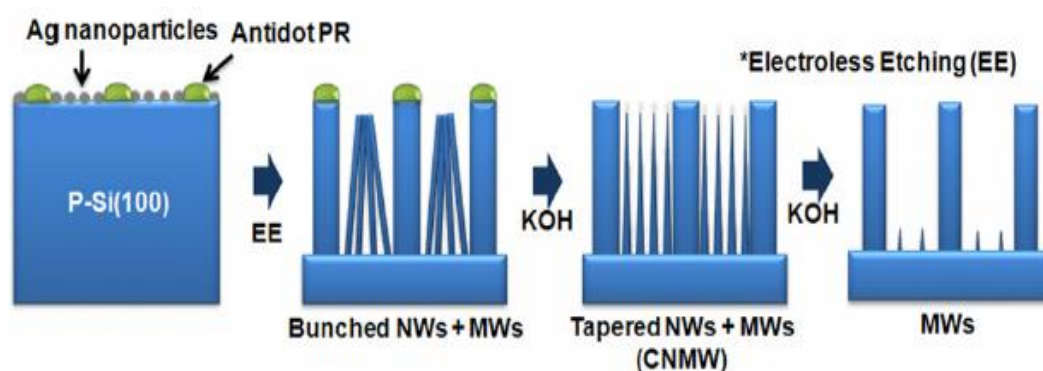


Figure 2.7. Wire array fabrication process (top). SEM images of (a) single layer of silica beads on a silicon wafer, (b) completed ordered silicon nanowire radial p-n junction and edge of finger contact (inset), (c) cross-sectional SEM of the solar cell. (d) Optical image silicon wire radial junction solar cell [109].

In this process, wire radius and separation are controlled by size of the beads while the wire length is decided by etching time. However, since the silica beads are also etched slightly, the resultant wire radii are always smaller than the radius of the initial silica beads. As a result, 390 nm wire diameters were obtained with 8 minutes etching although the bead diameters were 530 nm. After reaching the desired wire length which is 8-20  $\mu\text{m}$ , the silica bead mask was removed by hydrofluoric acid.

Since the initial wafer type is n-type, the process was followed by boron diffusion. According to diffusion equation calculations, junction depth was 160 nm. This means that the p-n junction was a radial junction. The contact formation was obtained by aluminum/palladium sputtering which enabled to fill completely between the wires. As a result, 5-6% efficiencies were obtained from these radial cells.

An alternative and low-cost etching technique based on wet chemical metal assisted etching was developed to fabricate arrays of radial p-n junction microwires and conical nanowires (CNMW) for photovoltaic applications [99]. Metal assisted chemical etching is the method used in this thesis work and will be explained in detail in the next chapter.



*Figure 2.8. Schematic illustration of (CNMW) of MWs and tapered NWs: (1) Deposition of Ag nanoparticles by galvanic displacement following the formation of antidot photoresists. (2) Wire structure formation by MAE. (3) Formation of the CNMW structure by KOH etching (4) Further KOH tapering to obtain only nanowire residues [99].*

Fabrication steps used in the above-mentioned work [99] are shown in Figure 2.8. Si wires were formed on p-type, 1–10 ohm.cm, Si (100) wafer. Before the metal assisted wet chemical etching, circular photoresist dots were periodically patterned by low-level optical photolithography. The photoresist dots determine the radius and the spacing between the microwires. In this work, 1.5  $\mu\text{m}$  thick antidot photoresists with

1  $\mu\text{m}$  radii were defined on the substrates. Later, using the galvanic displacement, silver nanoparticles were deposited on the substrates. The galvanic displacement solution contains de-ionized water, 4.8 M HF and 0.01 M  $\text{AgNO}_3$  and MAE solution contains de-ionized water, 4.8 M HF and 0.5 M  $\text{H}_2\text{O}_2$ . After 20 minutes of etching, micro and nanowire array formations with a length of 10  $\mu\text{m}$  were obtained. Radius of the nanowires and microwires were 25-100 nm and 1  $\mu\text{m}$ , respectively. After cleaning remaining silver nanoparticles and photoresist in nitric acid and acetone, 30% KOH solution at 20  $^\circ\text{C}$  for 60 sec. was used to make the ends of the nanowires sharp. Increasing the KOH etching time resulted in a decrease in the areal density of tapered nanowires which then disappeared at 240 s. As a result, a rugged surface morphology on the samples were observed. The two major benefits of this work are the optical absorption enhancement with tapered nanowires due to multiple scatterings and the electrical improvement with the micro-sized wires due to the increased junction area. The considerable cell performance from tapered nanowires and microwires with a  $V_{oc}$  of 500 mV, a  $J_{sc}$  of 20.59  $\text{mA}/\text{cm}^2$ , an FF of 69.78% and a conversion efficiency of 7.19 % were achieved.

### **2.3. Challenges in Radial Junction Solar Cell Technology**

Significant achievements have already been obtained in many studies including ours presented in this work (Table 2.1). However, many problems arising from the electrical degradation are to be solved for an actual application of this approach to industrial scale. These problems are listed and briefly discussed below:

1. Fabrication of radial structures with uniform geometry and distribution.
2. Fabrication of the structures on large surface area.
3. Replacing the expensive photolithography technique with a cost-effective production technique.
4. Passivation of the large surface area created by radial structures.

Table 2.1. A summary of different types of radial junction solar cell results.

| Description  | Geometry  | Method  | Jsc<br>(mA/cm <sup>2</sup> ) | Voc<br>(mV) | FF<br>(%) | Efficiency<br>(%) |
|--|---|---|------------------------------|-------------|-----------|-------------------|
| J-Y Jung et al., Al-BSF solar cells, 2010 [99]             | Combination of nanowires and microwires, 10 $\mu\text{m}$ in length and 2 $\mu\text{m}$ in diameter | low-level optical lithography followed by MAE | 20.59                        | 500         | 69.78     | 7.19              |
| M. C. Putnam et al., Flexible c-Si solar cells, 2010 [116] | Microwire arrays, 43-49 $\mu\text{m}$ in length and 2-3 $\mu\text{m}$ in diameter                   | VLS   | 24                           | 500         | >65       | 7.9               |
| H. P. Yoon et al., Al-BSF solar cells, 2010 [108]          | Microwire arrays, 25 $\mu\text{m}$ in length and 7.5 $\mu\text{m}$ in diameter                      | Optical lithography and DRIE                  | 20.0                         | 560         | 78.1      | 8.7               |
| J. D. Christesen et al., HIT solar cells, 2012 [97]        | Nanowire arrays, 2 $\mu\text{m}$ in length and ~260 nm in diameter                                  | VLS   | 9.8                          | 441         | 69        | 2.99              |
| G. Jia et al., HIT solar cells, 2012 [126]                 | Nanowire arrays, 900 nm in length and 300 nm in diameter  | MAE   | 27                           | 476         | 56.2      | 7.29              |
| M. Ghargi et al., HIT solar cells, 2012 [94]               | Microwire arrays, 22 $\mu\text{m}$ in length and 20-30 $\mu\text{m}$ in diameter                    | Photolithography followed by DRIE             | 31.1                         | 591         | 66.4      | 12.20             |
| H. Shen et al., al., HIT solar cells, 2013 [96]            | Micropillar arrays, 10 $\mu\text{m}$ in length and 8 $\mu\text{m}$ in diameter                      | DRIE  | 23.6                         | 550         | 75.4      | 9.8               |
| G. Jia et al., HIT solar cells, 2014 [127]                 | Irregular shape nanowire arrays, 500-600 nm in length   | MAE   | 20.2                         | 530         | 82.19     | 8.8               |

|  |  |                                |      |       |      |      |
|--|--|--------------------------------|------|-------|------|------|
| H-D. Um et al., Al-BSF solar cells, 2015 [101]     | Microwire arrays, 10 $\mu\text{m}$ in length and 2 $\mu\text{m}$ in diameter     | MAE                            | 33.2 | 547.7 | 71.3 | 13.0 |
| K. Lee et al. Al-BSF solar cells, 2016 [102]       | Microwire arrays, 10-30 $\mu\text{m}$ in length and 2 $\mu\text{m}$ in diameter  | Photolithography and DRIE      | 33.8 | 573   | 76.0 | 14.7 |
| K. Lee et al. Al-BSF solar cells, 2016 [102]       | Nano/micro hybrid, 10-30 $\mu\text{m}$ in length and 2 $\mu\text{m}$ in diameter | Photolithography, DRIE and MAE | 39.1 | 581   | 75.8 | 17.3 |
| G. Baytemir et al. Al-BSF solar cells, 2017 [128]  | Microwire arrays, 6 $\mu\text{m}$ in length and 4 $\mu\text{m}$ in diameter      | Photolithography and MAE       | 38.9 | 583   | 68.8 | 15.6 |
| I. Hwang et al. Al-BSF thin solar cells 2018 [129] | Microwire arrays, , 30 $\mu\text{m}$ in length, 2 $\mu\text{m}$ in diameter      | Photolithography and DRIE      | 34.6 | 570   | 76.2 | 15.0 |

In order to benefit from the advantages of radial junction commercially, these important problems must first be addressed and overcome. It is relatively straightforward to obtain uniformity in geometry and distribution. However, some limitations exist in determining the size of the structures. Despite some challenges, fabrication of radial geometry on a large surface area is still possible with the current lithography approach. However, for a cost effective and mass production, photolithography is not a suitable technique. One of the most challenging problem is the high recombination rate on the surface of large amount of surface created by the radial structures. This surface has a rough and defected structure after the etching process, which provides an easy path for carriers to recombine. These defect structures need to be passivated in order to obtain high carrier life time, which is necessary for a high efficiency solar cell.



## CHAPTER 3

### METAL ASSISTED ETCHING THROUGH PHOTOLITHOGRAPHY: MICROPILLARS ON P-TYPE MONOCRYSTALLINE SILICON

*“We have this handy fusion reactor in the sky called the sun, you don't have to do anything, it just works. It shows up every day.”*

Elon Musk

#### 3.1. Introduction

Silicon, which maintains to be the most crucial material for semiconductor technology, is promising for the fabrication of devices in various technologies such as solar cells [94, 97-117], opto-electronics [111] and nanoelectronics [130, 131] with its micro-nano structured surface. The parameters such as crystalline quality [132], crystalline orientation [133, 134], size and orientation of the used crystal silicon material [135] affect the properties of these structures [136] and therefore the applications of the produced devices. Hence, it is very important that the fabrication steps of the micro-nano structures should be controlled in a very precise way.

As mentioned in the previous chapter, several top-down and bottom-up methods such as VLS, RIE and MAE have been developed to form Si micro-nano structures. Among these methods, MAE has attracted considerable attention in recent years due to its low cost and simplicity. It is a method that can be implemented entirely using chemicals, which do not require any expensive equipment. The second important feature is that the parameters such as cross-sectional shape, radius, length, crystal orientation, doping type and level can be controlled. For example, regardless of the crystal orientation of

the substrate, various methods have been developed to form vertical or inclined micro-nanowires, although the chemical etching method is inherently anisotropic [137, 138]. In addition, it is possible to grow only circular-base wires by other methods such as VLS, while the different shapes can be formed by the MAE method. The wires that are formed on the monocrystalline substrates by MAE are generally rougher than those obtained by VLS growth, however, they usually exhibit better crystalline quality. Moreover, RIE tends to cause defects close to the etched area, which in turn leads to the production of lower efficient devices, for example by forming recombination regions in the solar cells. On the other hand, wires obtained by MAE do not contain crystallographic defects even they are rougher [132]. In addition, MAE can be used to grow micro-nanostructures on not only Si but also some other semiconductors such as Gallium Arsenide (GaAs) [139, 140] and Gallium Nitride (GaN) [141]. Micro-nano structures by MAE have been demonstrated to be applicable to many areas from solar energy conversion [99, 106-109, 125, 135, 136] to thermal power conversion [142] and chemical and biological sensing [143-145]. Hence, the MAE method is increasingly attracting attention for the formation of micro-nano structures.

Since it is the method applied in this thesis study to fabricate the radial geometry, first, the theory behind the MAE method is explained in the following section, and then experimental results of MAE with the aid of photolithography method used for the formation of these structures are given.

### **3.2. Metal Assisted Etching**

Although it is well known that MAE is a galvanic process based on the oxidation and dissolution of silicon, it has been the subject of debates since it was first reported by Dimova-Malinovska et al. in 1997 [146]. In general, in metal assisted etching, a substrate, which is partly covered by a noble metal, is exposed to an etchant, consisting of an oxidative agent and HF. This noble metal, which can be in two different phases, acts as a catalyst in the etching reaction. The first of these is the liquid phase, usually



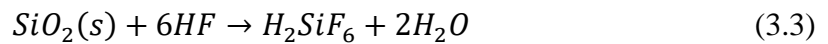
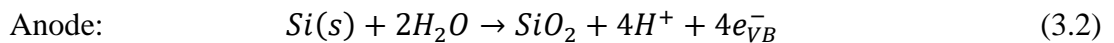
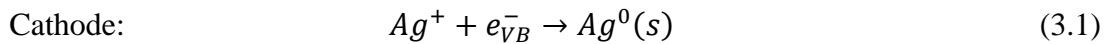
metal salt, and in this case, metal deposition at the surface and etching of the surface occur at the same time. Next phase is the solid phase catalyst which is coated on the surface prior to the etching. As a result, the region beneath the noble metal, acting as a catalyst, is etched faster than the region without the metal.

Basic mechanisms of the MAE technique are described and discussed below.

### 3.2.1. Catalyst Types and Their Reaction Mechanisms

#### 3.2.1.1. Liquid Phase Catalyst

Si sample is immersed into the mixture of HF and metal salt which then decomposes and forms the catalyst in ionic form. The  $\text{AgNO}_3/\text{HF}$  solution is usually used to etch the silicon in liquid phase catalyst etching process. Using  $\text{AgNO}_3/\text{HF}$  solution, Peng et al. [147] described the Ag deposition process during etching, comparing the Si energy levels and the metal reduction potentials. By the attraction of the electrons from the Si valance band, the  $\text{Ag}^+$  ions reduce to solid Ag since Si valance band energy level is higher than the  $\text{Ag}^+/\text{Ag}$  energy level (cathodic reaction). Hence, the silicon atom, which has lost the valance band electrons, begins to oxidize (anodic reaction) and is then dissolved by HF. The cathodic and anodic reactions are given as,



As can be understood from Figure 3.1 and from the cathode and anode reaction equations, Ag nuclei are formed to create pits on the surface. The resulting Ag nuclei are more electronegative than silicon and therefore attract electrons from Si to become negative and form regions for the subsequent reduction of  $\text{Ag}^+$ . However, while the region underneath the Ag particles is etched, this region, covered by the Ag particles, will continue to grow. If the Ag particles continue to grow and the entire surface is covered, the etching will be terminated. Therefore, metal-assisted etching of Si requires HF to reach the metal-Si interface.

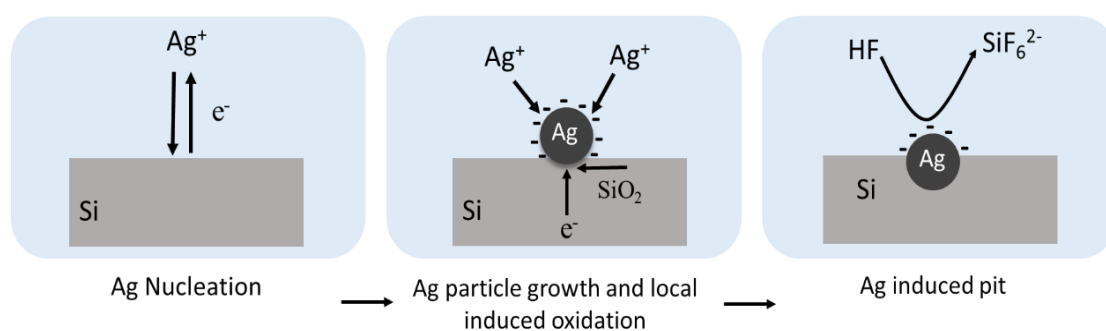


Figure 3.1. Schematic illustration of electroless Ag deposition and etching process on Si wafer immersed in  $\text{HF}/\text{AgNO}_3$  solution.

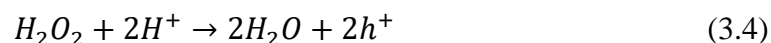
Instead of  $\text{AgNO}_3$ , other oxidants such as  $\text{KAuCl}_4$ ,  $\text{K}_2\text{PtCl}_6$  or  $\text{Cu}(\text{NO}_3)_2$  can be used for the etching mechanism. In these cases, it was observed that the Si wafer surface was induced with Au, Pt or Cu particles [147]. However, although the etching method obtained by forming the catalyst by the electroless deposition method is simple, it is limited in terms of structures obtained on the surface. For example, liquid phase catalyst is not suitable for forming regular structures or for forming microwire-structured surfaces instead of nanowires. Nanowire diameters can only be roughly adjusted by applying oxidants and HF at different concentrations [148]. Catalysts in solid phase are required to obtain structures more regular and desired sizes.

### 3.2.1.2. Solid Phase Catalyst

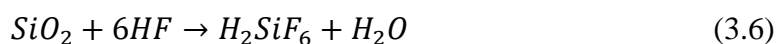
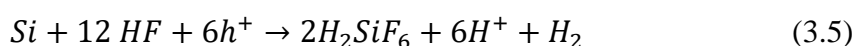
There exist many ways to deposit a solid catalyst on the Si surfaces, such as sputtering, thermal evaporation etc. However, to deposit a thin catalyst layer in desired shape, some methods are used before the deposition, such as photolithography, interference lithography, nano-sphere lithography etc. Hereby, after metal assisted etching, desired structures on the surface are formed. During etching, the regions coated with a thin layer of metal subjected to an etchant solution of HF and H<sub>2</sub>O<sub>2</sub> are oxidized faster and formed SiO<sub>2</sub> is etched by HF to form cavities through the metal precipitates [145]. Noble metals such as Pt [149, 150], Pd [151], Au [152] and Ag [21] are widely used in metal assisted etching. Figure 3.2 shows a schematic representation of the MAE applied to create the desired structures on the surface.

The proposed reaction mechanisms to explain the chemistry of the solid catalyst MAE are given in the following equations:

Cathode: the reduction of H<sub>2</sub>O<sub>2</sub>, which occurs more rapidly around the metal [153],



Anode: Si and SiO<sub>2</sub> dissolution by HF,



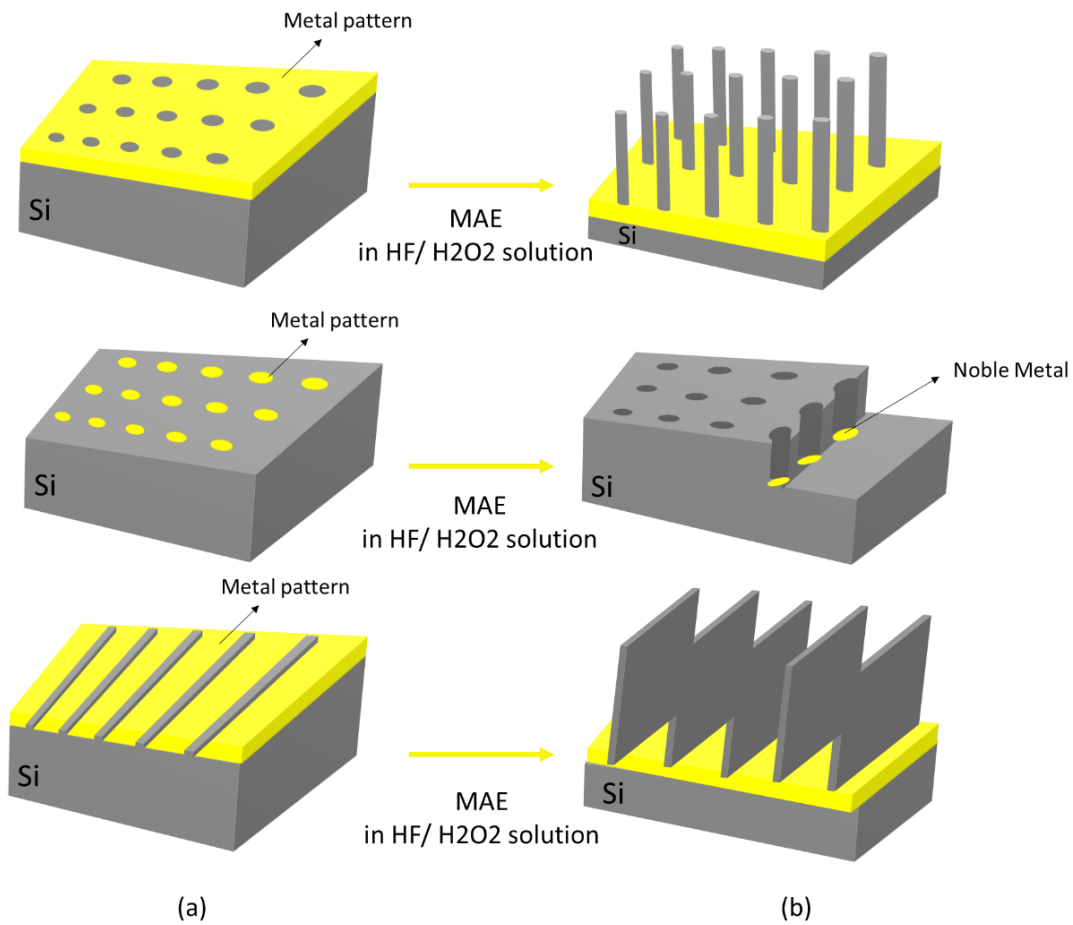
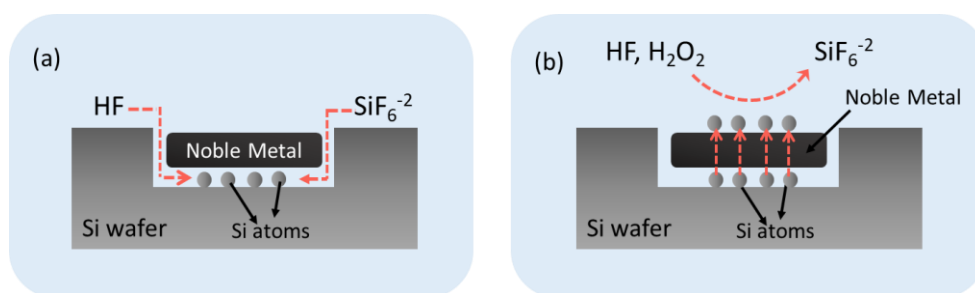


Figure 3.2. Schematic illustration of metal assisted etching of silicon via solid phase catalyst; pillars, holes, sheets a) pre-etching b) after etching.

In the previous section, it has been mentioned that HF must reach the metal-Si interface in order to be able to etch the silicon. For this reason, in the solid-phase catalyst MAE process, it is necessary to deposit metal with desired pattern. This makes the solid phase catalyst more advantageous than the liquid phase catalyst because the catalyst can be patterned with various lithographic approaches prior to deposition in a wide variety of structures on Si, as shown in Figure 3.2, and the desired structures are formed on the surface.

### 3.2.2. Mass Transport

There are two mechanisms proposed for the transport of reagent and byproducts shown in Figure 3.3. According to the first mechanism proposed, which is seen in Figure 3.3 (a), Si atoms are oxidized and dissolved at the interface between the noble metal and the Si substrate, and reagent and byproducts diffuse along this interface [147, 154]. This approach is reasonable for surfaces containing small lateral sized noble metal particles because the diffusion of the reagent and byproducts travel a short distance at the interface before reaching the oxidized region. However, there are no explicit experimental evidence supporting this suggestion for the cases involving larger metal interfaces.



*Figure 3.3. Schematics of proposed mass transport mechanisms for MAE. (a) the reagent and byproduct diffuse along the noble metal and Si substrate interface. Si atoms are oxidized in this interface. (b) Si atoms are dissolved and diffuse through noble metal to the metal and solution interface and are then oxidized in this interface.*

According to the second mechanism proposed, given in Figure 3.3 (b), the back bonds of Si atoms in contact with the noble metal are broken and the free Si atoms diffuse through the noble metal to the interface of the noble metal and the solution where Si atoms are oxidized and etched. The noble metal used for the MAE does not need to have small lateral size in this case. This etching can take place with noble metals in film or particle form [145].

### 3.3. Application of MAE Through Photolithography

In this thesis, the micropillars with cylindrical shape are formed by MAE method. In this section, the methods used to obtain the radial geometry on p-type substrates are described. As shown in the following figure, before applying MAE method, the desired metal shape was obtained by so called lift-off technique followed by the photolithography process. The details of all the steps are given below.

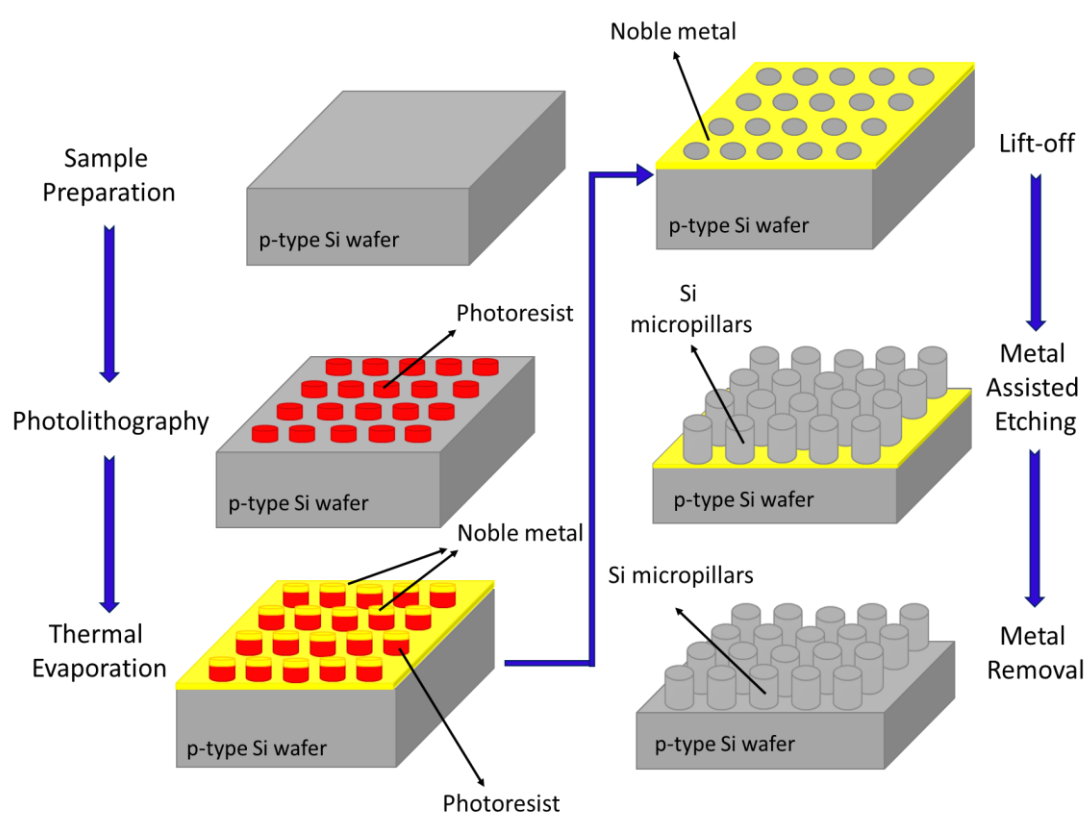


Figure 3.4. Schematic illustration of micropillar array structure fabrication steps.

#### 3.3.1. Sample Preparation

In order to get rid of metallic and organic contaminations, Si wafers were cleaned by two different RCA standard cleaning steps, namely RCA-1 and RCA-2.

In the RCA-1 cleaning, organic contaminations are removed from the Si wafer surface. So-called piranha cleaning can also be used to remove organic contaminations.

First, 300 ml of deionized water (DI water) was mixed with 50 ml of ammonium hydroxide ( $\text{NH}_4\text{OH}$ ) and heated up to  $70\text{-}80^\circ\text{C}$ . Then 50 ml of hydrogen peroxide ( $\text{H}_2\text{O}_2$ ) was added to this solution. The Si wafers were then dipped in the solution for 10-15 minutes. Later, they were rinsed with flowing DI water for 5-10 minutes. Following the rinsing step, the oxide layer formed on the surface was removed using 5% HF solution and then the samples were rinsed again.

In the RCA-2 cleaning, inorganic/metallic contaminations are removed from the Si wafer surface. First, 250 ml of DI water was mixed with 50 ml of hydrochloric acid (HCl) and heated up to  $70\text{-}80^\circ\text{C}$ . Then 50 ml of hydrogen peroxide ( $\text{H}_2\text{O}_2$ ) was added to this solution. The Si wafers were then dipped in the solution for 10-15 minutes. Then, they were rinsed with flowing DI water for 5-10 minutes. Afterwards, the oxide layer formed on the surface was removed using 5% HF solution. After the rinsing and drying, the samples were ready for the photolithography step.

### **3.3.2. Photolithography**

In this thesis, a lift-off technique based on photolithography was used to form the desired metal pattern on the surface prior to MAE. As given in Figure 3.4, it is first necessary to obtain circular dot photoresist (PR) patterns on the surface to form micropillars. After creating circular dot PR patterns on the surface, lift-off process is applied because in addition to the wet or dry etching, the lift-off is a common method to obtain metal patterns with  $\mu\text{m}$  and sub- $\mu\text{m}$  range shapes on the surface. Application and the thickness of the PR layer should be adjusted carefully for a successful lift-off process. After the PR patterns are formed on the surface, the metal film with the desired thickness is evaporated on to the patterned PR film. For a successful application of lift-off technique, an undercut profile at the side walls of the PR pattern and a discontinuity in the metal film are highly desirable as shown in Figure 3.5

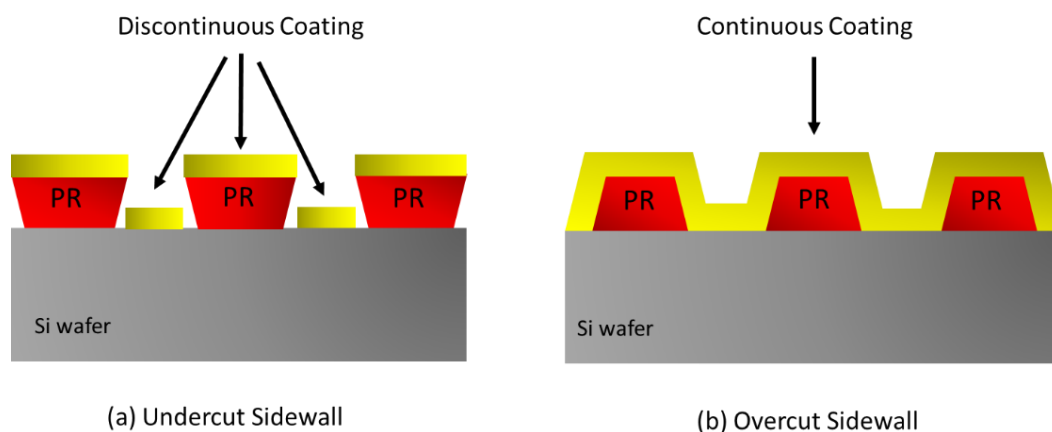


Figure 3.5. Comparison of a) undercut sidewall profile that causes discontinuities in coating and easier lift-off and b) overcut sidewall profile.

Positive PRs do not have crosslink that keeps the softening point up to 110-130 °C. However, since these temperatures frequently occur in typical metal coating, they would be rounded and are completely coated. This makes the lift-off process difficult. Even if the PR features do not soften, positive PRs only allow flat sidewalls, which also causes sidewall coating. On the other hand, negative PRs are designed to create undercut sidewalls. The cross-linking of the resins of the negative PRs helps to protect the undercut during coating even at very high coating temperatures. In this way, the sidewalls are not coated during the metal coating, which facilitates the subsequent lift-off process [155].

In this study, the PR AZ 5214 E was used for photolithography steps. This PR can be used as both positive and negative resist. In this study, image reversal process was applied, and AZ 5214 E was used as a negative mode to have PR patterns with undercut sidewalls.

Compared to the process in which positive PRs are directly used, image reversal process requires an additional image reversal bake after exposure and then flood exposure without a mask. Thus, the sidewalls of the PR show a pronounced undercut profile shown in Figure 3.6.



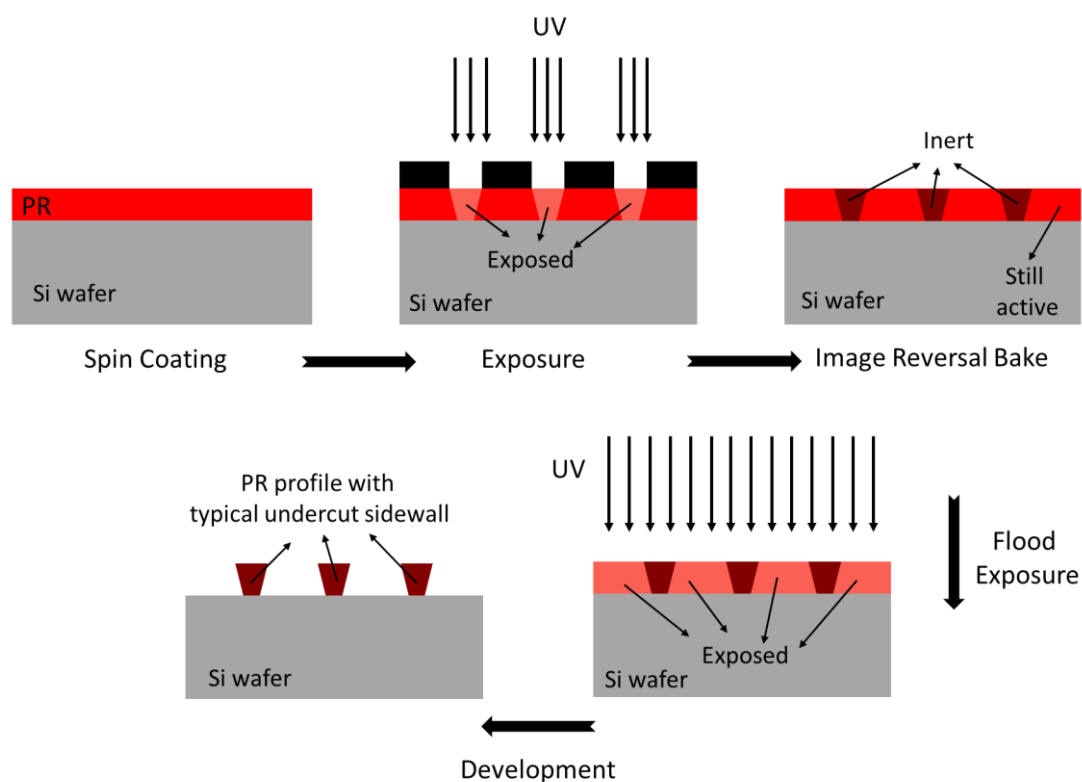


Figure 3.6. Schematic illustration of obtaining undercut sidewall profile by image reversal process

The PR thicknesses were measured by applying the spin speed between 2000 and 5000 rpm with the help of Dektak surface profiler. The results are shown in Figure 3.7. The optimum PR thickness for the subsequent steps of the process was determined as 1.4  $\mu\text{m}$ . For this reason, 3500 rpm was used for the PR coating process. The rest of the photolithography process was carefully optimized and applied in all the radial geometry formation processes on the surface. Following the PR coating on the surface, a pre-bake process for 1 minute at 110 $^{\circ}\text{C}$  temperature and then 30  $\text{mJ}/\text{cm}^2$  UV exposure dose was applied using OAI Model 500 mask aligner system. The image reversal bake that was applied for 2 minutes at 120 $^{\circ}\text{C}$  and then 150  $\text{mJ}/\text{cm}^2$  UV dose was exposed for flood exposure. The samples were developed about 60-70 seconds using the MIF-319 developer.

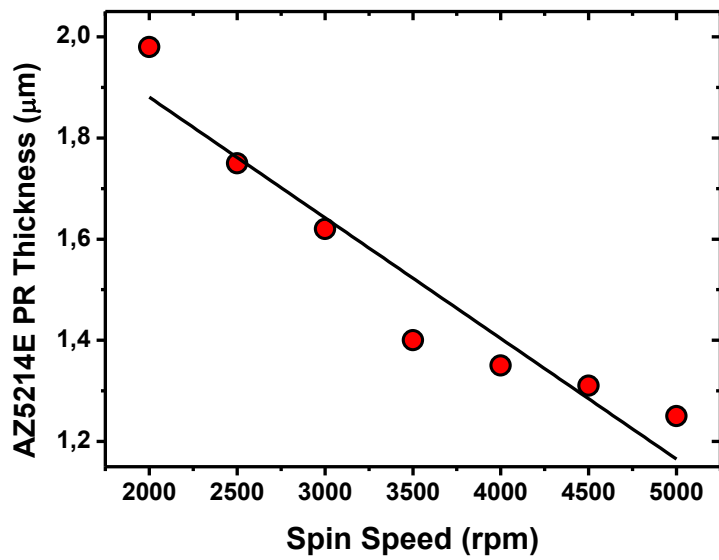


Figure 3.7. AZ 5214 E PR thickness as a function of spin speed.

After all the optimization steps, appropriate PR patterns whose SEM image is shown in Figure 3.8, were easily obtained and the subsequent steps were regularly processed.

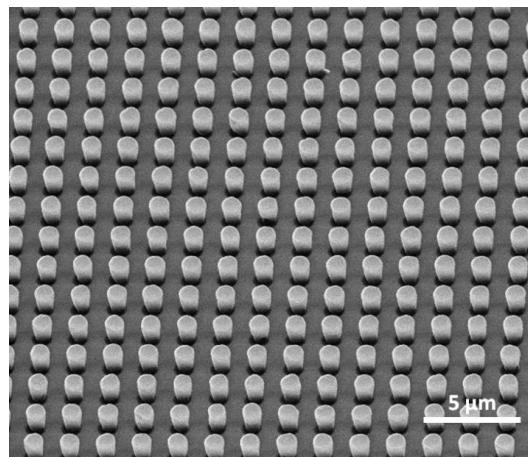


Figure 3.8. Scanning electron microscope image of PR patterns with undercut sidewall profile on Si substrate

### **3.3.3. Thermal Evaporation**

In this thesis, Au was used for MAE process since it has appropriate etch rate as a catalyst for MAE and the thermal evaporation technique was used to coat the Au layer on the PR patterns. As thermal evaporation has unidirectional deposition flux, it at least carries out Au coating of the side walls of the PR patterns and facilitates the subsequent lift-off step.

In the thermal evaporation process, Au was placed in the tungsten boat, the chamber was pumped down with a two-stage pumping system to approximately  $10^{-6}$  Torr. The current was slowly increased to heat the tungsten boat resistively and the coating was carried out.

The deposited Au layer should be neither too thick nor too thin for the lift-off process in order to remove Au on the PR patterns without any problems. Au film with excessively high thickness can be hardly lifted off while a thin layer can be lifted everywhere. In this study, the thickness of the Au catalyst was optimized to be about 20 nm evaporated with a coating rate of 2-2.5 Å/sec.

### **3.3.4. Metal Lift-off**

Lift-off is a simple method to obtain the metal layer with desired patterns on the surface, especially for those noble metal layers such as gold and platinum which are difficult to be removed. During lift-off process, the photoresist under the metal layer is removed with solvent, removing the metal layer on it, and leaving only metal layer which was directly coated on the surface. Ultrasonic agitation helps to break the metal layer at the edge of the photoresist so it can be applied during lift-off.

In this work, the photoresists were dissolved in acetone with ultrasonic agitation for 1 min. after thermal evaporation of 20 nm of Au. As a result, Au layer with circular

holes was left on the samples. An example of such samples before and after lift-off process is shown in Figure 3.9.

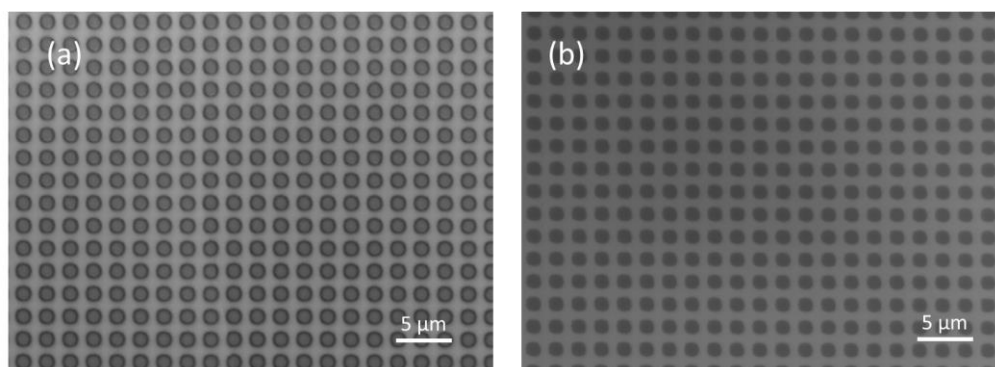
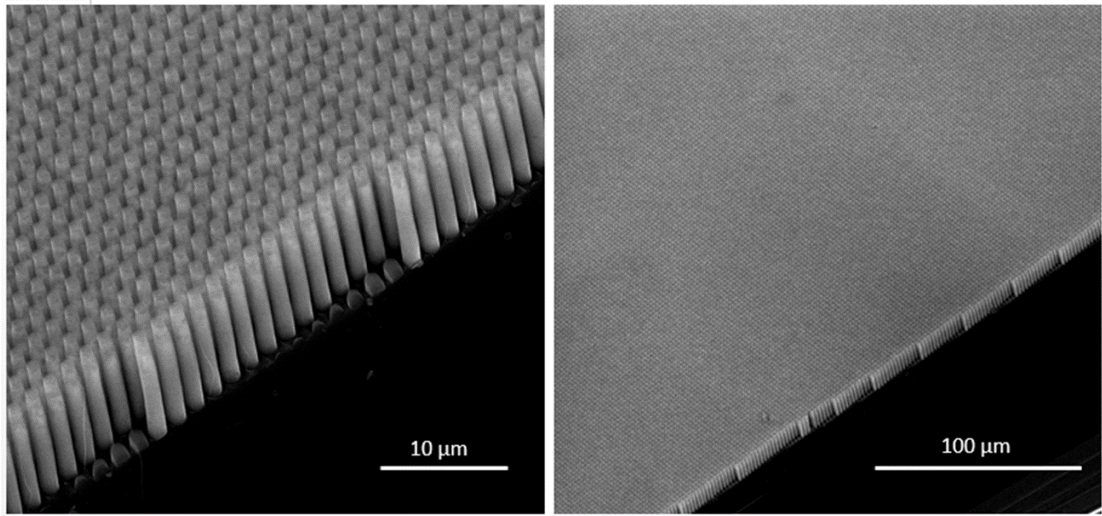


Figure 3.9. Optical microscope images of (a) PR patterns before lift-off, (b) Au layer with the circular holes after lift-off process.

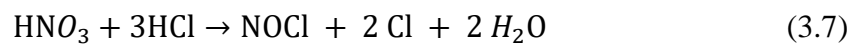
### 3.3.5. Metal Assisted Etching of Si

In this step, the concentrations of HF and H<sub>2</sub>O<sub>2</sub> in the MAE solution were studied. The results are discussed in the next chapter. It was observed that the smoothest etching profile was obtained with MAE solution containing [HF] = 1.8 M and [H<sub>2</sub>O<sub>2</sub>] = 0.4 M, when it was applied to 1-10 ohm.cm, p-type Si wafers with an Au layer of approximately 20 nm thickness. The same concentration was applied for the MAE process for different patterns on Si wafers with the same properties. After obtaining micropillars on the surface by MAE process, the aqua regia solution obtained by mixing nitric acid and hydrochloric acid in a volume ratio of 1: 3 was used to remove the gold layer from the surfaces of the samples. The etch rate of aqua regia is nearly 10 μm/min for gold, at room temperature [156]. Therefore, in order to get rid of the gold layer from the samples entirely, they were immersed in this mixture for 10 minutes after each MAE process. Figure 3.10 shows SEM images of micropillars obtained after 60 minutes MAE applied with 1 μm diameter holes with 2 μm period mesh patterned Au film.



*Figure 3.10. Scanning electron microscope images of micropillars on the surface of silicon wafers at two different magnifications.*

Aqua regia solution has a very strong oxidative effect [156] due to the formation of nitrosyl chloride (NOCl) given in the following equation,



Therefore, the samples were immersed into the HF solution to remove oxide layer from the surface after the etching process. Then they were rinsed again to for final cleaning.



## CHAPTER 4

### **SILICON MICROPILLARS FOR SOLAR CELL APPLICATIONS: RADIAL JUNCTION ON P-TYPE MONOCRYSTALLINE SILICON<sup>1</sup>**

*“The use of solar energy has not been opened up because the oil industry does not own the sun.”*

Ralph Nader

#### **4.1. Introduction**

As understood from its theory mentioned in Chapter 1 and the results of the studies in the literature given in Chapter 2, radial junction solar cells have an alternative device geometry to conventional planar solar cells and have a potential for high optical and electrical performance. This geometry enables the minority carrier collection in the radial direction and thus shortens the length that the carriers travel before they reach the junction. It also optically improves solar cell efficiency by reducing reflection from the surface and increasing light trapping with nano/micropillars on the surface. However, in order to achieve the high electrical and optical performances mentioned above, the nano/micropillars on the surface should have the proper geometry, i.e. diameter, length and period [90].

Since it has perfect crystalline structure without grain boundaries, mono-c Si has the virtue of high minority carrier lifetime. For this reason, micropillar arrays have been

---

<sup>1</sup> The contents of this chapter have been published in 2017, G. Baytemir, F. Es, A. S. Alagoz and R. Turan “Radial junction solar cells prepared on single crystalline silicon wafers by metal-assisted etching” Phys. Status Solidi RRL, **11**, 1600444 and Phys. Status Solidi RRL, **11**, 1770326.

formed on mono c-Si wafers, using metal assisted etching as described in detail in Chapter 3. The geometry, distribution and the shape of the pillars have been studied through a series of experiments, aiming to reach an optimum set of process parameters. Following this optimization processes, solar cells were fabricated on a variety of samples with different pillar configurations. Optical and electrical performances of the solar cells were investigated. As a result, one of the highest reported efficiency achieved from the radial junction solar cells was obtained. It was concluded that such solar cells could be an alternative to traditional planar solar cells.

## 4.2. Experimental Procedures

For solar cell fabrication, 500  $\mu\text{m}$  thick, boron doped, polished mono c-Si wafers with a resistivity of 1-10  $\Omega\cdot\text{cm}$  were used. Radial junction solar cell fabrication steps are given in Figure 4.1. First, RCA-1 and RCA-2 cleanings were applied to the wafers and then the photolithography method was used to define distribution of the micropillar array and the lateral geometry.

In the photolithography step, the openings in the photomask were exposed to 365 nm light at intensity of 30  $\text{mJ}/\text{cm}^2$  after the wafers were coated with AZ 5214 E photoresist by spin coating at 3500 rpm for 45 seconds. The photomask used in this study contains circular opaque structures with a diameter of 4  $\mu\text{m}$  in a period of 6  $\mu\text{m}$ . Following the image reversal process, the samples were exposed to 365 nm light at intensity of 150  $\text{mJ}/\text{cm}^2$  for flood exposure and then non-exposed regions were developed. Subsequently, a 20  $\mu\text{m}$  thick Au layer was coated by thermal evaporation and the circular photoresist dots was removed from the surfaces by ultrasonic agitation in acetone bath. In this way, 6  $\mu\text{m}$  periodically patterned Au thin film on the surfaces with circular holes of 4  $\mu\text{m}$  in diameter was obtained. Finally, c-Si wafers were etched by MAE solution with  $[\text{HF}] = 1.8 \text{ M}$  and  $[\text{H}_2\text{O}_2] = 0.4 \text{ M}$  for 10-90 min. to obtain various lengths of micropillars. The samples were then immersed in aqua regia solution to remove the Au catalyst layer from the surface. Subsequently, with RCA-1



and RCA-2 cleanings, organic photoresist residues, Au residues, and other organic and metallic contaminants were removed from the surface. Later, the samples were immersed in HF: HCl solution in order to remove the oxide layer formed on the surface after RCA-1 and RCA-2 cleanings.

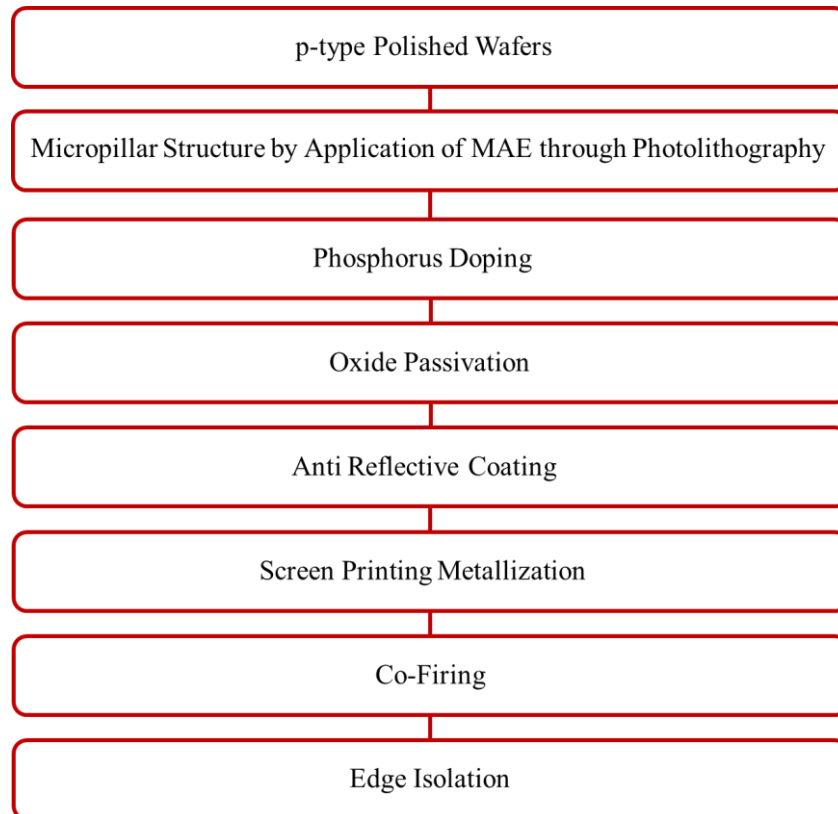


*Figure 4.1. Process sequence for radial junction solar cell production.*

The samples were then doped by phosphorus using SEMCO Engineering LYDOP furnace. In the doping process, using  $\text{POCl}_3$  as source gas, the surfaces were coated with phosphosilicate glass (PSG) film at  $830\text{ }^\circ\text{C}$  temperature for 25 min and P atoms diffused into the samples at drive-in step by annealing for 20 min. PSG layer formed on the surface was removed by HF solution. P atoms distribution profile, as measured by Secondary Mass Ion Mass Spectrometry (SIMS) is shown in Figure 4.2. The

junction depth is estimated to be around 0.4  $\mu\text{m}$  which is much smaller than the diameter of the pillar (4  $\mu\text{m}$ ).

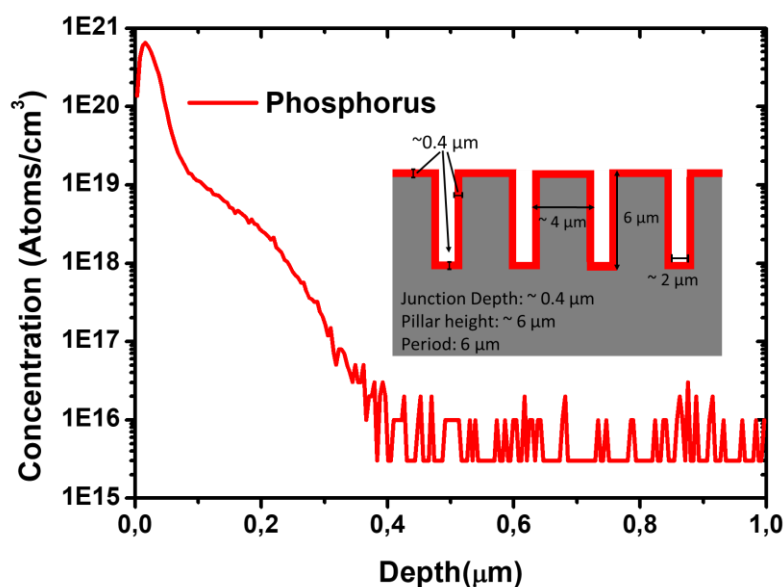


Figure 4.2. Phosphorus diffusion profile measured by SIMS method at EAG Laboratories. The inset shows schematics of radial geometry after doping.

Following the doping process, the surface of the micropillars were passivated with 10 nm dry oxide formation using oxidation tube of the furnace at 830  $^{\circ}\text{C}$  for 30 min. Then, using SEMCO Engineering Direct Plasma PECVD system, as anti-reflecting coating (ARC) with a thickness of around 75 nm of  $\text{SiN}_x\text{:H}$  layer was deposited on the front sides of the samples. In the metallization step, screen printing metallization technique was used to form full aluminum (Al) layer on the back surfaces and silver (Ag) finger and busbar formation on the front surfaces. For the diffusion and the sintering of the metals, 6 zones BTU International conveyor belt furnace was used. However, high temperature processes as co-firing are very delicate to wafer thickness. Due to the thermal capacity of silicon, varied wafer thicknesses result in a differing co-firing temperature profile. Therefore, co-firing conditions were optimized using 500  $\mu\text{m}$  planar cells and then the optimum one which has  $\sim 900^{\circ}\text{C}$  peak temperature, at the

belt speed of 275 cm/ min. applied to radial junction cells. Finally, edge isolation was performed by cutting the edges of the samples mechanically. I-V measurements were performed at room temperature, under AM1.5G by using solar simulator. Metal shadowing due to silver busbar was subtracted to calculate the active solar cell efficiency. Reflection and EQE measurements were performed with an integrating sphere - monochromator setup.

### 4.3. Results and Discussion

#### 4.3.1. Photolithography and Metal Assisted Etching

After photolithography step using 1.5x1.5 cm<sup>2</sup> photomask which contains circular opaque structures with a diameter of 4 μm and a period of 6 μm, rainbow-like color of the samples is seen in Figure 4.3. This diffraction pattern indicates the regularity of the patterns on this large area.

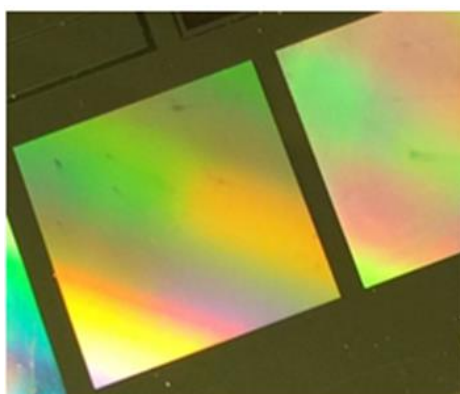


*Figure 4.3. Image of the well-ordered photoresist dots on the sample after photolithography.*

The dependency of the length of the micropillars on the duration of the etching is shown in the Figure 4.4. It was observed that the length of the micropillars increases

linearly with the etching time and the etching rate was calculated as  $0.17 \mu\text{m}/\text{min}$  by using least square fit method.

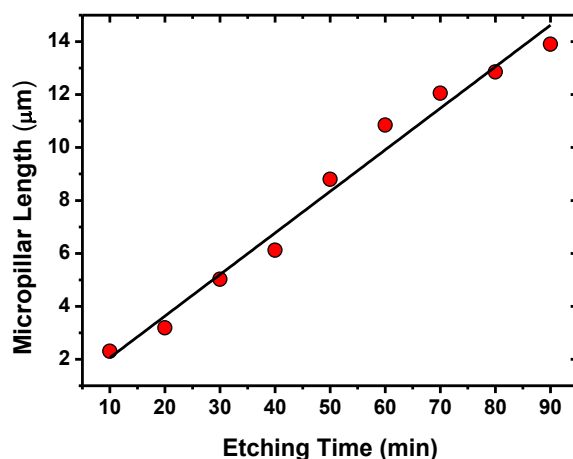


Figure 4.4. Micropillar length with respect to duration of MAE by  $[\text{HF}] = 1.8 \text{ M}$ ,  $[\text{H}_2\text{O}_2] = 0.4 \text{ M}$ ,  $\text{H}_2\text{O}$  solution.

Depending on the etching duration, well-ordered and vertically aligned micropillar arrays obtained in different lengths are shown in Figure 4.5. In the MAE etching mechanism, the extracted holes diffuse to the areas covered by noble metals as explained in the Chapter 3. However, some oxidation/etching process can take place in the regions which are not covered by metal due to the diffusion of extra holes from the metal region. This results in surface roughness outside of the intended region [157]. The etch rate in the lateral direction is much lower than in the vertical direction [158]. Therefore, as understood from Figure 4.5, while micropillars were obtained at nearly the same diameter for different etching times, for long periods of etching, i.e. more than 50 minutes, the side walls and tips of the micropillars began to deteriorate due to slow lateral etching despite the absence of metal. For this reason, in this study, samples with a maximum duration of 50 minutes of MAE were used for radial junction solar cell fabrication.

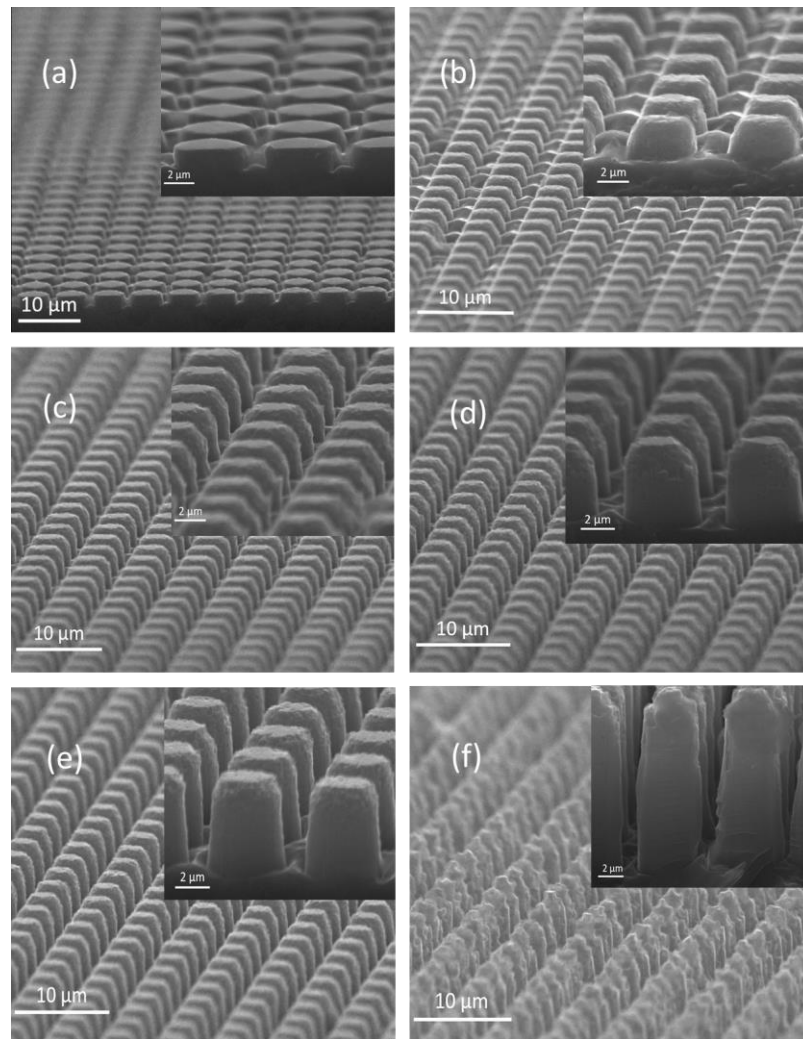


Figure 4.5. Low-magnification and higher-magnification (insets) cross-sectional SEM images of silicon micropillar arrays at length of (a)  $1.7\ \mu\text{m}$  (10 min. etching), (b)  $2.3\ \mu\text{m}$  (20 min. etching), (c)  $3.2\ \mu\text{m}$  (30 min. etching), (d)  $5.0\ \mu\text{m}$  (40 min. etching), (e)  $6.1\ \mu\text{m}$  (50 min. etching), (f)  $13.9\ \mu\text{m}$  (90 min. etching).

### 4.3.2. Reflectance

Figure 4.6 shows the reflectance spectrum of the samples metal assisted etched for 10-50 min. a) before and b) after ARC. The reflection results of planar and pyramid textured samples are also given as a comparison. In this measurement, the wavelength range between 350 nm and 1100 nm was chosen because c-Si weakly absorbs the photons with wavelengths longer than 1100 nm, while the spectral power density is

very low below 350 nm. First, it is clear that the reflectance of samples with micropillars, both before and after ARC, decreased as micropillar length increased. Before ARC, it is seen that, while the samples with micropillars have lower reflectance than the planar one, their reflection results, especially the result of the sample with longest micropillar, 6.1  $\mu\text{m}$ , has a reflectance value which is very close to pyramid textured sample. On the other hand, after the ARC, the pyramid textured sample has very low reflectance compared to the samples with micropillars.

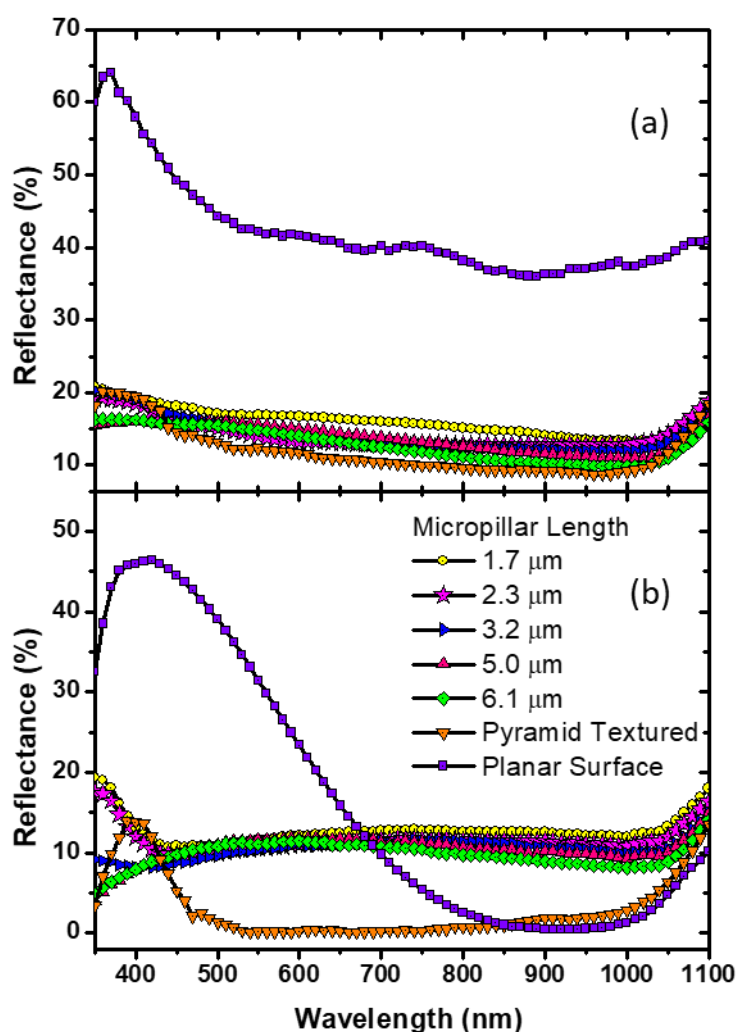


Figure 4.6. Reflectance spectrum for samples having different length of micropillars a) before ARC and b) after ARC. Reflection results of planar and pyramid textured samples were inserted for comparison.

The reflection results can be compared more quantitatively by looking at the AM 1.5G weighted reflection averages before and after ARC coating. The weighted reflection is given as:

$$R_w = \frac{\int_{350 \text{ nm}}^{1100 \text{ nm}} R(\lambda) I_{A.M.1.5 G}(\lambda) d\lambda}{\int_{350 \text{ nm}}^{1100 \text{ nm}} I_{A.M.1.5 G}(\lambda) d\lambda} \quad (4.1)$$

where,  $R(\lambda)$  is the reflectance from the surface at the wavelength  $\lambda$ ,  $I_{A.M.1.5G}(\lambda)$  is the intensity of solar radiation at a specific wavelength  $\lambda$  [159].

AM 1.5G weighted light reflection characteristic of c-Si micropillars with increasing length in comparison with planar and pyramid textured surface are shown in Figure 4.7 with and without ARC.

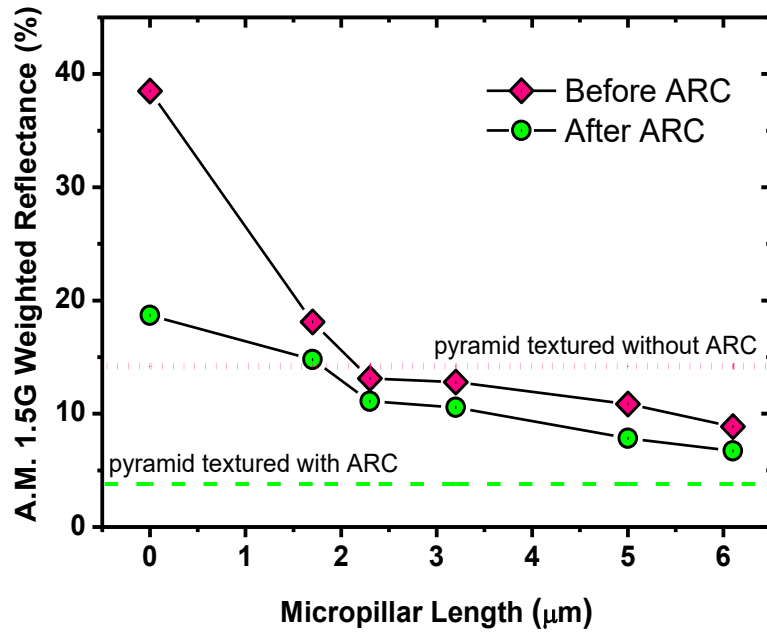


Figure 4.7. Average reflectance for each micropillar length before and after ARC. The length zero is for planar samples. Reflection results of pyramid textured samples were inserted as reference lines.

As expected, both before and after ARC, micropillars showed lower  $R_w$  than planar geometry and  $R_w$  decreased with increasing micropillar length. On the other hand, the average reflection from the micropillar surface remains to be higher than the pyramid-textured surface coated with ARC. The reflection from the micropillar surface can be improved by optimizing the  $\text{SiN}_x$  layer since it is optimized for the pyramid textured surface. However, it should be noted that these results are in agreement with previously reported values for similar surface structures [99, 100, 102].

#### **4.3.3. Optimization of Co-firing Process for Metallization**

Si surface with a 3-dimensional structure requires special metallization process optimization for a good electrical connection to the underlying device. After screen printing of the metal fingers on the front side, an optimization study was performed for the co-firing step. A typical co-firing temperature profile which was taken using Datapaq Thermal Profiling System is given in Figure 4.8. This profile is commonly used for standard solar cell fabrication in our laboratory and applied at a belt speed of 500 cm/min.

In the first part of this curve, that is, until the wafer reaches the melting layer of the Al layer, the organic compounds in the metallic pastes, which allow the paste to adhere to the wafer surface evaporate. This process also provides the diffusion of passivating hydrogen from the  $\text{SiN}_x$  layer to the silicon substrate. When the temperature reaches above  $660^\circ\text{C}$ , the aluminum on the back-side melts and the silicon dissolves in the molten Al forming a Si-Al alloy. During cooling, the silicon is segregated from the melt and recrystallized as the epitaxial Al-doped layer which creates an Al-back surface field. At the peak firing temperature, silver contact formation on the front side is formed. The glass frit in metallic paste digs  $\text{SiN}_x$  layer while Ag particles pass through the molten mixture and form a conductive layer [160].



In order to create good contact formation, co-firing is a very important step. It is seen from the figure, for 180  $\mu\text{m}$  thick solar cells, sintering takes place around 20 sec. Since 500  $\mu\text{m}$  thick wafers were used in this study, we assumed that the sintering would take longer time because of the thermal capacity of silicon.

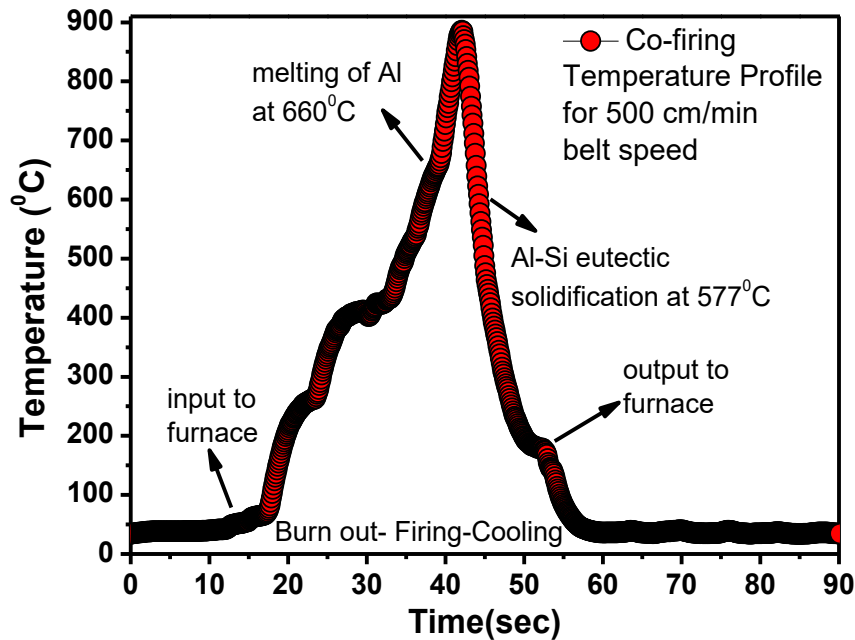


Figure 4.8. A typical co-firing temperature profile for  $\sim 180 \mu\text{m}$  thick solar cells

Therefore, a firing step optimization was performed using 500  $\mu\text{m}$  thick planar solar cells which went through the same processes as the radial junction devices except photolithography and MAE. The results of the experiments are shown in Table 4.1 and Figure 4.9. It is seen that, best solar cell performance is obtained with belt speed of 250 cm/min. Therefore, for our 500  $\mu\text{m}$  thick, three-dimensional radial junction solar cells, a little thinner after the formation of micropillars, 275 cm/min firing belt speed at  $\sim 900 \text{ }^\circ\text{C}$  peak temperature was applied for co-firing step.

Table 4.1. The performance parameters of the 500  $\mu\text{m}$  thick planar solar cells with respect to different firing belt speeds at 900 C peak temperature.

| Firing Belt Speed (cm/min) | Efficiency (%) | V <sub>OC</sub> (V) | J <sub>SC</sub> (mA/cm <sup>2</sup> ) | FF (%) |
|----------------------------|----------------|---------------------|---------------------------------------|--------|
| 150                        | 10.65          | 0.551               | 30.46                                 | 63.46  |
| 175                        | 11.98          | 0.569               | 31.12                                 | 67.67  |
| 200                        | 13.86          | 0.583               | 32.50                                 | 73.17  |
| 225                        | 14.56          | 0.585               | 33.35                                 | 74.63  |
| 250                        | 15.83          | 0.589               | 35.97                                 | 74.72  |
| 275                        | 14.96          | 0.584               | 35.59                                 | 71.98  |
| 300                        | 2.48           | 0.559               | 15.79                                 | 28.13  |

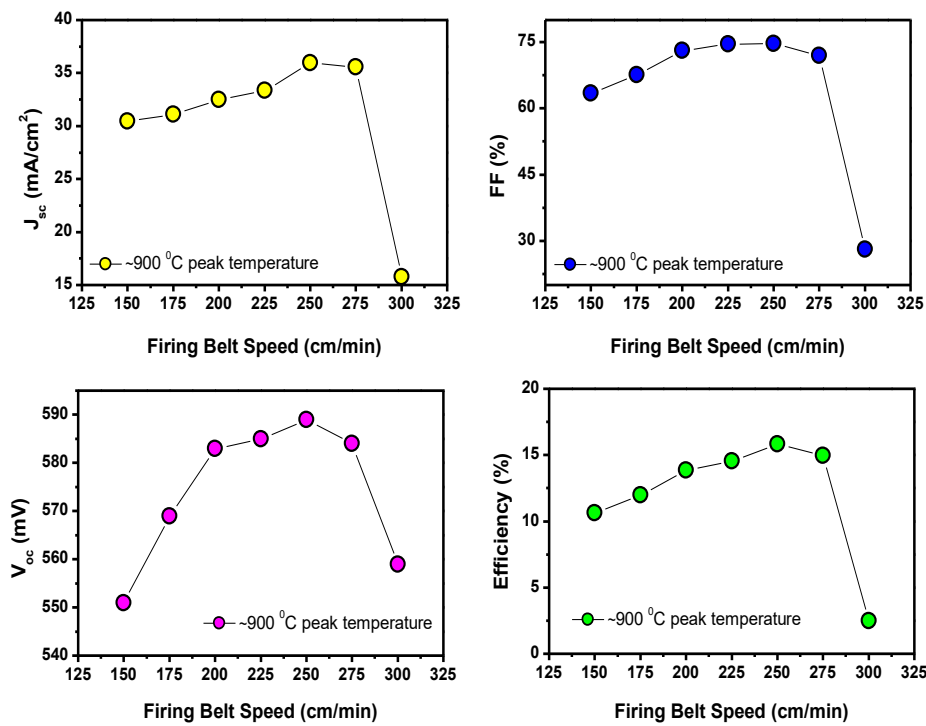


Figure 4.9. The performance parameters with respect to different firing profiles for 500 $\mu\text{m}$  thick planar solar cells

#### 4.3.4. Solar Cell Results

The J-V characteristics of the radial junction solar cells fabricated with different micropillar lengths are shown in Figure 4.10 and corresponding performance values are shown in Table 4.2 and Figure 4.11.

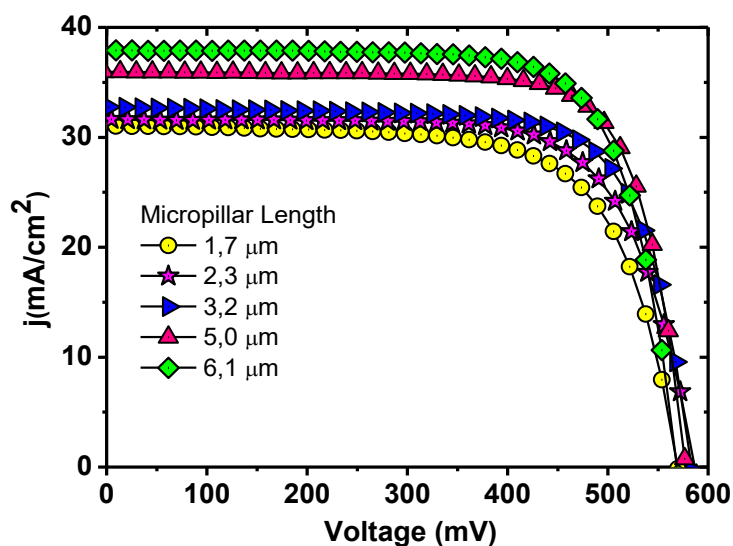


Figure 4.10. J-V curves of radial junction solar cells for different micropillar length.

Table 4.2. Performance Values of Radial Junction Solar Cells with different micropillar length.

| Micropillar Length ( $\mu\text{m}$ ) | Efficiency (%) | $V_{oc}$ (V) | $J_{sc}$ ( $\text{mA}/\text{cm}^2$ ) | FF (%) |
|--------------------------------------|----------------|--------------|--------------------------------------|--------|
| 1.7                                  | 12.2           | 0.570        | 31.0                                 | 69.1   |
| 2.3                                  | 13.2           | 0.587        | 31.6                                 | 71.2   |
| 3.2                                  | 14.0           | 0.583        | 32.7                                 | 73.4   |
| 5.0                                  | 15.4           | 0.577        | 35.4                                 | 75.2   |
| 6.1                                  | 15.9           | 0.575        | 37.5                                 | 74.1   |

It has been observed that the performance of radial junction solar cells increases with increasing micropillar length, which is in correlation with average reflection values. We also see that this increase mainly comes from the increase in the short circuit current density.

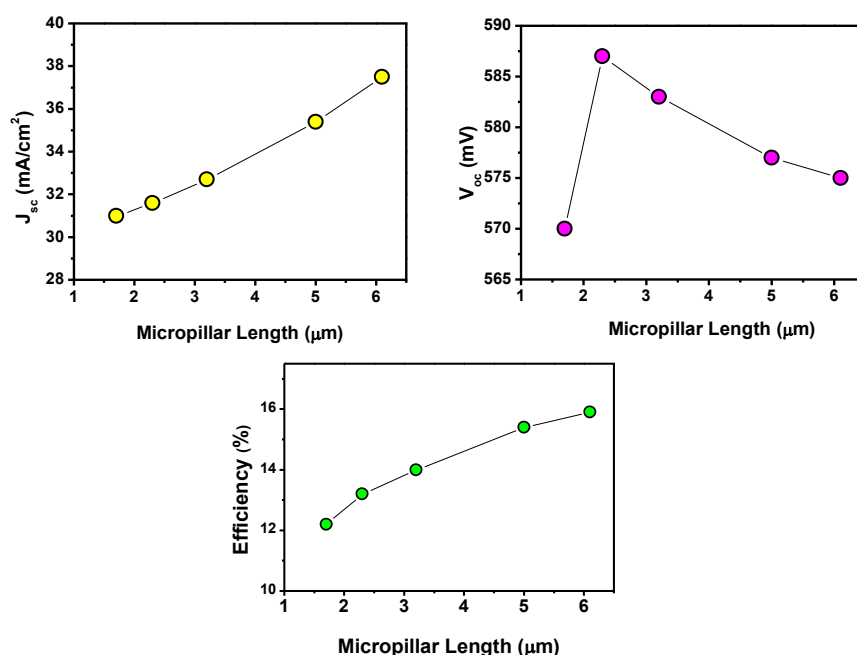


Figure 4.11.  $J_{sc}$ ,  $V_{oc}$  and Efficiency curves as a function of micropillar length

Considering the results of the reflection graphs and the obtained short circuit current density ( $J_{sc}$ ) results, the optical absorption of the cells increases with increasing micropillar length, and therefore the maximum efficiency value was obtained from the cell with  $\sim 6 \mu\text{m}$  long micropillars. In order to understand the mechanisms, the internal quantum efficiency (IQE) spectra of the radial junction solar cells shown in Figure 4.12 were calculated from external quantum efficiencies (EQE) and reflection measurements as a function of wavelength,  $\text{IQE} = \text{EQE} / (1-R)$ . At low wavelengths, IQE provides information about emitter recombination because of the shallow absorption of these photons in Si. On the other hand, high-wavelength photons are

absorbed deeper in Si wafers, so high-wavelength IQE results provide information on minority carrier diffusion length depending on passivation and back surface conditions.

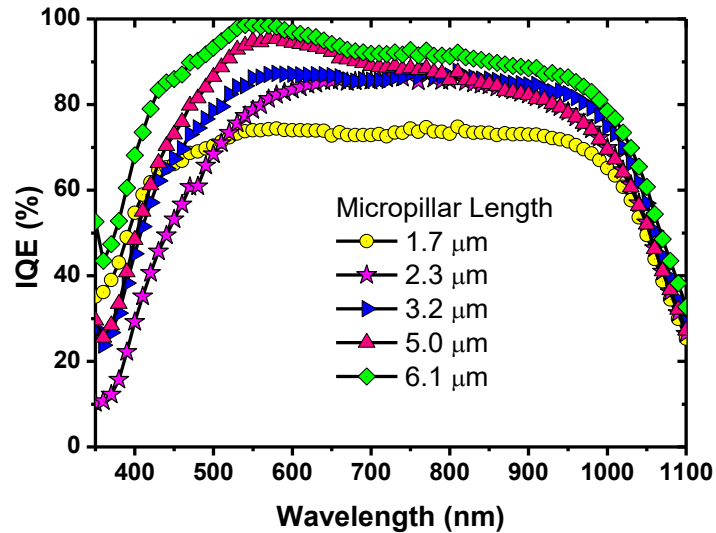


Figure 4.12. IQE spectrum for the Radial Junction Solar Cells with different micropillar length.

Although the sample with minimum pillar length (1.7  $\mu\text{m}$ ) has an unexpectedly low IQE values, which can be related to the experimental errors, other samples exhibit a clear tendency in the IQE measurements. It is obvious that as the micropillar length increases, the blue and then the visible response up to the wavelength of 700 nm of the radial junction cells increase. This increase in the IQE values in the blue region indicates an effective charge collection near the surface of the sample. The presence of the micropillar on the surface has two major effects: one is the effect of radial junction which shortens the length to the junction, the second effect is the light trapping which result from the scattering of the light beam from the surface features. A combination of these two effects is expected to increase the efficiency of the collection in the region close to the junction. The light beam spending more time at the surface region results in more absorption and more effective collection of the electrons due to the presence of radial junction. Another important device parameter

is the open circuit voltage,  $V_{oc}$ , which is a function of the recombination of generated charge carrier. Because of high defect and contamination density, the recombination at the surface is particularly important in solar cell devices. For this reason, increasing the surface area leads to high recombination rate and thus low  $V_{oc}$  values. When the surface is textured with three dimensional structures, like micropillars, the surface area increases significantly, which is expected to have a negative effect on the  $V_{oc}$  values. In agreement with this expectation, the  $V_{oc}$  values decrease with the increasing pillar length as can be seen in Table 4.2 (except for 1.7  $\mu\text{m}$  sample). However, the decrease is surprisingly small indicating that the increase in the surface area does not have a detrimental effect on the  $V_{oc}$  values.

Another way of looking at the device properties is to analyze the dark J-V curve from a fundamental device point of view. Dark J-V curves of cells with planar and radial junction are compared in Figure 4.13.

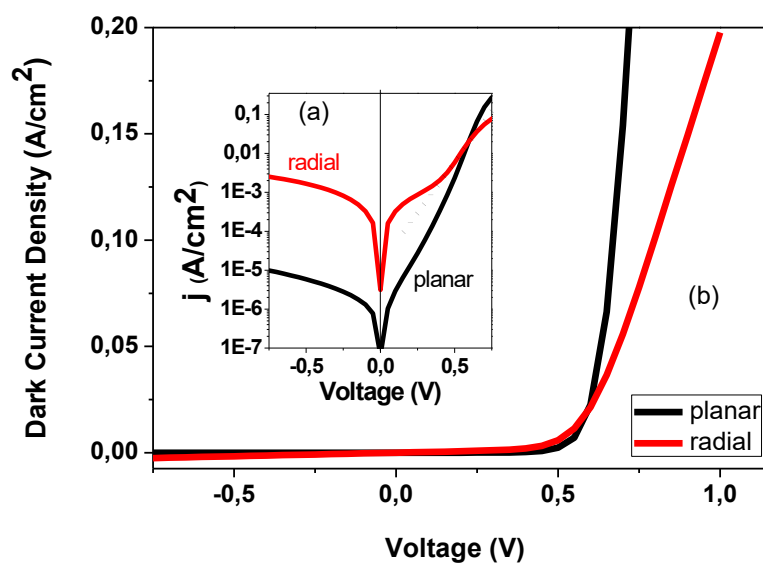


Figure 4.13. (a) Semilog, (b) Linear dark J-V characteristics of solar cells with planar and radial junction having 6,1  $\mu\text{m}$  micropillar length.

The ideality factors of the diodes were calculated as 1.7 and 3.2 for planar and radial junctions, indicating a lower quality junction in the radial junction devices. Moreover, the deviation from the ideality is seen to be larger at lower voltages, which is usually attributed to the enhanced recombination at the junction [96, 108]. Therefore, it can be generally concluded that the high surface area results in high recombination current at the junction which is not far from the surface of the micropillar. This is however not affecting the  $V_{oc}$  values very significantly.  $V_{oc}$  performance, device quality and the ideality factor can be improved by a proper passivation which can be a subject of a future study.

#### **4.4. Conclusion**

In this study, well-ordered micropillar arrays with different lengths were uniformly formed by photolithography and MAE techniques on the surface of p-type, single c-Si wafers. In photolithography step, a photomask which contains circular opaque structures with a diameter of 4  $\mu\text{m}$  in a period of 6  $\mu\text{m}$  was used to obtain radial junction solar cells, i.e. to have micropillars on the surface whose radius is greater than the junction depth of 0.4  $\mu\text{m}$ .

Effect of metal assisted etching time on micropillar length and effect of micropillar length on surface reflection were studied. It was observed that micropillar length increased linearly by etching time with a rate of 0.17  $\mu\text{m}/\text{min}$ . Reflection measurements revealed that increased micropillar length results in lower average reflectance. In addition, prior to anti-reflective coating, surfaces with micropillars have lower reflectance than planar surfaces. Depending on the pillar length, the reflectance can be obtained as low as that of pyramid textured surfaces. On the other hand, after ARC, the average reflection of the pyramid textured surface is always the lowest one as the  $\text{SiN}_x$  optimization is based on this structure. However, the reflection results obtained from samples with micropillars are in accordance with the literature values for similar surface structures.

In order to fabricate radial junction solar cells, standard  $\text{POCl}_3$  tube furnace doping,  $\text{SiO}_2$  passivation, PECVD  $\text{SiN}_x$  coating as ARC, screen printed metallization, co-firing of the contacts and edge isolation were followed. The samples which were etched from 10 to 50 min. were processed to fabricate radial junction solar cells since applying more than 50 minutes etching caused deterioration on the side walls and the tips of the micropillars due to slow lateral etching. Since optical reflection from solar cells surface decreased with increasing micropillar length, solar cell short circuit current ( $J_{sc}$ ) and efficiency ( $\eta$ ) increased. This was also supported by IQE results and as a result, the maximum efficiency value was obtained from the cell with 6.1  $\mu\text{m}$  long micropillars. The best solar cell efficiency is 15.9 % and this is one of the highest reported values obtained from the radial junction solar cells prepared by MAE technique.

Radial junction solar cells fabricated with nano/micropillars are expected to have efficiency values in the range of 15%-18% depending on pillar size and quality [161]. Although the efficiency value obtained in this study is consistent with the literature, it is still possible to achieve better efficiency values from radial junction solar cells with better passivation techniques that will reduce surface recombination.



## CHAPTER 5

### **GOLD IMPURITIES IN CRYSTALLINE SILICON: RADIAL JUNCTION SOLAR CELLS ON LOW QUALITY CRYSTALLINE SILICON WAFERS<sup>2</sup>**

*“Following the light of the sun, we left the Old World.”*

Christopher Columbus

#### **5.1. Introduction**

Purity is one of the most crucial property of electronic materials. If a material has 99.99% purity, it is generally considered to be pure material in many applications. However, if it is to be used in microelectronics and photovoltaic applications, a purity level of 99.99% is not sufficient as it corresponds to high contamination. This is because a trace amount of impurity can have a high impact on the electronic properties such as conductivity and carrier lifetime. On the other hand, although high efficiency is obtained from the devices produced with high-purity materials, the cost of the produced devices is also increased. For this reason, it is highly desirable to use low quality material to reduce costs.

The impurities of the crystalline silicon material can be divided into 2 categories; contaminants and dopants. The dopant atoms, i.e. boron, arsenic, phosphorous, are intentionally added to the material to adjust the resistivity of it to be used in fabricating

---

<sup>2</sup> The contents of this chapter have been submitted for publication. G. Baytemir, F. Es and R. Turan, (2018) “Comparison of Influence of Gold Impurities on the Performances of Planar and Radial Junction c-Si Solar Cells”

the devices. However, contaminant atoms occur during the production of the c-Si material, unintentionally. For the production of silicon, some carbon based agents are used and they are important sources of contaminants since they consist of different amounts of Ca, S, P and some metal impurities, such as, Au, Pt, Fe, Co, Ni, Cu [162].

The study (WH study) conducted by Westinghouse Corp [163] in the 1980s for the effect of impurities on the performance of solar cells is still used as a reference. However, since then, advances in cell processing enable to use low-cost materials in non-traditional cell structures, thereby achieving close efficiency values to the traditional ones. Therefore, there is a need for detailed studies.

In this thesis, solar cells were fabricated on c-Si contaminated with Au impurities. The purpose here is to show that radial junction solar cells can have an advantage on low purity materials. At the same time, conventional planar cells are produced on these low-quality materials to examine how impurities affect the performances of both cell types.

In this chapter, the role of metal impurities in Si material is discussed before going to cell production, and then the results of Au metallic contaminations on the performance values obtained from planar and radial junction cells are given.

## **5.2. Metal Impurities in Crystalline Silicon**

This section describes how metallic impurities affect the material properties. The metal impurities in the silicon wafers are present as foreign atoms in the crystalline structure of the silicon. These atoms may be point defects in the lattice structure by acting as substitutional or interstitials, as well as on the wafer surfaces. Since each element has its own unique property, such as atomic size, the distribution of impurities in the wafers depends on which type of atoms they are. More generally, the chemical status and distribution of impurity atoms depend on the solubility and diffusivity of those atoms. Impurity atoms are the cause of defect energy levels within the band gap

energy levels of silicon. This greatly affects the electronic properties of the devices fabricated from that silicon crystal due to increasing the possibility of recombination of the carriers.

### **5.2.1. Solubilities and Diffusivities of Metal Impurities**

The maximum dissolved impurity concentration in a material is defined as the solubility of the impurities when thermal equilibrium is achieved. The thermal equilibrium and thus solubilities of the impurities depend on the applied temperature. In addition, it is also dependent on the surface conditions of the material. [164]. High diffusivity causes impurities to move towards a higher solubility area, for instance to phosphorus-rich layer, or to regions where crystal defects occur. Since dissolved impurities behave as recombination centers by creating new energy levels within the band gap, it is preferable to collect the impurities into precipitates to decrease the recombination probability per atom and thereby to increase the minority carrier diffusion length.

### **5.2.2. Diffusion Mechanisms**

In metals, self diffusion takes place if there is no net mass transport, however, the impurity atoms carry out diffusions randomly along the crystal. Several atomic mechanisms have been suggested for self diffusion and inter-diffusion. The energetically favored mechanism involves replacing an atom with a neighboring vacancy: *substitutional diffusion*. The impurity atoms performing the *interstitial diffusion* mechanism diffuse by jumping from one interstitial site to neighboring one as they are small enough to capture the interstitial regions. In this diffusion, the number of interstitial sites that the atoms occupied is usually large, therefore the required energy is only for motion. Also, it is faster than the substitutional diffusion. Some elements can alternate between these two mechanisms. In semiconductors, elements are usually dissolved as substitutional, but then they can be moved by fast

diffusion in interstitial form [165-167]. Transition from interstitial sites to substitutional sites takes place in the presence of vacancies or self-interstitial atoms and defined as Frank-Turnbull mechanism [165-168]. Another reaction involving self-interstitials is defined as kick-out mechanism [169].

According to the results of studies on concentration profiles of Au, at temperatures of 800°C and above, it diffuses in silicon via on kick-out mechanism and has a U shape diffusion profile in silicon [170-173].

### **5.3. Experimental Procedures: Radial Junction Solar Cells on Low Quality Silicon Wafers**

As described in the previous section, it is known that gold diffuses in silicon very quickly as an interstitial atom and then is converted as substitutional impurity atom, which is very active electrically, by means of the kick-out mechanism. In many previous studies, it has been observed that Au has a U shape diffusion profile at temperatures between 700-1300 °C [174-177]. It was argued that the radial junction solar cells can have relatively good performance on materials with low quality, and this would reduce the fabrication cost. In this study, Au which has a fast diffusion mechanism in silicon was used to decrease the quality of the Si wafers since it diffuses across the entire surface. The effect of the gold impurities in silicon on bulk lifetime of wafers was examined systematically. Then using these Si wafers at low quality, planar and radial junction solar cells were fabricated and the effects on the solar cell performance were investigated. As a result, while the efficiencies of the cells in the planar junction formed from Si wafers containing Au contamination are reduced in high amounts, the solar cells in the radial structure are not much affected using these low-quality wafers.

In all steps of this work, for lifetime measurements and to fabricate solar cells, 275 µm thick, single side polished, boron doped monocrystalline silicon wafers with resistivity of 1-10 Ω • cm were used. In order to create metal contamination in the

wafers, at least 10 nm gold layers were thermally evaporated on the surface of the wafers and then these gold layers were diffused into the wafers at 800 °C for 1 hour under nitrogen atmosphere.

Before proceeding to solar cell fabrication, a lifetime study was carried out. In order to determine whether Au impurities have been introduced into the samples or not, 3 different samples were prepared. The PL lifetime measurements were taken, and the bulk lifetime of these samples were examined afterwards. The first one of these samples is the reference sample without any Au impurity and any thermal treatment. The second and third samples were subjected to Au contamination by diffusion. After Au diffusion, these samples were kept in aqua regia solution to remove the gold residues from the surfaces. The third one, unlike the second one, was later etched in a 20 % KOH solution at 80 °C temperature for 10 minutes, allowing 10 µm to be etched from both sides of the sample. In this way, it is understood that Au with a U-shaped diffusion profile in the silicon is sufficiently diffused in the middle regions of the samples or not. The prepared samples were deposited with 20 nm Al<sub>2</sub>O<sub>3</sub> with atomic layer deposition (ALD) method for surface passivation after applying RCA-1 and RCA-2 cleanings to remove organic and metallic contaminations. Finally, they were activated by annealing at 425 °C for 30 minutes under N<sub>2</sub> atmosphere. Photoluminescence (PL) lifetime measurements were performed to determine the bulk lifetime values after activation. Following bulk lifetime measurements, solar cell production whose steps are shown in the Figure 5.1 was carried out.

After removing the undiffused gold layer on the surface using the aqua regia solution, the samples were made ready for forming the radial geometry by performing RCA-1 and RCA-2 cleanings. The radial geometry was formed on both contaminated and uncontaminated samples. In order to define the distribution of the radial geometry and to obtain micropillar array pattern, photolithography and MAE methods were applied as in Chapter 3 and Chapter 4. Considering the efficiency results of the cells fabricated in the previous chapter, all radial geometry junction samples were subjected to 50 minutes of etching in this work. Because gold was used as a catalyst for MAE, it was

also removed from the surfaces using aqua regia solution after forming micropillars on the surfaces.

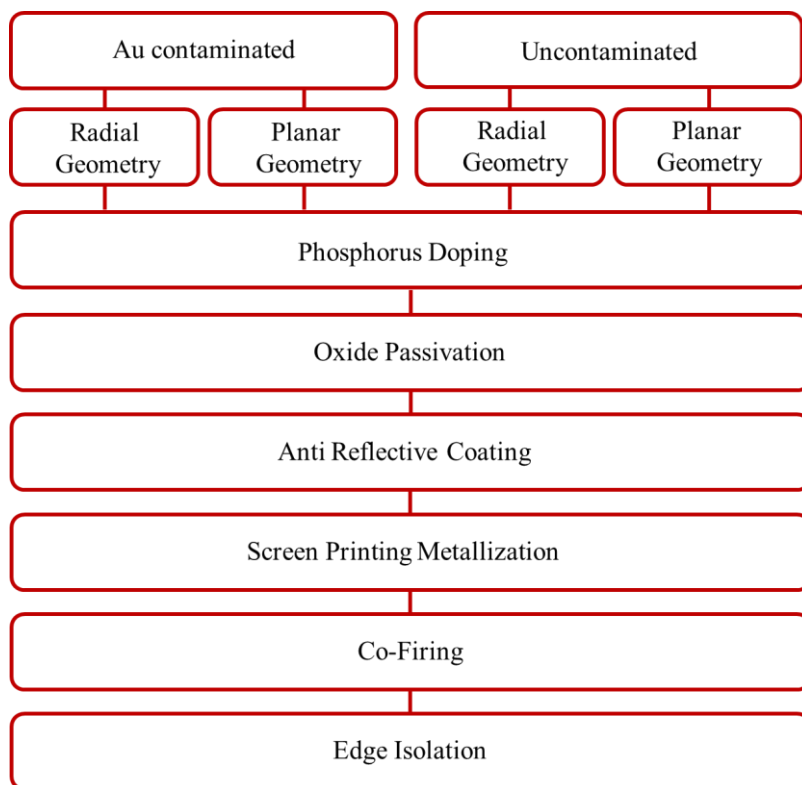


Figure 5.1. Process sequence for planar and radial junction solar cell productions on Au contaminated and uncontaminated Si wafers.

For the fabrication of solar cells, all samples, with and without gold contamination, micropillars being formed and planar, were immersed in HF: HCl solution to remove oxide deposits on the surface. Later, RCA-1 and RCA-2 were applied for organic and metallic cleanings, respectively and were then dipped again in HF: HCl solution to remove the oxide layer resulting from the cleaning procedures. Subsequently, as in the previous chapter, using  $\text{POCl}_3$  as the source gas at  $830^\circ\text{C}$  for 25 minutes in a SEMCO Engineering LYDOP furnace, the surfaces of the samples were coated with phosphosilicate glass (PSG) and phosphorous atoms diffused into the samples at 20

min. drive-in step by annealing. Thus, all the samples were doped with phosphorus and doping depth of about 500 nm and 50  $\Omega/\square$  sheet resistance at the samples were achieved. After removing PSG by HF solution and cleaning of the surfaces by RCA-2, the surfaces of the samples were passivated by 10 nm dry oxide formation, formed in the oxidation tube of the furnace at 830  $^{\circ}\text{C}$  temperature for 30 min. As an antireflection coating layer, around 75 nm of  $\text{SiN}_x\text{:H}$  was deposited on the front sides by PECVD at 380  $^{\circ}\text{C}$ . For the contact formation, Ag busbar and fingers to the front sides and full Al layer to the rear sides were formed by screen printing metallization method. Since the optimum firing characteristics of the samples in this study were unknown to obtain high efficiencies, firing processes at  $\sim 900$   $^{\circ}\text{C}$  but at different speeds were applied. For the characterization of the samples, the methods used in the previous chapter were applied.

#### **5.4. Results and Discussion**

The carrier lifetime distribution obtained from the PL lifetime mappings are shown in Figure 5.2. Furthermore, the lifetime values of the samples were also measured by Sinton Lifetime Tester. For a minority carrier density (MCD) of  $10^{15} \text{ cm}^{-3}$ , the lifetime of the reference sample without any contamination and heat treatment (in accordance with Figure 5.2-a) exhibited around 119  $\mu\text{sec}$ , while the lifetime of the Au contaminated samples without and with surface etching were measured to be 4.93  $\mu\text{sec}$  and 8.15  $\mu\text{sec}$  by Sinton Lifetime Tester, respectively, in accordance with Figure 5.2-b and Figure 5.2-c.

As expected, the lifetime was severely reduced relative to the reference sample having no Au contamination. Although a slight increase was observed in lifetime of sample etched from the both sides, the lifetime was observed to be still very low compared to the reference samples in both etched and unetched samples, indicating that Si wafer is fully contaminated by Au.

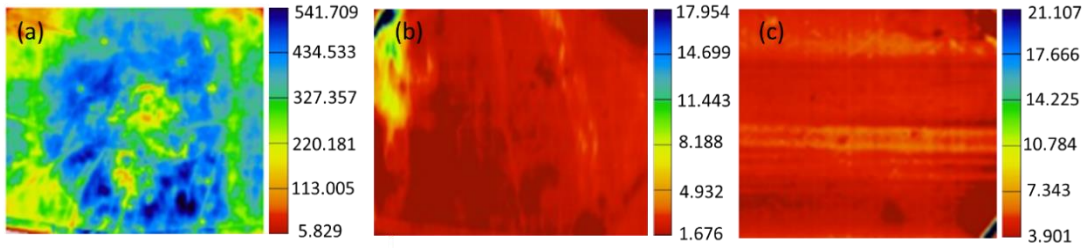


Figure 5.2. Photoluminescence lifetime mapping and after 20 nm Al<sub>2</sub>O<sub>3</sub> deposition and activation. (a) reference sample, (b) 10 nm Au coated and diffused at 800C for 1 h (c) 10 nm Au coated, diffused at 800C for 1 h and 10 μm etched from both sides.

After standard solar cell process steps, different firing speeds were applied during the formation of solar cells. Appropriate co-firing parameters must be applied to obtain the Al back surface field (BSF) formation and to allow the front silver fingers and busbars to dig into the nitrate layer without damaging the junction. Since the properties of firing vary according to the sample thicknesses and the thicknesses of the wafers used here were 275 μm, thicker than standard solar wafers, slower firing belt speeds had to be applied. For this reason, all samples were fired at speed of 250 to 500 cm/min.

Electrical characterization of the solar cells was provided by ENDEAS Quicksun solar simulator at room temperature. Metal shadowings only due to silver busbars were subtracted to calculate active solar cell efficiencies. Performance parameters as a function of firing belt speed as shown in Figure 5.3 and Table 5.1. While the planar solar cells had their best results at a range of 325-375 cm/min, the best results for the radial junction solar cells were obtained at 400-450 cm/min. firing belt speeds. The reason for the cells in the radial structure to have best results at faster firing speeds is that the samples became somewhat thinner during MAE. At the firing speeds outside of those ranges, all the cells suffered from a low fill factor. For this reason, the results were evaluated for both cell types based on their own firing belt speed intervals.



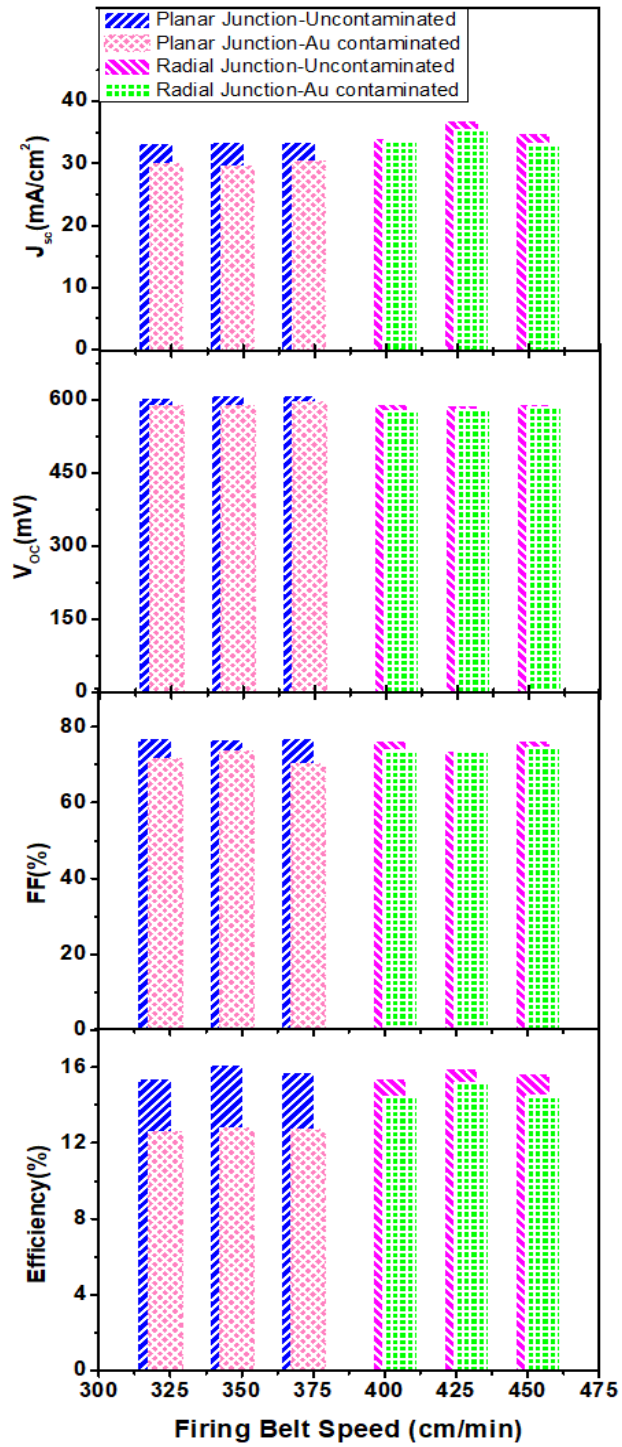


Figure 5.3. Performance parameters of Au contaminated and uncontaminated planar and radial junction solar cells as a function of firing belt speed.

Table 5.1. Performance parameters of Au contaminated and uncontaminated planar and radial junction solar cells as a function of firing belt speed.

| Junction Type-Substrate | Firing Belt Speed (cm/min) | $J_{sc}$ (mA/cm <sup>2</sup> ) | $V_{oc}$ (mV) | FF (%) | Efficiency (%) |
|-------------------------|----------------------------|--------------------------------|---------------|--------|----------------|
| PJ-Uncontaminated       | 325                        | 33.26                          | 603           | 76.81  | 15.38          |
|                         | 350                        | 34.44                          | 610           | 76.73  | 16.13          |
|                         | 375                        | 33.46                          | 610           | 76.96  | 15.70          |
| PJ-Au contaminated      | 325                        | 30.00                          | 587           | 71.50  | 12.59          |
|                         | 350                        | 29.60                          | 588           | 73.62  | 12.81          |
|                         | 375                        | 30.30                          | 597           | 70.42  | 12.74          |
| RJ-Uncontaminated       | 400                        | 34.04                          | 592           | 76.42  | 15.40          |
|                         | 425                        | 36.83                          | 587           | 73.54  | 15.90          |
|                         | 450                        | 34.79                          | 591           | 76.18  | 15.67          |
| RJ-Au contaminated      | 400                        | 33.76                          | 579           | 73.82  | 14.46          |
|                         | 425                        | 35.49                          | 580           | 73.82  | 15.20          |
|                         | 450                        | 33.18                          | 586           | 74.59  | 14.51          |

According to the results of the short circuit current density ( $J_{sc}$ ), as a result of carrier collection, it was observed that in the samples without contamination, the radial geometry cells have somewhat higher values than the values of planar geometry cells, while it was observed that this difference obviously increases in cells containing gold contamination. Since open circuit voltage ( $V_{oc}$ ) is a measure of the amount of recombination, radial junction cells, both with and without Au contamination, have lower  $V_{oc}$  values due to high surface area. It can be improved with better surface passivation techniques. However, even after Au contamination, less decrement in  $V_{oc}$  was observed, compared to the planar structure cells. The decrease in the fill factor (FF) is another parameter that plays a role in further reducing the performance of solar cells. As seen in the same figure and table, the FFs of the cells were significantly reduced in contaminated cells. As in the  $V_{oc}$  and  $J_{sc}$  results, it was observed that FFs

were less affected in radial junction solar cells. As a consequence of all these performance parameters, the efficiency values of the solar cells showed that radial junction solar cells were less affected from Au impurities.

*Table 5.2. The average of the performance parameters of Au contaminated and uncontaminated planar and radial junction solar cells.*

| Junction Type-Substrate | $J_{sc}$<br>(mA/cm <sup>2</sup> ) | $V_{oc}$<br>(mV) | FF<br>(%) | Efficiency<br>(%) |
|-------------------------|-----------------------------------|------------------|-----------|-------------------|
| PJ-Uncontaminated       | 33.72±0.7                         | 608±7            | 76.83±0.1 | 15.74±0.4         |
| PJ-Au contaminated      | 29.97±0.4                         | 591±6            | 71.85±1.8 | 12.72±0.1         |
| RJ-Uncontaminated       | 35.22±1.6                         | 590±3            | 75.38±1.8 | 15.66±0.2         |
| RJ-Au contaminated      | 34.14±1.3                         | 581±5            | 74.08±0.5 | 14.71±0.5         |

The average performance parameters of the three different cells for all types and their average J-V curves are given in Table 5.2 and Figure 5.4. The same interpretations could be mentioned according to their averages.

According to the literature, radial junction solar cells consist of nano/micropillars are expected to give efficiency values in the range of 15%-18% depending on pillar geometry [161]. In addition, it is possible to obtain energy conversion efficiencies up to 16% even with low purity silicon [89].

In this study, we have shown that energy conversion efficiencies from the planar and radial geometries, which consist of samples with the same feature and have the same process steps, are close to each other, (on average) 15.74% and 15.66%, respectively. However, from planar and radial cells formed from intentionally contaminated samples, on average 12.72% and 14.71% efficiencies were observed. This corresponds to a relative decrease of 6.07 % in the efficiency of radial junction and 19.19 % in the

planar junction. This is in agreement with the expectation that radial junction solar cells are less sensitive to the quality of the wafer used.

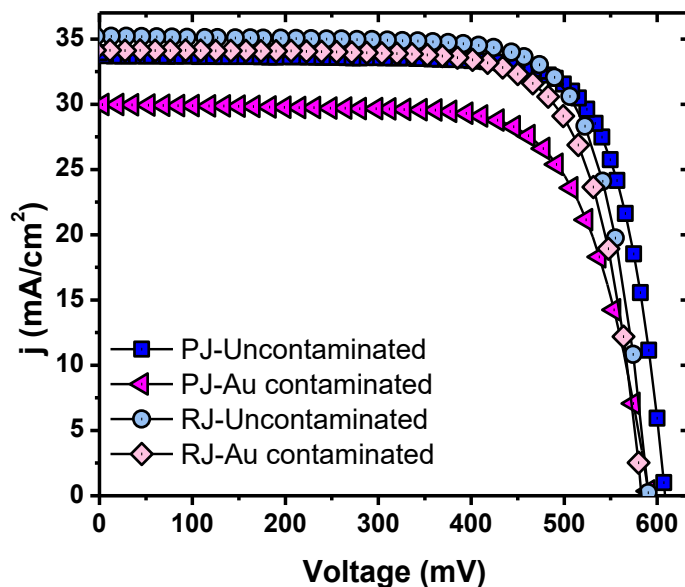


Figure 5.4. Circuit current density vs. voltage graph obtained from the averages of the parameters of Au contaminated and uncontaminated planar and radial junction solar cells.

In order to understand the degradation mechanisms and their causes, the internal quantum efficiencies of the solar cells shown in Figure 5.5 were calculated from their external quantum efficiencies EQE and reflection measurements as a function of wavelength. At low wavelengths, IQE provides information about emitter recombination because of the shallow absorption of these photons in silicon. On the other hand, high-wavelength photons are absorbed deeper in silicon wafers, so high-wavelength IQE results provide information on minority carrier diffusion length depending on passivation and back surface conditions. In this study, the change in IQE values in high wavelengths depends on the variation in direct bulk recombination, since a change in the back surface of the samples is not examined and it is assumed that Au contamination does not affect the back surface properties.

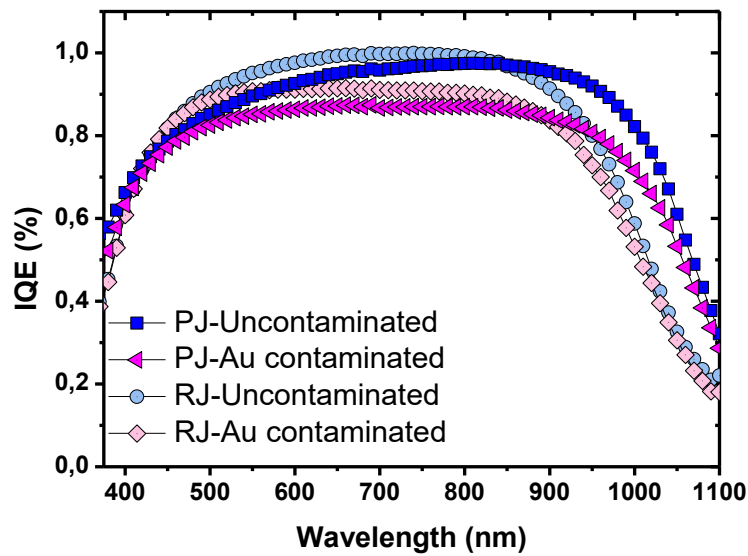


Figure 5.5. Averages of Internal Quantum Efficiencies of Au contaminated and uncontaminated Planar and Radial Junction Solar Cells as a function of wavelength

Solar cells in both type of geometries, in the emitter region gave high IQE values. On the other hand, degradation of IQE curves of the cells containing Au contamination at high wavelengths are due to bulk recombinations. In both types of geometry, Au contamination caused a visible decrease in IQE values at high wavelength region. However, as in the performance parameters, in IQE results, it was observed that RCSCs were less affected by this contamination.

### 5.5. Conclusion

In this study, it was shown that solar cells with three-dimensional radial junction are less affected by the use of low-quality materials than those with planar junction cells. This is because, as an advantage of the geometry of the radial junction, minority carriers in these cells need to travel a shorter distance to reach the junction region.

To illustrate this, the wafers to be used for solar cell fabrication were intentionally contaminated with metal impurities. In order to create metal contamination in the wafers, at least 10 nm gold layers were thermally evaporated on the surface of the wafers and then the gold layers on the surface of the wafers were diffused into the wafers at 800 °C for 1 hour under nitrogen atmosphere. They were contaminated by Au, which is used in many studies and shown to have a U-shaped diffusion profile. Before proceeding to solar cell fabrication, a lifetime study was carried out. According to the results of PL lifetime mapping and Sinton lifetime tester, the lifetime was severely reduced relative to the reference sample having no Au contamination, indicating fully contamination of Au.

For comparison purposes, the planar and radial junction cells were also fabricated using high quality materials. In the fabrication of radial junction solar cells, well-ordered single crystalline micropillar arrays were formed by MAE through photolithography, as explained in Chapter 3 and Chapter 4. Subsequently, standard cell formation procedures after surface cleaning were applied to all the samples. Since the optimum firing characteristics of the samples were unknown, various belt speeds were applied for co- firing process.

As a result, the efficiency from samples with the planar and radial geometries and having no contamination are close to each other, with their average efficiency values of 15.74 % and 15.66 %, respectively. On the other hand, in the case of metallic contamination, the efficiency of the cells with radial junction degraded much less compared to the planar junction with the values of 14.71 % and 12.72 %, respectively. This is in agreement with the expectation that cells with a radial geometry are less sensitive to the quality of the material used. In addition, these results show that future structural optimizations providing optical gain as well as electrical gain enable the usage of materials with low lifetime and thus lower fabrication costs without reducing the solar cell performance.

## CHAPTER 6

### RADIAL JUNCTION SOLAR CELLS ON THIN CRYSTALLINE SILICON WAFERS

*“Solar power is the last energy resource that isn't owned yet - nobody taxes the sun yet.”*

Bonnie Raitt

#### 6.1. Introduction

##### 6.1.1. Towards Radial Junction, Thin c-Si Solar Cells

It is predicted that silicon will continue to be used in a foreseeable future due to its natural abundancy together with high efficiency properties in photovoltaic cells and the fact that it has been studied for many years and is a well-known material. However, in the fabrication of solar cells, efforts are made to reduce the cost of fabrication with high efficiency efforts. In addition, it is tried to be manufactured in a flexible structure to be installed on the materials used for daily necessities. In recent years, perovskite [177], organic [178], dye sensitive solar cells [179] have been the subject of many studies due to their flexible structures and low costs. However, despite all these studies, the efficiency values obtained from these cells are very low compared to the efficiencies obtained from silicon solar cells. Therefore, it is necessary to reduce the thickness of the silicon amount used in Si solar cells in order to utilize the excellent properties of the silicon, and to reduce the fabrication cost.

Thin Si solar cell production reduces costs by not only because of less material consumption, but also by allowing the usage of low-quality Si materials with short carrier diffusion length. Thin Si solar cells are attractive because they allow high open circuit voltage in the cell by reducing recombination possibility. However, Si has a low absorption coefficient as it is a semiconductor with indirect band gap.

Planar solar cell fabricated from thin silicon wafers have absorption losses in the near infrared region due to the low absorption coefficient and have a surface reflection of more than 30%, resulting in decrease in the efficiency. Therefore, in order to prevent efficiency losses, light harvesting strategies such as the application of surface texturing, forming nano or micro structures on the surface should be applied. Although nanostructures are promising in terms of light absorption, solar cells containing nanostructures have a large surface area, and they are fully doped after the doping process. Therefore, they exhibit low efficiency in the short wavelength region of the spectrum due to Auger recombination. In contrast to nanostructured cells, the cells containing micropillars on the surfaces, i.e. three-dimensional junction solar cells, are more suitable for thin solar cells, since they have both light trapping and carrier collection properties, as schematized in Figure 6.1.

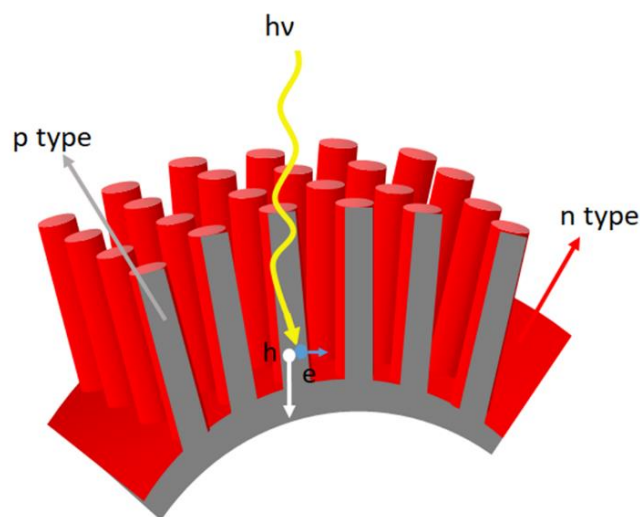


Figure 6.1. Schematic of radial junction solar cell with thin, flexible substrate.



### 6.1.2. Si Wafer Thinning

Si wafer thinning is an important process for MEMS applications. It can be used to thin the wafer itself, to remove the irregular structures from the surface or to polish the surface of the Si wafers. There are four main techniques for wafer thinning: mechanical grinding, Chemical Mechanical Planarization (CMP), Atmospheric Downstream Plasma (ADP) Dry Chemical Etching (DCE) and wet etching [180]. In the mechanical grinding and CMP, in order to thin the wafer, a wheel and water or chemical slurries are used and combined for the reaction with the wafer. In dry or wet etchings, chemicals are used to thin the wafer.

In this work, wet etching was used to thin the wafers, since it is a simple, fast and cost-effective technique and it works properly. In wet etching method, usually a mask is used to protect undesired region from thinning. While some chemicals are isotropic etchants like HNA, the combination of HF, HNO<sub>3</sub> and acetic acid (CH<sub>3</sub>COOH), the others are anisotropic like KOH, tetramethylammonium hydroxide, (TMAH) ethylenediamine pyrocatechol (EDP).

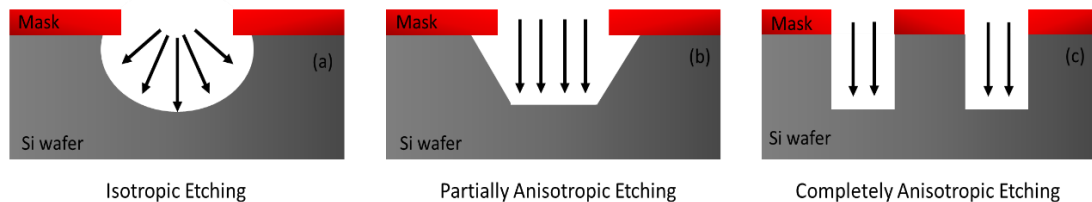


Figure 6.2. (a) Isotropic, (b) Partially Anisotropic, (c) Completely Anisotropic etchings.

In isotropic etching (uniform in all directions), the etching rate is similar in all the directions. Therefore, the wafer is removed laterally at the similar rate of etching downward. On the other hand, in anisotropic etching (uniform in one direction), etching rates are different for different crystallographic orientation. The working

principles of these two types of chemical etchings are shown Figure 6.2. In this study, Si wafers were thinned by KOH.

## 6.2. Experimental Procedures

In this work, 275  $\mu\text{m}$  thick, double side polished, boron doped monocrystalline silicon wafers with a resistivity of 1-10  $\Omega \cdot \text{cm}$  were used. During the entire thesis work, the photolithography on the polished wafers was applied before MAE processes as described in Chapter 3. During the photolithography process, the samples should be hard contacted with the photomask. Therefore, the micropillar arrays were formed first, and then the thinning was performed from the back sides. Firstly, for radial junction cells, it has been tried to obtain samples with as long micropillars as possible and to increase the ratio to flat region as much as possible since the aim here is to investigate how radial junction and planar junction solar cells would be affected when they are fabricated on thin substrates. According to the results of Chapter 4, the lengths of micropillars increase with metal assisted etching time. However, for long periods of etching, i.e. more than 50 minutes, with the solution of  $[\text{HF}] = 1.8 \text{ M}$ ,  $[\text{H}_2\text{O}_2] = 0.4 \text{ M}$ ,  $\text{H}_2\text{O}$  the side walls and tips of the micropillars began to deteriorate due to slow lateral etching. Therefore, in order to control lateral etching, higher HF concentration was applied. Moreover, to obtain more vertical and smooth etching, the etchant solution with low surface tension was used. The etchant solution  $[\text{HF}] = 5.4 \text{ M}$ ,  $[\text{H}_2\text{O}_2] = 0.4 \text{ M}$ , Ethanol was used and to etch the tips of the micropillars, a KOH study was performed.

After obtaining smooth micropillars, a new solar cell optimization study was performed to decide the length of the pillars for high performance solar cells. As described in the previous chapters, standard solar cell processes were applied.

After deciding optimum micropillar length and sample preparation, 50 wt. % KOH etching at 80-90<sup>0</sup> C was performed to fabricate planar and radial junction Si solar cells with various thicknesses. However, since KOH would also etch the micropillars and

disrupt the radial structure, the front sides of the samples with micropillars were protected with SiN<sub>x</sub> and then the etching was performed using a single side hole teflon holder. The planar samples were etched from both sides without using holder.

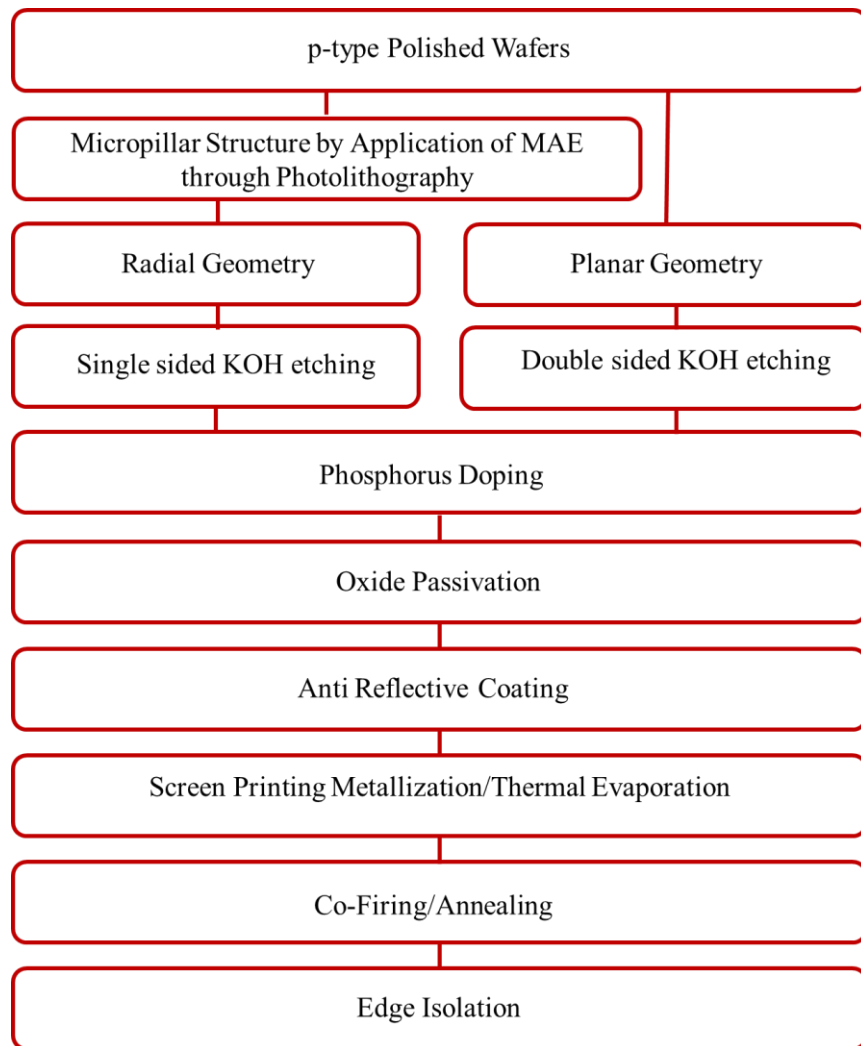


Figure 6.3. Process sequence for planar and radial junction solar cell productions at various thicknesses.

After removing SiN<sub>x</sub> layer from the surfaces of the radial junction solar cell samples by high concentration of HF solution and after removing metallic and organic

contaminations from all the samples' the surfaces, standard solar cell processes were applied as described in previous chapters. However, some of the thin cells suffered from contact formation. Therefore, Al thermal evaporation and annealing at 800 °C for 40 min. was applied for the back sides of the cells. For the front sides, it was necessary to apply photolithography to open finger/busbar areas for the applicability of Ag thermal evaporation. Since it is a troublesome process for thin samples, screen printing metallization was applied for the front sides and for co-firing, belt speed optimization was performed with respect to cell thicknesses. The solar cell fabrication process steps are shown in Figure 6.3.

### **6.3. Results and Discussion**

The aim of this study is to show that for thin solar cells, radial junction with micropillars on the surfaces has an advantage over planar junction. For this purpose, for the radial junction cells, firstly it was tried to prepare samples with as long micropillars as possible compared to the underlying planar region. However, as explained before, in the MAE etching mechanism, the extracted holes diffuse to areas covered by noble metals, but they can also diffuse into the other areas which are not covered by metal, if they are not depleted at the metal-semiconductor interface. Even the rate of etching in the lateral direction is slower than in the vertical direction, surface roughness can be observed outside of the intended region for long etching durations [157, 158]. According to the results of Chapter 4, understood from Figure 4.5, for long periods of etching, i.e. more than 50 minutes, the sidewalls and tips of the micropillars began to deteriorate due to slow lateral etching. Since it is not possible to apply more than 50 min. etching with the solution of  $[HF] = 1.8 \text{ M}$ ,  $[H_2O_2] = 0.4 \text{ M}$ ,  $H_2O$ , it was decided to use a different etchant solution to obtain deeper and smooth micropillars.

In order to reduce pores effect and improve etching result, the solution with the same HF and H<sub>2</sub>O<sub>2</sub> concentrations was prepared but ethanol was used instead of H<sub>2</sub>O. SEM results of the samples etched in these two different solutions is given in Figure 6.4.

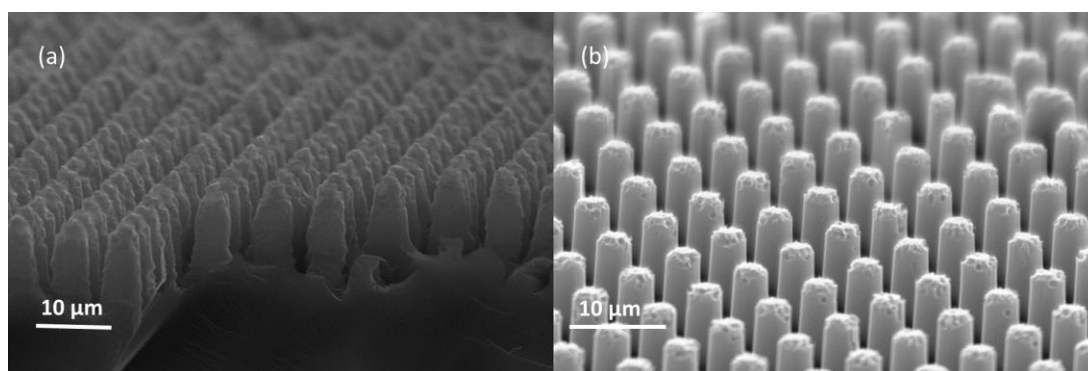


*Figure 6.4. The cross-sectional SEM images of the etched samples with  $[HF] = 1.8, M [H_2O_2] = 0.4 M$ , (a) H<sub>2</sub>O (b) Ethanol; the etching duration was 60 min.*

As seen in the figure, the etching result was improved using etchant solution containing ethanol which has a low surface tension. The possible reason of this etching result could be that ethanol containing solution influenced the diffusion and solubility of HF and H<sub>2</sub>O<sub>2</sub>, resulting in a smoother etching. However, even though etching was improved, there were still pores on the tips of the pillars and lateral etching was also observed because of the extra holes which were not depleted at the metal-semiconductor interface and oxidize the sidewalls of the micropillars due to the difficulty of HF transport. Since this would be more problematic for longer etching durations, the HF concentration was increased in order to avoid lateral etching and pores on the tips.

The assumption is consistent with the results seen in Figure 6.5. Even though the pores were still observed on the tips of the micropillars after using the solution of  $[HF] = 5.4 M$ ,  $[H_2O_2] = 0.4 M$ , Ethanol, smoother etching was observed by increasing the HF concentration.

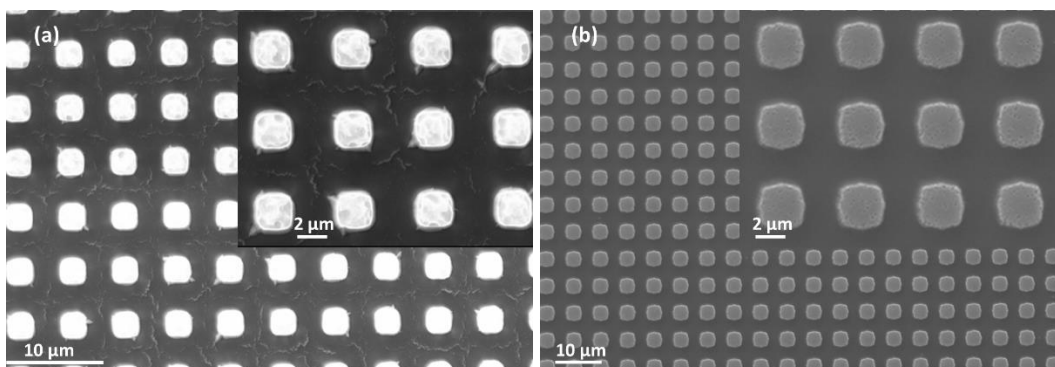


Figure 6.5. Low-magnification and higher-magnification (insets) SEM images of the etched samples with  $H_2O$ - $[H_2O_2] = 0.4 M$  and (a)  $[HF] = 1.8 M$ , and (b)  $[HF] = 5.4 M$ ; the etch duration was 60 min.

Thereafter, to ensure that there is no lateral etching for long durations, 300 min. of MAE with the etchant solution  $[HF] = 5.4 M$ ,  $[H_2O_2] = 0.4 M$ , Ethanol, and then to avoid pores on the tips of the micropillars, 1% KOH etching at 75-80 °C was applied to the samples for 1, 5, 10, 20, 30 seconds.

Although MAE process was performed for so long, no lateral etching was observed (Figure 6.6-a). From this point, it can be said that the solution used is suitable for long etching processes which is required to obtain long length micropillars.

As it is understood from Figure 6.6- a and b, no significant change was observed for 1 sec KOH etching. For 5- and 10-seconds etchings, (Figure 6.6-c and d) the tips of the micropillars were smoother. However, the tips of the micropillars were thinned. More than this, for 20 and 30 seconds etching, (Figure 6.6-e and f) and the bottoms of the pillars were also thinned and they would have a smaller diameters than the junction depth while fabricating solar cells. Since, 3-D junction solar cell property will not be achieved, it was decided not to apply KOH etching after forming micropillars.

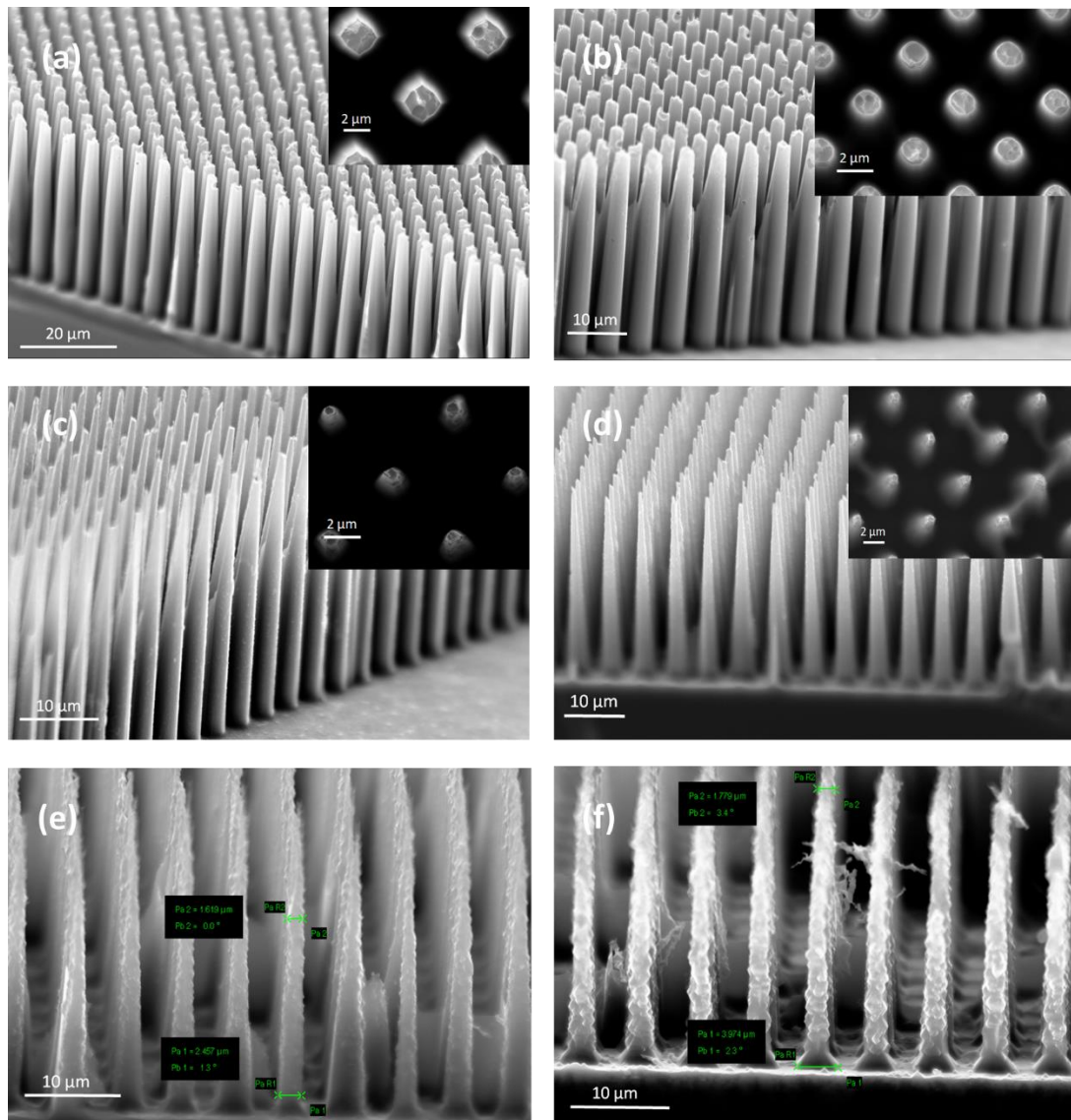


Figure 6.6. Low-magnification and higher-magnification (insets) SEM images of the samples after the application of 1% KOH etching at 75-80 °C for, (a) 0, (b) 1, (c) 5, (d) 10, (e) 20, (f) 30 seconds following MAE with  $[HF] = 5.4 M$   $[H_2O_2] = 0.4 M$ , Ethanol solution; the etching duration was 300 min.

After understanding that the solution is suitable for obtaining deep and smooth structures, standard cell processes were performed before going to the fabrication of thin solar cells. The aim was to observe the applicability of doping, passivation and metallization processes with the increase in junction area. Therefore, firstly the

samples were metal assisted etched for 60, 180, 300, 720, 1200 minutes and the length of the micropillars are 3.8, 11.5, 20.0, 47.1, 64.9  $\mu\text{m}$ , respectively. The cross-sectional SEM images of the samples are shown in Figure 6.7.

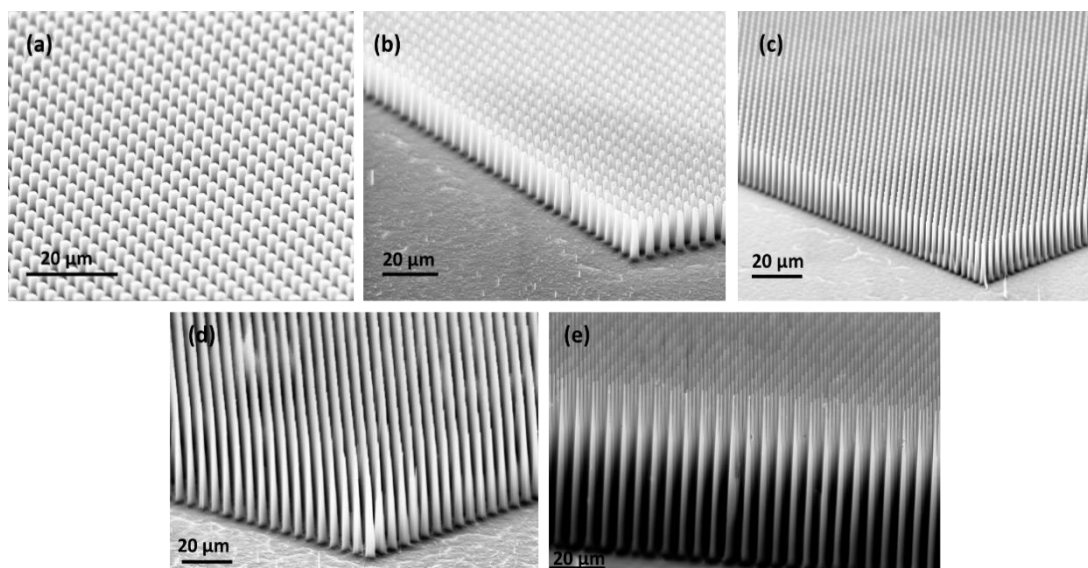


Figure 6.7. The cross-sectional SEM images of the samples etched for (a) 60, (b) 180, (c) 300, (d) 720, (e) 1200 minutes with  $[\text{HF}] = 5.4 \text{ M}$   $[\text{H}_2\text{O}_2] = 0.4 \text{ M}$ , Ethanol solution.

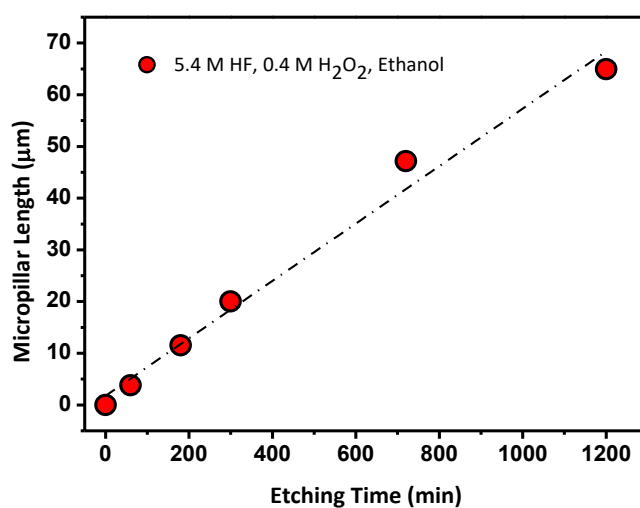


Figure 6.8. Micropillar length with respect to duration of MAE by  $[\text{HF}] = 5.4 \text{ M}$ ,  $[\text{H}_2\text{O}_2] = 0.4 \text{ M}$ , Ethanol solution.



The dependence of the length of the micropillars on the duration of the etching by  $[HF] = 5.4 \text{ M}$ ,  $[H_2O_2] = 0.4 \text{ M}$ , Ethanol solution is shown in Figure 6.8. The length of the micropillars increases linearly with the etching time and the etching rate was calculated as  $0.056 \mu\text{m}/\text{min}$ .

After removing Au layer from the surface, and applying necessary surface cleaning procedures, standard solar cell processes were applied. A.M. 1.5 G weighted reflectance characteristic of the surfaces with various micropillar lengths, after SiNx deposition is graphed in Figure 6.9. For comparison, weighted reflectance results of pyramid textured, and planar surfaces are also given. As expected, micropillars showed lower  $R_w$  than planar geometry and  $R_w$  decreased with increasing micropillar length as in Chapter 4. On the other hand, the average reflectance from the micropillar surface remains to be higher than the pyramid-textured surface coated with ARC. However, the sample having around  $65 \mu\text{m}$  length micropillars has a very similar reflectance result to pyramid textured surface,  $\sim 3\%$ . This is very promising that with a further optimization, lower reflectance results can be achieved with micropillar decorated surfaces.

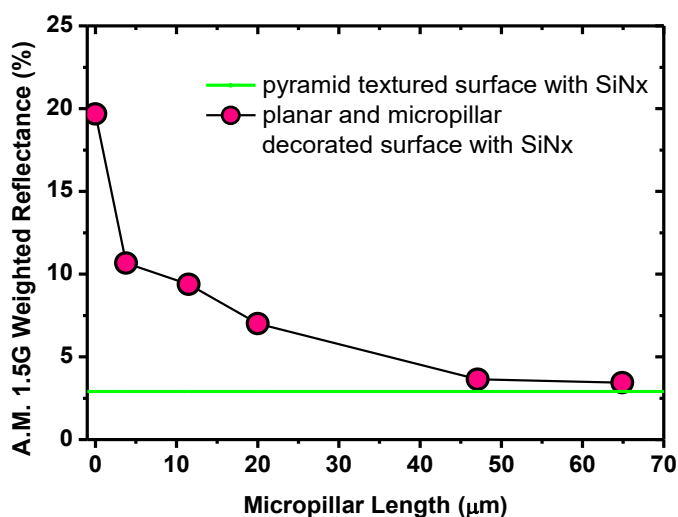


Figure 6.9. Weighted reflectance for each micropillar length after ARC. The length zero is for planar samples. Reflectance results of pyramid textured sample was inserted as reference line.

The J-V characteristics of the radial junction solar cells fabricated with the new micropillar lengths are graphed in Figure 6.10 and corresponding performance values are tabulated in Table 6.1. The average of performance values of planar solar cell is also given. In Chapter 4, it was concluded that the performance of radial junction solar cells increases with increasing micropillar length, which is in correlation with their average reflection values.

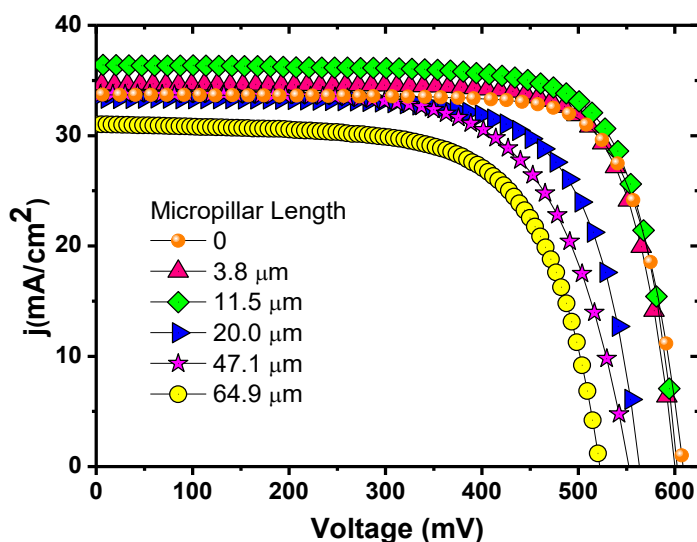


Figure 6.10. Current Density vs Voltage curves of the radial junction solar cells with different micropillars length. The J-V curve of planar junction solar cell is also given as comparison.

In this study, with the new etchant solution, longer micropillar lengths were obtained and it was also observed that the average reflection values decrease with increasing pillar length.  $J_{SC}$  results increased up to 11.5  $\mu\text{m}$  pillar length and similar  $V_{OC}$  results were obtained from the cells with 3.8 and 11.5  $\mu\text{m}$  micropillars. However, the parameters were not improved for longer micropillar lengths. The highest  $V_{OC}$  value was obtained from planar junction solar cell. The probable cause of that, the passivation becomes difficult for the cells which have longer micropillars.

*Table 6.1. Performance parameters of the radial junction solar cells with different micropillars length. The averages of the performance values of the planar solar cell are given as a comparison.*

| Micropillar length ( $\mu\text{m}$ ) | Efficiency (%) | $V_{\text{OC}}$ (V) | $J_{\text{SC}}$ ( $\text{mA}/\text{cm}^2$ ) | FF (%) |
|--------------------------------------|----------------|---------------------|---|--------|
| 0                                    | 15.74          | 0.608               | 33.72                                       | 76.83  |
| 3.8                                  | 15.88          | 0.600               | 34.66                                       | 76.38  |
| 11.5                                 | 17.27          | 0.602               | 36.41                                       | 75.59  |
| 20.0                                 | 13.40          | 0.563               | 33.40                                       | 71.24  |
| 47.1                                 | 12.34          | 0.552               | 33.76                                       | 66.20  |
| 64.9                                 | 10.85          | 0.521               | 31.04                                       | 67.13  |

In addition, although it is reasonably expected to increase the carrier collection with the increasing micropillar length, any increment was not observed in  $J_{\text{SC}}$  results after 11.5  $\mu\text{m}$  pillar length. Moreover, the FF values began to decrease with the increase in length. Therefore, the process steps applied for long micropillar cells should be developed. As a result of the standard processes performed, the highest performance values were obtained from the cell containing 11.5  $\mu\text{m}$  micropillars and the highest efficiency is 17.23%.

Figure 6.11 shows the EQE spectra of radial junction solar cells with various micropillar lengths. According to EQE results, at the short wavelength region, the cells with longer micropillars were remarkably improved. It can be concluded that three-dimensional junction was provided considering the junction depth, i.e. 400 nm. The generated minority carriers were able to be separated and collected since the length of the carriers required to reach the junction was shortened. Also, the absorption of the lights at short wavelengths was enhanced with the increment of the pillar length.

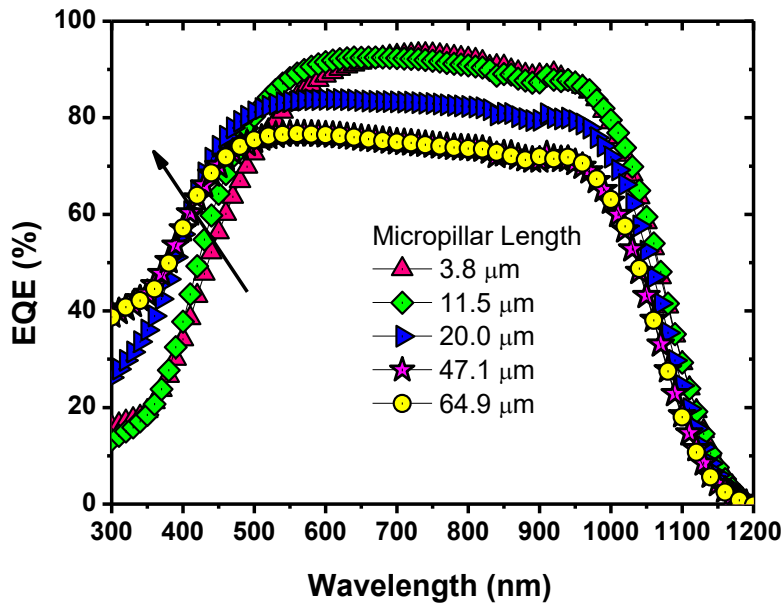


Figure 6.11. External Quantum Efficiency Spectra of Radial Junction Solar Cell with various micropillars length.

In order to clarify the enhancement of EQE at the short-wavelength region, IQE spectra was calculated from reflectance and EQE spectra. The results are shown in Figure 6.12. According to IQE results, reflectance effects are not included, at short wavelength region, all the samples with different micropillar lengths have similar values. Therefore, it can be concluded that the reason why EQE results in this region is increased with the length of the micropillars is due to the decrease in the reflection results as the length of the pillars increases. Hence, with the standard solar cell processes, the collection of the carriers could not be increased with micropillar length. On the other hand, at long wavelength region, the IQE results decreased obviously with the micropillar length. This is due to a thinner planar area with the increase in the pillar length. Therefore, light absorption at high wavelength region is reduced. This explains why the solar cell performance decreases as the length of the pillar increases.

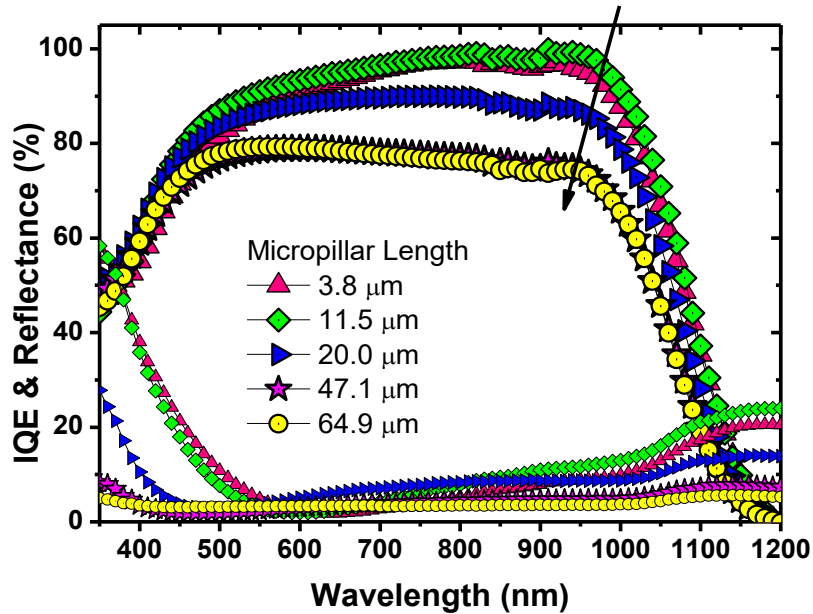


Figure 6.12. Internal Quantum Efficiency and Reflectance Spectra of Radial Junction Solar Cell with various micropillars length.

Considering all these results with the J-V results together, it was decided to fabricate thin solar cells using the samples with an average of 11.5  $\mu\text{m}$  micropillar length from which the highest performance values were obtained.

The SEM images of the solar cells with various thicknesses after the application of 50 wt. % KOH etching at 80-90<sup>0</sup> C and the standard solar cell fabrication processes are shown in Figure 6.13. As shown in Figure 6.13- a, b, c, after KOH etching for 1 hour 170-180  $\mu\text{m}$ , for 2 hours 90-100  $\mu\text{m}$  and for 3 hours 15-30  $\mu\text{m}$  thick samples were obtained. In Figure 6.13- e and f, an SEM image and a picture of 1.5 h double sided etched  $\sim$ 18  $\mu\text{m}$  planar solar cell are seen. The thinnest solar cells had flexibility property.

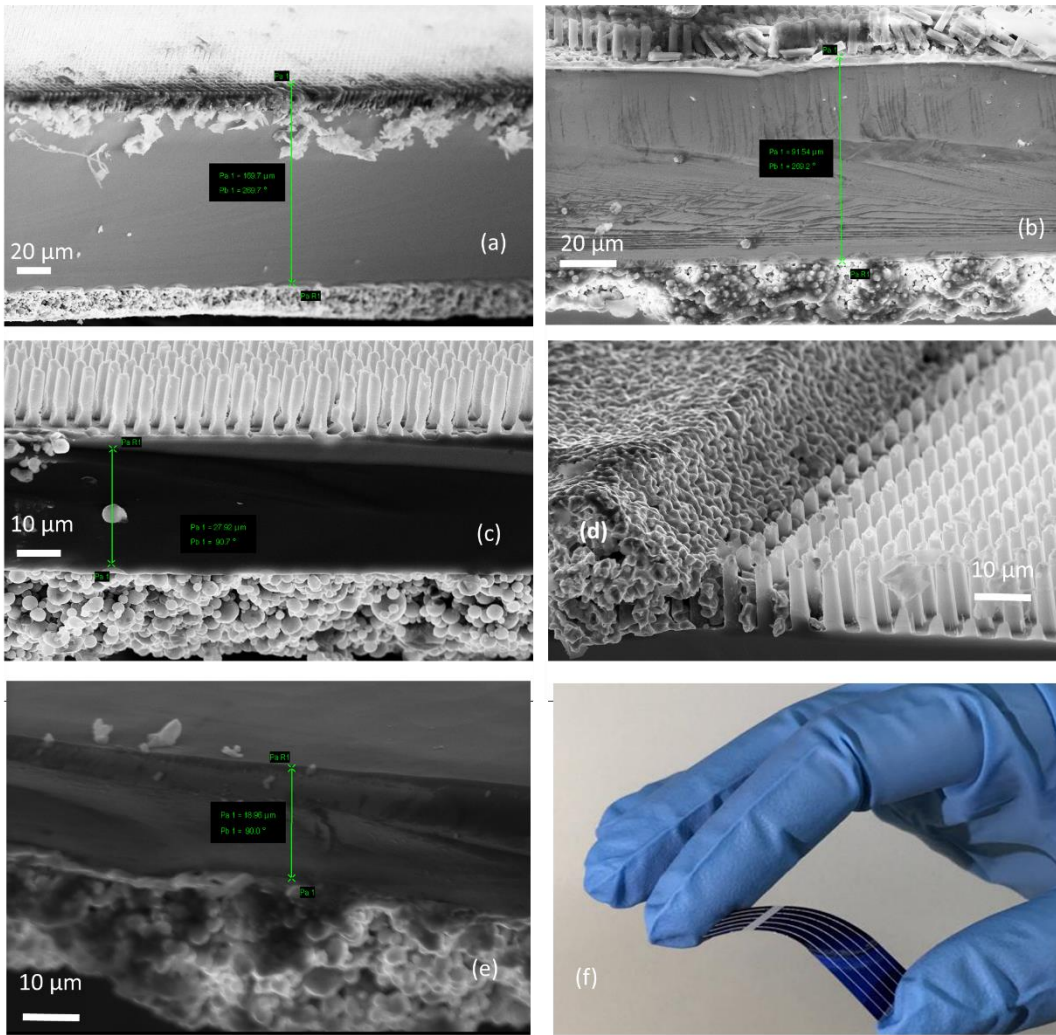


Figure 6.13. The cross-sectional SEM images of a) 1 h b) 2 h c) 3h etched radial junction solar cells, d) Ag finger on micropillars, e) SEM image, f) picture of thinnest planar solar cell.

However, after the metallization and optimized co-firing with respect to thicknesses were applied, the thinned radial junction solar cells and the planar cells with 15-30 μm thicknesses suffered from very low FF results. The EQE spectra of the samples are shown in Figure 6.14. Since co-firing process was optimized with respect to the thicknesses of solar cells, it was thought that the contact problem is due to the back side full Al metallization. There was not any problem during printing; however, as the

sample thickness decreased, bending effects were observed after co firing. Therefore, the results for all the samples decreased with increasing etching time. On the other hand, the etching was performed using a single side hole teflon holder for radial junction solar cells, so thicker Al layer had to be printed on the thinned region due to the support region of the samples. Therefore, all the thinned radial junction cells suffered from very low performance results.

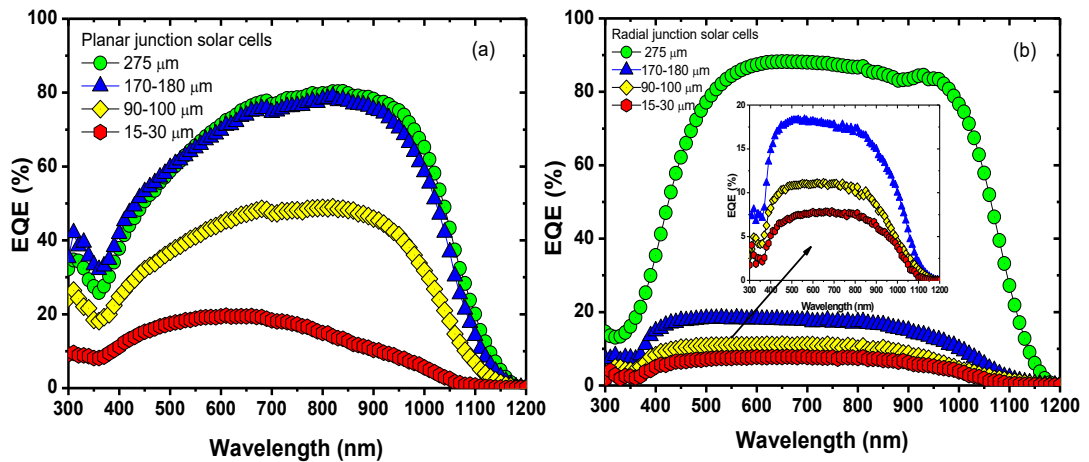


Figure 6.14. EQE spectra of unetched and etched a) planar and b) radial junction solar cells with metallization problem.

Therefore, thermal evaporation technique was used for the back-side metallization. Al-BSF was obtained by annealing at 800 °C temperature for 40 min. under N<sub>2</sub> atm. For the front sides, screen printing and optimized co-firing with respect to the wafer thickness were applied.

The performance parameters are tabulated in Table 6.2 and J-V results are graphed in Figure 6.15.

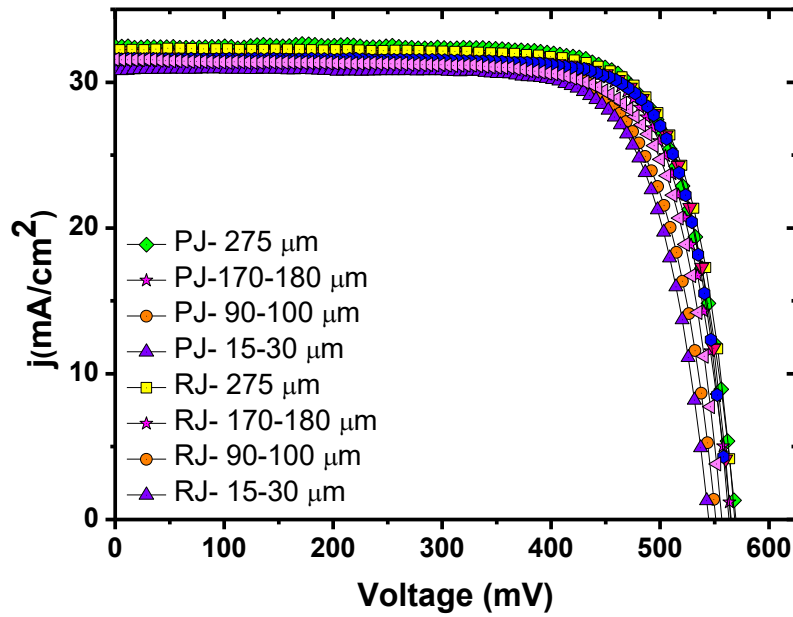


Figure 6.15. J-V curves of planar and radial junction solar cells with various thicknesses.

When the thickness of the solar cells decreases, it can be expected that the  $V_{oc}$  results would decrease. On the other hand, with a decrease in solar cell thickness, the light at the long wavelength region of the solar spectrum may not be absorbed very well or the carriers can be generated away from the junction region. According to the results, both  $J_{sc}$  and  $V_{oc}$  results for both type of the cells decreased with the decrease in the thickness of the solar cell. However, radial junction which enhances the performance of the solar cell both optically and electronically, has an advantage when the cell thickness decreases. While there was a very rapid decrement in the values of  $J_{sc}$  and  $V_{oc}$  in planar junction solar cells, a slower reduction in radial junction solar cells was observed. The change in  $J_{sc}$  and  $V_{oc}$  values as a function of cells thickness is also shown in Figure 6.16 for both types of solar cells.



Table 6.2. J-V curves of planar and radial junction solar cells with various thicknesses.

| Junction type-<br>etching duration | Efficiency<br>(%) | V <sub>oc</sub><br>(V) | J <sub>sc</sub><br>(mA/cm <sup>2</sup> ) | FF<br>(%) |
|------------------------------------|-------------------|------------------------|--|-----------|
| PJ- 275 μm                         | 14.13             | 0.570                  | 32.39                                    | 76.54     |
| PJ- 170-180 μm                     | 13.79             | 0.565                  | 32.08                                    | 76.07     |
| PJ- 90-100 μm                      | 13.06             | 0.551                  | 31.98                                    | 74.09     |
| PJ- 15-30 μm                       | 12.7              | 0.544                  | 30.86                                    | 75.69     |
| RJ- 275 μm                         | 14.19             | 0.568                  | 32.26                                    | 77.36     |
| RJ- 170-180 μm                     | 14.03             | 0.565                  | 31.67                                    | 78.43     |
| RJ- 90-100 μm                      | 13.94             | 0.562                  | 31.59                                    | 78.42     |
| RJ- 15-30 μm                       | 13.28             | 0.556                  | 31.55                                    | 75.65     |

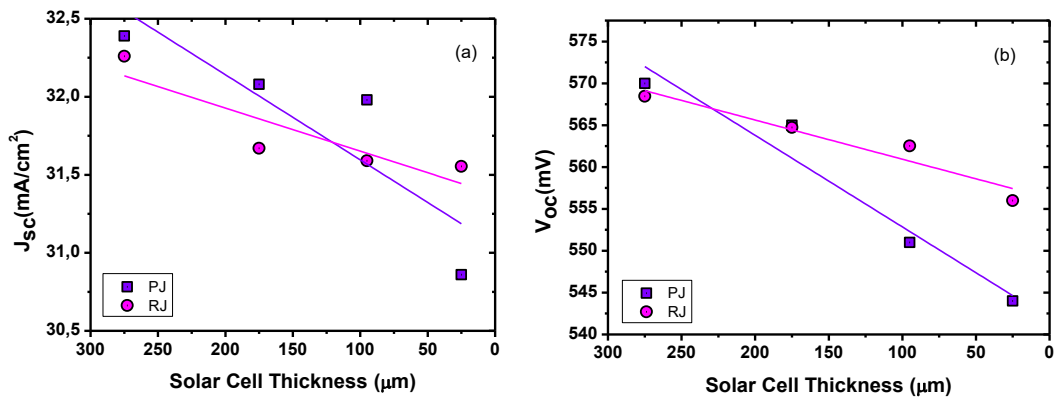


Figure 6.16. The change in a) Jsc and b) Voc values of planar and radial junction solar cells with respect to cell thicknesses.

In Figure 6.17, IQE and reflectance spectra of planar and radial junction solar cells with different thicknesses are given. The decrement at the long wavelength region of

IQE spectra of the cells in different thicknesses supports the decrement in  $V_{oc}$  results. As can be seen in the IQE spectra, the decrement at long wavelength in planar junction cells is more than that of radial junction solar cells.

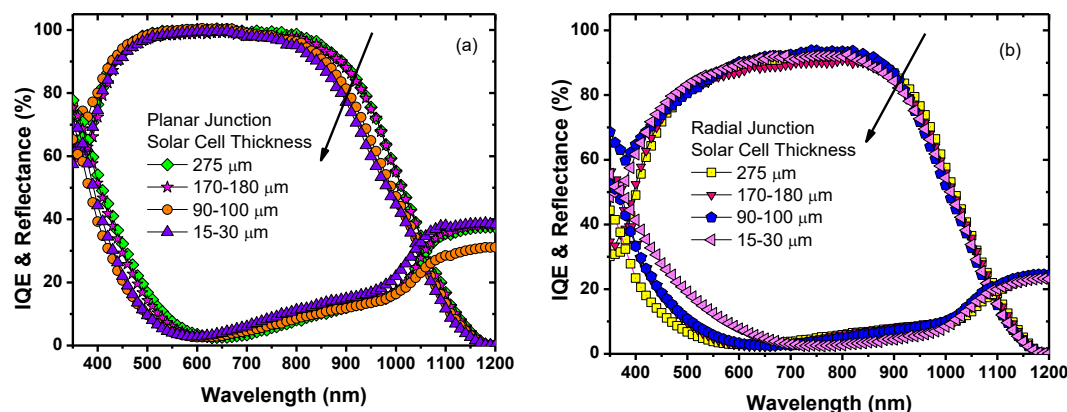


Figure 6.17. IQE and reflectance spectra of a) planar and b) radial junction solar cells as a function of wavelength with respect to cell thicknesses.

As a result, it was observed from both performance parameters and IQE results that radial junction solar cells were less affected by the use of thin Si substrate.

#### 6.4. Conclusion

In this study, it was shown that solar cells with three-dimensional radial junction are less affected by the use of thin Si substrate than those with planar junction cells. The reason is that minority carriers in these cells need to travel a shorter distance to reach the junction region in radial junction solar cells.

Since photolithography was applied to obtain micropillars on the surfaces and the samples were hard contacted during UV exposure, first the radial geometry was obtained then the samples were thinned. In order to protect micropillars from KOH etching, front sides of the radial junction cells were coated by  $\text{SiN}_x$  and single side KOH etching was performed. After standard solar cell fabrication processes and

optimized co firing conditions for wafer thicknesses, it was understood that screen printing metallization was not applicable for the fabrication of thin solar cells due to bending effects. Later, back side Al metallization was carried out by thermal evaporation technique.

As a result, the efficiency of the samples with the planar and radial geometries on thick Si substrates are close to each other, with the average efficiency values 14.13 % and 14.19%, respectively. On the other hand, when the cell thickness is decreased, the efficiency of the cells with radial junction degraded much less compared to the planar junction since  $V_{oc}$  values in radial junction cell were less effected by thinning. This is in agreement with the expectation that cells with a radial geometry whose carrier diffusion length to reach the junction is shortened are less sensitive to the material used. At the end, 12.7 % and 13.28 % conversion efficiencies were obtained from 15-30  $\mu\text{m}$  thick planar and radial junction solar cells, respectively.



## CHAPTER 7

### CONCLUSIONS

*“Keep your face to the sun and you will never see the shadows.”*

Helen Keller

In this thesis, radial junction solar cells with three-dimensional carrier collection property were studied. This type of solar cells contain densely packed Si nano/micropillar arrays on their surfaces. This geometry facilitates to separate the directions of charge carrier collection and light absorption and also provides a high junction area which depends on the aspect ratio of the pillars. Since it relaxes the long carrier lifetime requirement, three-dimensional, radial junction solar cell allows the use of low-quality substrate whose minority carrier diffusion length is shorter than the optical absorption depth. Moreover, with appropriate design of the pillar geometry, i.e. period, pillar length and diameter, the solar cell efficiency is enhanced due to the reduced surface reflectance and increased light harvesting.

Throughout this thesis work, to fabricate micropillars in appropriate geometry on the surfaces of solar cells, MAE method was used. Before applying MAE, the desired metal shapes were obtained on the surfaces by photolithography followed by thermal evaporation and lift-off processes.

In the first part of this thesis, the effect of micropillar length on the optical and electrical performances of the solar cell was studied. According to P atom distribution profile measured by Secondary Mass Ion Mass Spectrometry (SIMS), junction depth was estimated to be around 0.4  $\mu\text{m}$ . Therefore, the radii of the micropillars were

determined as 2  $\mu\text{m}$  so that the pillars are not fully doped and form radial junction. Until the tips and the sidewalls of the micropillars started to be etched, different metal assisted etching durations were applied to obtain micropillars in various length, the longest being about 6  $\mu\text{m}$ . In order to fabricate radial junction solar cells, standard processes for  $\text{POCl}_3$  tube furnace doping,  $\text{SiO}_2$  passivation, PECVD  $\text{SiN}_x$  coating as ARC, screen printed metallization, co-firing of the contacts and edge isolation were followed. Due to the thermal capacity of silicon, varied wafer thicknesses result in a differing co-firing temperature profile. Therefore, co-firing conditions, such as peak temperature and belt speed were optimized with respect to wafer thicknesses. According to the solar cell performance results,  $J_{sc}$  and efficiency values increased with increasing micropillar length since optical reflection from solar cells' surface decreased. As a result, the maximum efficiency value was obtained from the cell with  $\sim 6 \mu\text{m}$  micropillars. The best solar cell efficiency was obtained as 15.90 % which is one of the highest reported values in radial junction solar cells prepared by MAE technique.

The main purpose of the use of the radial junction solar cells is to ensure the availability of low quality, inexpensive materials in solar cell production, since it reduces the path length of minority carriers to reach the space charge region. Therefore, as another solar cell work, it was shown that the three-dimensional junction has an advantage over planar junction when Si wafers intentionally contaminated with metal impurities, were used. Au metal impurities with a U-shaped diffusion profile in Si, were diffused into the Si wafers for contamination. After the application of standard solar cell fabrication processes, while the efficiencies of the cells with radial and planar geometries having no contamination were close to each other 15.66% and 15.74%, in the case of contamination, the efficiency of the cells with radial junction degraded less compared to the planar junction with the values of 14.71 % and 12.72 %, respectively. The reason is that  $J_{sc}$  values in radial junction solar cells were affected less since the photogenerated carriers diffuse short distances to be collected. The

results are consistent with the expectation that solar cells with radial geometry are less sensitive to the quality of the substrate material used.

Moreover, a comparison of the performances of the planar and radial junction solar cells on different thicknesses Si wafers was investigated. The aim was to increase the proportion of the region containing micropillars in the cell and also to reduce the fabrication cost by allowing the use of thin Si substrates. Therefore, before the fabrication of thin Si solar cells, it was decided to change the MAE solution concentrations and the etchant in the solution to obtain longer micropillars. By increasing the HF concentration in the MAE solution to suppress the lateral etching and instead of H<sub>2</sub>O, using ethanol which has a lower surface tension, smoother etching was observed. Smooth micropillars up to 65  $\mu\text{m}$  in length were obtained on the surfaces and the surface reflection values were reduced to  $\sim 3\%$  close to the reflection value of the pyramid textured surfaces. However, since the standard cell production processes were not optimized according to the micropillar length, the cell efficiency of 17.27%, one of the highest efficiency values in radial junction cells, was obtained from the cell containing 11.5  $\mu\text{m}$  micropillars. In order to decrease the solar cell thicknesses, 50 % KOH anisotropic etching at 80-90<sup>0</sup>C was performed for different time durations. Since Al screen printing metallization for thin solar cells was not suitable due to bending effect, Al thermal evaporation was applied for back sides and annealing at 800 <sup>0</sup>C was performed for 40 minutes. By decreasing the thickness of the cells, it was observed that the efficiency values were less affected in three dimensional solar cells than in planar junction cells. With the decrease in solar cell thickness, the light at the long wavelength region of the solar spectrum may not be absorbed very well and the carriers can be generated away from the junction region. However, radial junction which enhances the performance of the solar cell both optically and electronically, had an advantage when the cell thickness decreases and so, less decrease in  $V_{oc}$  and  $J_{sc}$  values was observed. As a result, while the efficiencies of the planar and radial junction solar cells were close to each other  $\sim 14\%$ , before decreasing

the cell thicknesses, from 15-30  $\mu\text{m}$  thick planar and radial junction cells 12.70 % and 13.28 % efficiency values were obtained, respectively.

This thesis demonstrates that the three-dimensional p-n junction solar cells have an advantage over planar solar cells in the use of low-quality materials as well as for the solar cells with thin substrates. However, even if they have an advantage over conventional planar solar cells, high performance values in compliance with today's standards could not be obtained. Even if radial junction solar cells, with larger junction area provide an increase in the short circuit current, they suffer from surface recombination which leads to low open circuit voltage. Therefore, for future studies other passivation methods such as atomic layer deposition (ALD) can be applied taking the advantage of its conformality.



## REFERENCES

- [1] J. Nelson, *The Physics of Solar Cells*, Imperial College Press, 2003.
- [2] M. C. Putnam, M. A. Filler, B. M. Kayes, M. D. Kelzenberg, Y. B. Guan, N. S. Lewis, J. M. Eiler, H. A. Atwater, "Secondary Ion Mass Spectrometry of Vapor-Liquid-Solid Grown, Au-Catalyzed, Si Wires," *Nano Lett*, vol. 8, pp. 3109-3113, 2008.
- [3] "Central Intelligence Agency," [Online]. Available: <https://www.cia.gov/library/publications/the-world-factbook/>. [Accessed 15 June 2017].
- [4] Y. van Ingen, "Research Report XXV Annual Session: Taking measures to decrease global dependency on fossil fuels," in *Special Conference 2 on International Cooperation*, 2015.
- [5] R. K. Pachaur, L. A. Meyer., "Climate Change 2014: Synthesis Report: Contribution of Working Groups I, II and III to the Fifth Assessment Report of the Intergovernmental Panel on Climate Change," IPCC, Geneva, 2014.
- [6] R. Perez, M. Perez, "A fundamental look at energy reserves for the planet," The International Energy Agency SHC Programme Solar Update, 2009.
- [7] T.M. Razykov, C.S. Ferekides, D. Morel, E. Stefanakos, H.S. Ullal, and H. M. Upadhyaya, "Solar photovoltaic electricity: current status and future prospects," *Sol Energy*, vol. 85, p. 1580–608, 2011.
- [8] B Parida, S Iniyan, and R. Goic, "A review of solar photovoltaic technologies.," *Renew. Sustain Energy Rev.*, vol. 15, p. 1625–36, 2011.

- [9] Becquerel, A., "Mémoire sur les effets électriques produits sous linfluence des rayons solaires," *Comptes rendus*, vol. 9, p. 561–567, 1839.
- [10] A Goetzberger, C Hebling, and H.W. Schock, "Photovoltaic materials, history, status and outlook," *Mater Sci Eng*, vol. 1, p. 1–46, 2003.
- [11] R.W. Miles, K.M. Hynes, and I. Forbes, "Photovoltaic solar cells: an overview of state-of the-art cell development and environmental issues," *Prog Cryst Growth Charact Mater*, vol. 51, p. 1–42, 2005.
- [12] L.E. Chaar, L.A. Lamont, and N.E. Zein,, "Review of photovoltaic technologies.," *Renew Sustain Energy Rev.*, vol. 15, p. 2165–75, 2011.
- [13] A. Goetzberger, J. Luther, and G. Willeke,, "Solar cells: past, present, future.," *Sol Energy Mater Sol Cells*, vol. 74, pp. 1-11, 2002.
- [14] W. Adams and R. Day, "The action of light on selenium," *Proceedings of the Royal Society of London*, vol. 25, p. 113–117, 1876.
- [15] C. Fritts, "On the Fritts selenium cell and batteries," *Van Nostrands Engineering Magazine*, vol. 32, p. 388–395, 1885.
- [16] R. Ohl, "Light sensitive electric device". US Patent 2402662, 1941.
- [17] R. Ohl, "Light-sensitive electric device including silicon". US Patent 2443542, 1941.
- [18] D. Chapin, C. Fuller and G. Pearson, "A new silicon p-n junction photocell for converting solar radiation into electrical power," *Journal of Applied Physics*, vol. 25, p. 676–677, 1954.
- [19] W. Shockley and H. J. Queisser, "Detailed Balance Limit of Efficiency of p-n Junction Solar Cells," *Journal of Applied Physics*, vol. 32, p. 510, 1961.

- [20] E. T. Yu and J. van de Lagemaat, "Photon management for photovoltaics," *MRS Bulletin*, vol. 36, pp. 424-428, 2011.
- [21] G. Flatgen, S. Wasle, M. Lubke, C. Eickes, G. Radhakrishnan, K. Doblhofer and G. Ertl, "Autocatalytic mechanism of H<sub>2</sub>O<sub>2</sub> reduction on Ag electrodes in acidic electrolyte: experiments and simulations," *Electrochim. Acta*, vol. 44, p. 4499, 1999.
- [22] D. M. Callahan, J. N. Munday, and H. A. Atwater, "Solar Cell light trapping beyond the ray optic limit," *Nano letters*, vol. 12, pp. 214-8, 2012.
- [23] X. Wang, Design and analysis of solar cells by coupled electrical - optical simulation, Purdue University.: PhD thesis., 2014.
- [24] M. A. Green, and K. Emery, "Solar cell efficiency tables (version 2)," *Progress in Photovoltaics: Research and Applications*, vol. 1, pp. 225-227, 1995.
- [25] M. A. Green, K. Emery, K. Bücher, and D. L. King, "Solar cell efficiency tables (version 6)," *Progress in Photovoltaics: Research and Applications*, vol. 3, pp. 229-233, 1995.
- [26] M. A. Green, K. Emery, K. Bücher, and D. L. King, "Solar cell efficiency tables (version 7)," *Progress in Photovoltaics: Research and Applications*, vol. 4, pp. 59-62, 1996.
- [27] M. A. Green, K. Emery, K. Bücher, D. L. King, and S. Igari, "Solar cell efficiency tables (version 8)," *Progress in Photovoltaics: Research and Applications*, vol. 4, pp. 321-325, 1996.
- [28] M. A. Green, K. Emery, K. Bücher, D. L. King, and S. Igari, "Solar cell efficiency tables (version 11)," *Progress in Photovoltaics: Research and Applications*, vol. 6, pp. 35-42, 1998.

- [29] M. A. Green, K. Emery, K. Bücher, D. L. King, and S. Igari, "Solar cell efficiency tables (version 12)," *Progress in Photovoltaics: Research and Applications*, vol. 6, pp. 265-270, 1998.
- [30] M. A. Green, K. Emery, K. Bücher, D. L. King, and S. Igari, "Solar cell efficiency tables (version 13)," *Progress in Photovoltaics: Research and Applications*, vol. 7, pp. 31-37, 1999.
- [31] M. A. Green, K. Emery, D. L. King, S. Igari, and W. Warta, "Solar cell efficiency tables (version 16)," *Progress in Photovoltaics: Research and Applications*, vol. 8, pp. 377-383, 2000.
- [32] M. A. Green, K. Emery, D. L. King, S. Igari, and W. Warta, "Solar cell efficiency tables (version 17)," *Progress in Photovoltaics: Research and Applications*, vol. 9, pp. 49-56, 2001.
- [33] M. A. Green, K. Emery, D. L. King, S. Igari, and W. Warta, "Solar cell efficiency tables (version 18)," *Progress in Photovoltaics: Research and Applications*, vol. 9, pp. 287-293, 2001.
- [34] M. A. Green, K. Emery, D. L. King, S. Igari, and W. Warta, "Solar cell efficiency tables (version 19)," *Progress in Photovoltaics: Research and Applications*, vol. 10, pp. 55-61, 2002.
- [35] M. A. Green, K. Emery, D. L. King, S. Igari, and W. Warta, "Solar cell efficiency tables (version 20)," *Progress in Photovoltaics: Research and Applications*, vol. 10, pp. 355-360, 2002.
- [36] M. A. Green, K. Emery, D. L. King, S. Igari, and W. Warta, "Solar cell efficiency tables (version 21)," *Progress in Photovoltaics: Research and Applications*, vol. 11, pp. 39-45, 2003.

- [37] M. A. Green, K. Emery, D. L. King, S. Igari, and W. Warta, "Solar cell efficiency tables (version 22)," *Progress in Photovoltaics: Research and Applications*, vol. 11, pp. 347-352, 2003.
- [38] M. A. Green, K. Emery, D. L. King, S. Igari, and W. Warta, "Solar cell efficiency tables (version 23)," *Progress in Photovoltaics: Research and Applications*, vol. 12, pp. 55-62, 2004.
- [39] M. A. Green, K. Emery, D. L. King, S. Igari, and W. Warta, "Solar cell efficiency tables (version 24)," *Progress in Photovoltaics: Research and Applications*, vol. 12, pp. 365-372, 2004.
- [40] M. A. Green, K. Emery, D. L. King, W. Warta, and S. Igari, "Solar cell efficiency tables (version 26)," *Progress in Photovoltaics: Research and Applications*, vol. 13, pp. 387-392, 2005.
- [41] M. A. Green, K. Emery, D. L. King, Y. Hishikawa, and W. Warta, "Solar cell efficiency tables (version 27)," *Progress in Photovoltaics: Research and Applications*, vol. 14, pp. 45-51, 2006.
- [42] M. A. Green, K. Emery, D. L. King, Y. Hishikawa, and W. Warta, "Solar cell efficiency tables (version 28)," *Progress in Photovoltaics: Research and Applications*, vol. 14, pp. 455-461, 2006.
- [43] M. A. Green, K. Emery, D. L. King, Y. Hishikawa, and W. Warta, "Solar cell efficiency tables (version 29)," *Progress in Photovoltaics: Research and Applications*, vol. 15, pp. 35-40, 2007.
- [44] M. A. Green, K. Emery, Y. Hishikawa, and W. Warta, "Solar cell efficiency tables (version 30)," *Progress in Photovoltaics: Research and Applications*, vol. 15, pp. 425-430, 2007.

- [45] M. A. Green, K. Emery, Y. Hishikawa, and W. Warta, "Solar cell efficiency tables (version 31)," *Progress in Photovoltaics: Research and Applications*, vol. 16, pp. 61-67, 2008.
- [46] M. A. Green, K. Emery, Y. Hishikawa, and W. Warta, "Solar cell efficiency tables (version 32)," *Progress in Photovoltaics: Research and Applications*, vol. 16, pp. 435-440, 2008.
- [47] M. A. Green, K. Emery, Y. Hishikawa, and W. Warta, "Solar cell efficiency tables (version 33)," *Progress in Photovoltaics: Research and Applications*, vol. 17, pp. 85-94, 2009.
- [48] M. A. Green, K. Emery, Y. Hishikawa, and W. Warta, "Solar cell efficiency tables (version 34)," *Progress in Photovoltaics: Research and Applications*, vol. 17, pp. 320-326, 2009.
- [49] M. A. Green, K. Emery, Y. Hishikawa, and W. Warta, "Solar cell efficiency tables (version 35)," *Progress in Photovoltaics: Research and Applications*, vol. 18, pp. 144-150, 2010.
- [50] M. A. Green, K. Emery, Y. Hishikawa, and W. Warta, "Solar cell efficiency tables (version 36)," *Progress in Photovoltaics: Research and Applications*, vol. 18, pp. 346-352, 2010.
- [51] M. A. Green, K. Emery, Y. Hishikawa, and W. Warta, "Solar cell efficiency tables (version 37)," *Progress in Photovoltaics: Research and Applications*, vol. 19, pp. 84-92, 2011.
- [52] M. A. Green, K. Emery, Y. Hishikawa, W. Warta, and E. D. Dunlop, "Solar cell efficiency tables (version 38)," *Progress in Photovoltaics: Research and Applications*, vol. 19, pp. 565-572, 2011.

- [53] M. A. Green, K. Emery, Y. Hishikawa, W. Warta, and E. D. Dunlop, "Solar cell efficiency tables (version 39)," *Progress in Photovoltaics: Research and Applications*, vol. 20, pp. 12-20, 2012.
- [54] M. A. Green, K. Emery, Y. Hishikawa, W. Warta, and E. D. Dunlop, "Solar cell efficiency tables (version 40)," *Progress in Photovoltaics: Research and Applications*, vol. 20, pp. 606-614, 2012.
- [55] M. A. Green, K. Emery, Y. Hishikawa, W. Warta, and E. D. Dunlop, "Solar cell efficiency tables (version 41)," *Progress in Photovoltaics: Research and Applications*, vol. 21, pp. 1-11, 2013.
- [56] M. A. Green, K. Emery, Y. Hishikawa, W. Warta, and E. D. Dunlop, "Solar cell efficiency tables (version 42)," *Progress in Photovoltaics: Research and Applications*, vol. 21, pp. 827-837, 2013.
- [57] M. A. Green, K. Emery, Y. Hishikawa, W. Warta, and E. D. Dunlop, "Solar cell efficiency tables (version 43)," *Progress in Photovoltaics: Research and Applications*, vol. 22, pp. 1-9, 2014.
- [58] M. A. Green, K. Emery, Y. Hishikawa, W. Warta, and E. D. Dunlop, "Solar cell efficiency tables (version 44)," *Progress in Photovoltaics: Research and Applications*, vol. 22, pp. 701-710, 2014.
- [59] M. A. Green, K. Emery, Y. Hishikawa, W. Warta, and E. D. Dunlop, "Solar cell efficiency tables (version 45)," *Progress in Photovoltaics: Research and Applications*, vol. 23, pp. 1-9, 2015.
- [60] M. A. Green, K. Emery, Y. Hishikawa, W. Warta, and E. D. Dunlop, "Solar cell efficiency tables (version 46)," *Progress in Photovoltaics: Research and Applications*, vol. 23, pp. 805-812, 2015.

- [61] M. A. Green, K. Emery, Y. Hishikawa, W. Warta, and E. D. Dunlop, "Solar cell efficiency tables (version 47)," *Progress in Photovoltaics: Research and Applications*, vol. 24, pp. 3-11, 2016.
- [62] M. A. Green, K. Emery, Y. Hishikawa, W. Warta, and E. D. Dunlop, "Solar cell efficiency tables (version 48)," *Progress in Photovoltaics: Research and Applications*, vol. 24, pp. 905-913, 2016.
- [63] M. A. Green, K. Emery, Y. Hishikawa, W. Warta, and E. D. Dunlop, Dean H. Levi, Anita W.H. Ho-Baillie, "Solar cell efficiency tables (version 49)," *Progress in Photovoltaics: Research and Applications*, vol. 25, pp. 3-13, 2017.
- [64] M. A. Green, Y. Hishikawa, W. Warta, and E. D. Dunlop, Dean H. Levi, Jochen Hohl-Ebinger, Anita W.H. Ho-Baillie, "Solar cell efficiency tables (version 50)," *Progress in Photovoltaics: Research and Applications*, vol. 25, pp. 668-676, 2017.
- [65] M. A. Green, Y. Hishikawa, E. D. Dunlop, D. H. Levi, J. Hohl-Ebinger A. W.Y. Ho-Baillie, "Solar cell efficiency tables (version 51)," *Progress in Photovoltaics: Research and Applications*, vol. 26, pp. 3-12, 2018.
- [66] M. A. Green, Y. Hishikawa, E. D. Dunlop, D. H. Levi, J. Hohl-Ebinger A. W.Y. Ho-Baillie, "Solar cell efficiency tables (version 52)," *Progress in Photovoltaics*, vol. 26, pp. 427-436, 2018.
- [67] O. E. Semonin, J. M. Luther, S. Choi, H.-Y. Chen, J. Gao, A. J. Nozik, et al., "Peak external photocurrent quantum efficiency exceeding 100% via MEG in a quantum dot solar cell," *Science (New York, N.Y.)*, vol. 334, pp. 1530-3, 2011.
- [68] A. Marti and A. Luque, "Increasing the efficiency of ideal solar cells by photon induced transitions at intermediate levels," *Phys. Rev. Lett.*, vol. 78, pp. 5014-5017, 1997.



- [69] D. König, K. Casalenuovo, Y. Takeda, G. Conibeer, J. F. Guillemoles, R. Patterson, et al., "Hot carrier solar cells: Principles, materials and design," *Physica E: Low-dimensional Systems and Nanostructures*, vol. 42, pp. 2862-2866, 2010.
- [70] Fraunhofer Institute for Solar Energy Systems, ISE, "Photovoltaics Report," Freiburg, 27 August 2018.
- [71] A. M. Kuhlmann, "The Second Most Abundant Element in the Earth's Crust," *Journal of Metals*, vol. 15, pp. 502-505, 1963.
- [72] M. Hosenuzzaman, et al., "Global prospects, progress, policies, and environmental impact of solar photovoltaic power generation," *Renew Sustain Energy Rev.*, vol. 41, pp. 284-97, 2015.
- [73] J.S. Lacerda, J.C.J.M. Van Den Bergh, "Diversity in solar photovoltaic energy: implications for innovation and policy," *Renew Sustain Energy Rev.*, vol. 54, pp. 331-40, 2016.
- [74] M. A. Green, and M. J. Keevers, "Optical properties of intrinsic Si at 300 K," *Progress in Photovoltaics: Research and Applications*, vol. 3, pp. 189-192, 1995.
- [75] Z. Lan, and J. Li, "Photovoltaic technology and electricity saving strategies for fixed-velocity-measuring system," *Telkomnika Indones J Electr Eng*, vol. 6, pp. 4419-26, 2014.
- [76] A.D. Compaan, "Photovoltaics: clean power for the 21st century," *Sol Energy Mater Sol Cells*, vol. 90, pp. 2170-80, 2006.
- [77] J. Peng, L. Lu, and H. Yang, "Review on life cycle assessment of energy payback and greenhouse gas emission of solar photovoltaic systems," *Renew Sustain Energy Rev.*, vol. 19, pp. 255-74, 2013.

- [78] V.V. Tyagi, N.A.A. Rahim, N.A. Rahim, and J.A.L. Selvaraj, "Progress in solar PV technology: research and achievement," *Renew Sustain Energy Rev.*, vol. 20, pp. 443-61, 2013.
- [79] U. Gangopadhyay, S. Jana, and S. Das, "State of Art of Solar Photovoltaic Technology," in *Proceedings of International Conference on Solar Energy Photovoltaics*, 2013.
- [80] V. Avrutin, N. Izyumskaya, and H. Morkoç, "Semiconductor solar cells: recent progress in terrestrial applications," *Superlattices Microstruct*, vol. 49, pp. 337-64, 2011.
- [81] E. Yablonovitch, "Statistical ray optics," *Journal of the Optical Society of America*, vol. 72, pp. 899-907, 1982.
- [82] M. A. Green, "Lambertian light trapping in textured solar cells and light-emitting diodes: Analytical solutions," *Progress in Photovoltaics: Research and Applications*, vol. 10, pp. 235-241, 2002.
- [83] D. Thorp and S. R. Wenham, "Ray-tracing of arbitrary surface textures for lighttrapping in thin silicon solar cells," *Solar Energy Materials and Solar Cells*, vol. 48, p. 295–301, 2007.
- [84] J. F. Wise, "Silicon solar cell". US Patent Patent Application Serial No. 579,801, now abandoned, September 1966.
- [85] W. P. Rahilly, "Vertical multijunction solar cells," in *Conference Record of the Ninth IEEE Photovoltaic Specialists Conference*, 1972.
- [86] S. R. Wenham and M. A. Green, "Novel parallel multijunction solar cell," *Applied Physics Letters*, vol. 65, p. 2907–2909, 1994.

- [87] A. B. Sproul, S. Edmiston, S.R. Wenham, G.H. Heiser, and M.A. Green, "Innovative structures for thin film crystalline silicon solar cells to give high efficiencies from low quality silicon," in *Conference Record of the First World Conference on Photovoltaic Energy Conversion*, 1994.
- [88] H. Diepers, "Method of manufacturing solar cells, utilizing single-crystal whisker growth". US Patent 4155781, 22 May 1977.
- [89] B. M. Kayes, H. A. Atwater, and N. S. Lewis, "Comparison of the device physics principles of planar and radial p-n junction nanorod solar cells," *J. Appl. Phys.*, vol. 97, p. 114302, 2005.
- [90] M. D. Kelzenberg, S. W. Boettcher, J. A. Petykiewicz, D. B. Turner-Evans, M. C. Putnam, E. L. Warren, J. M. Supurgeon, R. M. Briggs, N. S. Lewis, and H. A. Atwater, "Enhanced absorption and carrier collection in Si wire arrays for photovoltaic applications," *Nature Mater*, vol. 9, pp. 239-244, 2010.
- [91] V. Schlosser, "Limiting Factors for the Application of Crystalline Upgraded Metallurgical Grade Silicon," *IEEE Transactions On Electron Devices*, vol. 31, pp. 610-613, 1984.
- [92] T. Daud, K. M. Koliwad, and F. G. Allen, "Effect of Grain-Boundaries in Silicon on Minority Carrier Diffusion Length and Solar Cell Efficiency," *Applied Physics Letters*, vol. 33, pp. 1009-1011, 1978.
- [93] M. Gharghi, "On the design and applicability of nanowire solar cells using low-grade semiconductors," *J. Appl. Phys.*, vol. 111, p. 0345501, 2012.
- [94] M. Gharghi, E. Fathi, B. Kante, S. Sivoththaman, and X. Zhang, "Heterojunction Silicon Microwire Solar Cells," *Nano Lett.*, vol. 12, pp. 6278-6282, 2012.

- [95] M. D. Kelzenberg, M. C. Putnam, D. B. Turner-Evans, N. S. Lewis, H. A. Atwater, "Predicted Efficiency of Si Wire Array Solar Cells," in *Proceedings of the 34th IEEE PVSC*, 2009.
- [96] H. Shen, Y. Yuwen, X. Wang, J. I. Ramirez, Y. V. Li, Y. Ke, C. E. Kendrick, N. J. Podraza, T. N. Jackson, E. C. Dickey, T. S. Mayer, and J. M. Redwing, "Effect of c-Si Doping Density on Heterojunction with Intrinsic Thin Layer (HIT) Radial Junction Solar Cells," in *Proceedings of the 39th IEEE PVSC*, 2013.
- [97] J. D. Christesen, X. Zhang, C. W. Pinion, T. A. Celano, C. J. Flynn, and J. F. Cahoon, "Design Principles for Photovoltaic Devices Based on Si Nanowires with Axial or Radial p–n Junctions," *Nano Lett.*, vol. 12, pp. 6024-6029, 2012.
- [98] G. Jia, I. Höger, A. Gawlik, J. Dellith, L. R. Bailey, A. Ulyashin, and F. Falk, "Wet chemically prepared silicon nanowire arrays on low-cost substrates for photovoltaic applications," *Phys. Status Solidi A*, vol. 210, pp. 728-731, 2013.
- [99] J-Y. Jung, Z. Guo, S-W. Jee, H-D. Um, K-T. Park, M. S. Hyun, J. M. Yang and J-H. Lee, "A waferscale Si wire solar cell using radial and bulk p–n junctions," *Nanotechnology*, vol. 21, p. 445303, 2010.
- [100] O. Gunawan, K. Wang, B. Fallahazad, Y. Zhang, E. Tutuc, and S. Guha, "High performance wire-array silicon solar cells," *Prog. Photovolt: Res. Appl.*, vol. 19, pp. 307-312, 2011.
- [101] H.-D. Um, N. Kim, K. Lee, I. Hwang, J. H. Seo, Y. J. Yu, P. Duane, M. Wober, and K. Seo, "Versatile control of metal-assisted chemical etching for vertical silicon microwire arrays and their photovoltaic applications," *Sci. Rep.*, vol. 5, p. 11277, 2015.

- [102] K. Lee, I. Hwang, N. Kim, D. Choi, H-D. Um, S. Kim and K. Seo, "17,6% Efficient radial junction solar cells using silicon nano/micro hybrid structures," *Nanoscale*, vol. 8, p. 14473, 2016.
- [103] L. Hu and G. Chen, "Analysis of Optical Absorption in Silicon Nanowire Arrays for Photovoltaic Applications," *Nano Lett.*, vol. 7, p. 11, 2007.
- [104] H. Alaeian, A. C. Atre and J. A. Dionne, "Optimized light absorption in Si wire array solar cells," *J. Opt.*, vol. 14, p. 024006, 2012.
- [105] K-T. Park, Z. Guo, H-D. Um, J-Y. Jung, J. M. Yang, S. K. Lim, Y. S. Kim, and J-H. Lee, "Optical properties of Si microwires combined with nanoneedles for flexible thin film photovoltaics," *Optics Express*, vol. 19, pp. A41-A50, 2011.
- [106] E. C. Garnett and P. Yang, "Silicon Nanowire Radial p-n Junction Solar Cells," *J. Am. Chem. Soc.*, vol. 130, p. 9224–9225, 2008.
- [107] Z. Huang, X. Zhang, M. Reiche, L. Liu, W. Lee, T. Shimizu, S. Senz, and U. Gösele, "Extended arrays of vertically aligned sub-10 nm diameter [100] Si nanowires by metal-assisted chemical etching," *Nano Lett.*, vol. 8, p. 3046–51, 2008.
- [108] H. P. Yoon, Y. A. Yuwen, C. E. Kendrick, G. D. Barber, N. J. Podraza, J. M. Redwing, T. E. Mallouk, C. R. Wronski, and T. S. Mayer, "Enhanced conversion efficiencies for pillar array solar cells fabricated from crystalline silicon with short minority carrier diffusion lengths," *Appl. Phys. Letters*, vol. 96, p. 213503, 2010.
- [109] E. Garnett, and P. Yang, "Light trapping in silicon nanowire solar cells," *Nano Lett.*, vol. 10, p. 1082–87, 2010.

- [110] B. Tian, X. Zheng, T. J. Kempa, Y. Fang, N. Yu, G. Yu, J. Huang and C. M. Lieber, "Coaxial silicon nanowires as solar cells and nanoelectronic power sources," *Nature Letters*, vol. 449, pp. 885-90, 2007.
- [111] M. C. Putnam, D. B. Turner-Evans, M. D. Kelzenberg, S. W. Boettcher, N. S. Lewis, and H. A. Atwater, "10  $\mu\text{m}$  minority-carrier diffusion lengths in Si wires synthesized by Cu-catalyzed vapor-liquid-solid growth," *Appl. Phys. Lett.*, vol. 95, p. 163116, 2009.
- [112] J. R. Maiolo, B. M. Kayes, M. A. Filler, M. C. Putnam, M. D. Kelzenberg, H. A. Atwater and N. S. Lewis, "High aspect ratio silicon wire array photoelectrochemical cells," *J. Am. Chem. Soc.*, vol. 129, p. 12346, 2007.
- [113] S. W. Boettcher, J. M. Spurgeon, M. C. Putnam, E. L. Warren, D. B. T. Evans, M. D. Kelzenberg, J. R. Maiolo, H. A. Atwater and N. S. Lewis, "Energy-conversion properties of vapor-liquid-solid-grown silicon wire-array photocathodes," *Science*, vol. 327, p. 185, 2010.
- [114] C. E. Kendrick, H. P. Yoon, Y. A. Yuwen, G. D. Barber, H. Shen, T. E. Mallouk, E. C. Dickey, T. S. Mayer, and J. M. Redwing, "Radial junction silicon wire array solar cells fabricated by gold-catalyzed vapor-liquid-solid growth," *Applied Physics Letters*, vol. 97, p. 143108, 2010.
- [115] B. M. Kayes, M. A. Filler, M. C. Putnam, M. D. Kelzenberg, N. S. Lewis, and H. A. Atwater, "Growth of vertically aligned Si wire arrays over large areas ( $> 1 \text{ cm}^2$ ) with Au and Cu catalysts," *Applied Physics Letters*, vol. 91, pp. 103110-3, 2007.
- [116] M. C. Putnam, S. W. Boettcher, M. D. Kelzenberg, D. B. Turner-Evans, J. M. Spurgeon, E. L. Warren, R. M. Briggs, N. S. Lewis, and H. A. Atwater, "Si microwire-array solar cells," *Energy Environ. Sci.*, vol. 3, p. 1037, 2010.

- [117] Y. J. Dong, B. Z. Tian, T. J. Kempa and C. M. Lieber, "Coaxial Group III–Nitride Nanowire Photovoltaics," *Nano Lett.*, vol. 9, p. 2183–2187, 2009.
- [118] M. Law, J. Goldberger, and P. Yang, "Semiconductor nanowires and nanotubes," *Annu. Rev. Mater. Res.*, vol. 34, p. 83–122, 2004.
- [119] J. Zhu, H. Peng, A.F. Marshall, D. M. Barnett, W. D. Nix, and Y. Cui, "Formation of chiral branched nanowires by the Eshelby Twist," *Nat. Nanotechnol.*, vol. 3, p. 477–81, 2008.
- [120] A. I. Persson, M.W. Larsson, S. Stenström, B. J. Ohlsson, L. Samuelson, and L. R. Wallenberg, "Solid-phase diffusion mechanism for GaAs nanowire growth," *Nature Mater.*, vol. 3, p. 677–81, 2004.
- [121] K. A. Dick, K. Deppert, L. S. Karlsson, L. R. Wallenberg, L. Samuelson, and W. Seifert, "A new understanding of Au-assisted growth of III–V semiconductor nanowires," *Adv. Funct. Mater.* , vol. 15, p. 1603–10, 2005.
- [122] J. K. Hyun, S. Zhang, L. J. Lauhon, "Nanowire heterostructures," *Annu. Rev. Mater. Res.* , vol. 43, pp. 451-479, 2013.
- [123] Z. Fan, H. Razavi, J. Do, A. Moriwaki, O. Ergen, Y. L. Chueh, P. W. Leu, J. C. Ho, T. Takahashi, L. A. Reichertz, S. Neale, K. Yu, M. Wu, J. W. Ager, and A. Javey, "Three-dimensional nanopillar-array photovoltaics on low-cost and flexible substrates," *Nature Mater*, vol. 8, pp. 648-53, 2009.
- [124] T. Martensson, P. Carlberg, M. Borgström, L. Montelius, W. Seifert, and L. Samuelson , "Nanowire arrays defined by nanoimprint lithography," *Nano Lett.*, vol. 4, pp. 699-702, 2004.
- [125] Z. Huang, H. Fang, and J. Zhu, "Fabrication of silicon nanowire arrays with controlled diameter, length, and density," *Adv. Mater*, vol. 19, p. 744–48, 2007.

- [126] G. Jia, M. Steglich, I. Sill, F. Falk, "Core-shell heterojunction solar cells on silicon nanowire arrays," *Solar Energy Materials & Solar Cells*, vol. 96, pp. 226-230, 2012.
- [127] G. Jia, A. Gawlik, J. Bergmann, B. Eisenhauer, S. Schonherr, G. Andra, and F. Falk, "Silicon Nanowire Solar Cells With Radial p-n Heterojunction on Crystalline Silicon Thin Films: Light Trapping Properties," *IEEE Journal of Photovoltaics*, vol. 4, pp. 28-32, 2014.
- [128] G. Baytemir, F. Es, A. S. Alagoz, R. Turan, "Radial junction solar cells prepared on single crystalline silicon wafers by metal-assisted etching," *Phys. Status Solidi RRL*, vol. 11, p. 1600444, 2017.
- [129] I. Hwang, H-D. Um, B-S. Kim, M. Wober and K. Seo, "Flexible crystalline silicon radial junction photovoltaics with vertically aligned tapered microwires," *Energy Environ. Sci.*, vol. 11, p. 641, 2018.
- [130] J. Goldberger, A. I. Hochbaum, R. Fan, and P. Yang, "Silicon Vertically Integrated Nanowire Field Effect Transistors," *Nano Lett.*, vol. 6, p. 973, 2006.
- [131] V. Schmidt, H. Riel, S. Senz, S. Karg, W. Riess, and U. Gösele, "Realization of a Silicon Nanowire Vertical Surround-Gate Field-Effect Transistor," *Small*, vol. 2, p. 85, 2006.
- [132] S. G. Cloutier, C. H. Hsu, P. A. Kossyrev, and J. Xu, "Enhancement of radiative recombination in silicon via phonon localization and selection-rule breaking," *Adv. Mater* , vol. 18, p. 841, 2006.
- [133] A.K. Buin, A. Verma, A. Svizhenko, and M.P. Anantram, "Significant Enhancement of Hole Mobility in [110] Silicon Nanowires Compared to Electrons and Bulk Silicon," *Nano Lett.*, vol. 8, p. 760, 2008.



- [134] K. H. Hong, J. Kim, S. H. Lee, and J. K. Shin, "Strain-Driven Electronic Band Structure Modulation of Si Nanowires," *Nano Lett.*, vol. 8, p. 1335, 2008.
- [135] H. Fang, X. D. Li, S. Song, Y. Xu, and J. Zhu, "Fabrication of slantingly-aligned silicon nanowire arrays for solar cell applications," *Nanotechnology*, vol. 19, p. 255703, 2008.
- [136] D. D. Ma, C. S. Lee, F. C. Au, S. Y. Tong, and S. T. Lee, "Small-diameter silicon nanowire surfaces," *Science*, vol. 299, p. 1874, 2003.
- [137] Z. Huang, T. Shimizu, S. Senz, Z. Zhang, N. Geyer, and U. Gösele, "Oxidation Rate Effect on the Direction of Metal-Assisted Chemical and Electrochemical Etching of Silicon," *J. Phys. Chem. C.*, vol. 114, p. 10683, 2010.
- [138] Z. P. Huang, T. Shimizu, S. Senz, Z. Zhang, X. X. Zhang, W. Lee, N. Geyer, and U. Gösele, "Ordered arrays of vertically aligned [110] silicon nanowires by suppressing the crystallographically preferred <100> etching directions," *Nano Lett.*, vol. 9, p. 2519, 2009.
- [139] Y. Yasukawa, H. Asoh, and S. Ono, "Periodic GaAs Convex and Hole Arrays Produced by Metal-Assisted Chemical Etching," *Japanese Journal of Applied Physics*, vol. 49, p. 116502, 2010.
- [140] M. DeJarld, J. C. Shin, W. Chern, D. Chanda, K. Balasundaram, J. A. Rogers, and X. Li, "Formation of High Aspect Ratio GaAs Nanostructures with Metal-Assisted Chemical Etching," *Nano Lett.*, vol. 11, p. 5259, 2011.
- [141] X. Geng, B. K. Duan, D. A. Grismer, L. Zhao, and P. W. Bohn, "Monodisperse GaN nanowires prepared by metal-assisted chemical etching with in situ catalyst deposition," *Electrochemistry Communications*, vol. 19, p. 39, 2012.

- [142] A. I. Hochbaum, R. K. Chen, R. D. Delgado, W. J. Liang, E. C. Garnett, M. Najarian, A. Majumdar, and P. D. Yang, "Enhanced thermoelectric performance of rough silicon nanowires," *Nature*, vol. 451, p. 163, 2008.
- [143] B. H. Zhang, H. S. Wang, L. H. Lu, K. L. Ai, G. Zhang, and X. L. Cheng, "Large-Area Silver-Coated Silicon Nanowire Arrays for Molecular Sensing Using Surface-Enhanced Raman Spectroscopy," *Adv. Funct. Mater.*, vol. 18, p. 2348, 2008.
- [144] M. L. Zhang, C. Q. Yi, X. Fan, K. Q. Peng, N. B. Wong, M. S. Yang, R. Q. Zhang, and S. T. Lee, "A surface-enhanced Raman spectroscopy substrate for highly sensitive label-free immunoassay," *Appl. Phys. Lett.*, vol. 92, p. 043116, 2008.
- [145] Z. Huang, N. Geyer, P. Werner, J. Boor, and U. Gösele, "Metal-Assisted Chemical Etching of Silicon: A Review," *Adv. Mater.*, vol. 23, p. 285, 2011.
- [146] D. Dimova-Malinovska, M. Sendova-Vassileva, N. Tzenov and M. Kamenova, "Preparation of thin porous silicon by stain etching," *Thin Solid Films*, vol. 9, p. 297, 1997.
- [147] K. Q. Peng, J. J. Hu, Y. J. Yan, Y. Wu, H. Fang, Y. Xu, S. T. Lee, and J. Zhu, J, "Fabrication of Single-Crystalline Silicon Nanowires by Scratching a Silicon Surface with Catalytic Metal Particles," *Adv. Funct. Mater.*, vol. 16, p. 387–394, 2006.
- [148] C.Y. Chen, C. S. Wu, C. J. Chou, and T. J. Yen, "Morphological Control of Single-Crystalline Silicon Nanowire Arrays near Room Temperature," *Adv. Mater.*, vol. 20, p. 3811–3815, 2008.
- [149] J. C. Huang, R. K. Sen, and E. Yeager, "Oxygen Reduction on Platinum in 85% Orthophosphoric Acid," *J. Electrochem. Soc.*, vol. 126, pp. 786-792, 1979.

- [150] S. Gottesfeld, I. D. Raistrick, and S. Srinivasan, "Oxygen Reduction Kinetics on a Platinum RDE Coated with a Recast Nafion Film," *J. Electrochem. Soc.*, vol. 134, pp. 1455-1462, 1987.
- [151] X. H. Cai, K. Kalcher, G. Kolbl, C. Neuhold, W. Diewald, and B. Ogorevc, "Electrocatalytic reduction of hydrogen peroxide on a palladium-modified carbon paste electrode," *Electroanalysis*, vol. 7, p. 340–345, 1995.
- [152] R. Zeis, T. Lei, K. Sieradzki, J. Snyder, and J. Erlebacher, "Catalytic reduction of oxygen and hydrogen peroxide by nanoporous gold," *J. Catal.*, vol. 253, p. 132, 2008.
- [153] C.Q. Lai, H. Cheng, W.K. Choi, C. V Thompson, "Mechanics of Catalyst Motion during Metal Assisted Chemical Etching of Silicon," *J. Phys. Chem. C*, vol. 117, p. 20802–20809, 2013.
- [154] K. Q. Peng, Y. Wu, H. Fang, X. Y. Zhong, Y. Xu, J. Zhu, "Uniform, axial-orientation alignment of one-dimensional single-crystal silicon nanostructure," *Angew. Chem. Int. Ed. Engl.*, vol. 44, p. 2737, 2005.
- [155] C. H. Liu, M. H. Hong, H. W. Cheung, F. Zhang, Z. Q. Huang, L. S. Tan, and T. S. A. Hor, "Bimetallic structure fabricated by laser interference lithography for tuning surface plasmon resonance," *Optics Express*, vol. 16, pp. 10701-10709, 2008.
- [156] "Photoresists, Ancillaries, Etchants, Solvents, and Technical Support for all Stages of Micro Structuring and Lithography.," [Online]. Available: [https://www.microchemicals.com/downloads/application\\_notes.html](https://www.microchemicals.com/downloads/application_notes.html). [Accessed 2018].

- [157] X. Li, "Metal assisted chemical etching for high aspect ratio nanostructures: A review of characteristics and applications in photovoltaics," *Curr. Opin. Solid State Mater. Sci.*, vol. 16, pp. 71-81, 2012.
- [158] F. Es, M. Kulakçı, R. Turan, " An Alternative Metal-Assisted Etching Route for Texturing Silicon Wafers for Solar Cell Applications," *IEEE Journal of Photovoltaics*, vol. 6, pp. 440-446, 2016.
- [159] ASTM G173-03(2012), "Standard Tables for Reference Solar Spectral Irradiances: Direct Normal and Hemispherical on 37° Tilted Surface, Astm.," vol. 3, p. 1–21., 2013.
- [160] L.J. Caballero, "Contact Definition in industrial silicon solar cells," *Solar Energy*, pp. 375-398, 2010.
- [161] L. Tsakalakos, J. Balch, J. Fronheiser, B. A. Korevaar, O. Sulima, and J. Rand, "Silicon nanowire solar cells," *Appl. Phys. Lett.* , vol. 91, p. 233117, 2007.
- [162] G. Coletti, P. C. P. Bronsveld, G. Hahn , W. Warta, D. Macdonald, B. Ceccaroli, K. Wambach, N. L. Quang, and J. M. Fernandez, "Impact of Metal Contamination in Silicon Solar Cells," *Adv. Funct. Mater.*, vol. 21, p. 879–890, 2011.
- [163] J. R. Davis, A. Rohatgi, R. H. Hopkins, P. D. Blais, P. Rai-Choudhury, J. R. McCormick, and H. C. Mollenkopf, "Impurities in silicon solar cells," *IEEE Trans. Electron. Devices*, vol. 27, p. 677, 1980.
- [164] K. Graff, *Metal Impurities in Silicon-Device Fabrication*, Springer, Revised Edition, 1999.
- [165] A. Seeger, K. P. Chick, "Diffusion Mechanisms and Point Defects in Silicon and Germanium," *Phys. Stat. Sol.*, vol. 29, pp. 455-542, 1968.

- [166] D. L. Kendall, "In Semiconductors and Semimetals, Vol. 4, ed. R.K Willardson, A. C. Beer," *New York: Academic*, no. 3, p. 163, 1968.
- [167] R. L. Longini, "Rapid zinc diffusion in gallium arsenide," *Solid-State Electron*, vol. 5, p. 127, 1962.
- [168] F. C. Frank, D. Turnbull, "Mechanism of Diffusion of Copper in Germanium," *Phys. Rev.*, vol. 104, p. 617, 1956.
- [169] U. Gösele, W. Frank, A. Seeger, "Mechanism and Kinetics of the Diffusion of Gold in Silicon," *Appl. Phys.*, vol. 23, pp. 361-368, 1980.
- [170] H. Frank, U. Gösele, H. Mehrer, A. Seeger, "In Diffusion in Crystalline Solids, ed. G. E. Murch, A. S. Nowick," *New York: Academic*, vol. 2, p. 64, 1984.
- [171] W. R. Wilcox, T. J. LaChapelle, D. H. Forbes, "Gold in silicon: effect on resistivity and diffusion in heavily-doped layers," *J. Electrochem. Soc.*, vol. 111, pp. 1377-1380, 1964.
- [172] N. A. Stolwijk, B. Schuster, J. Holzl, H. Mehrer, W. Frank, "Diffusion and solubility of gold in silicon," *Physica B*, vol. 116, p. 335, 1983.
- [173] N. A. Stolwijk, B. Schuster, J. Hölzl, "Diffusion of gold in silicon studied by means of neutron-activation analysis and spreading-resistance measurements," *Applied Physics A*, vol. 33, pp. 133-140, 1984.
- [174] J. Hauber, N. A. Stolwijk, L. Tapfer, H. Mehrer, W. Frank, "U- and W- shaped diffusion profiles of gold in silicon," *J. Phys. C: Solid State Phys*, vol. 19, pp. 5817-5836, 1986.
- [175] F. Morehead N. A. Stolwijk, W. Meyberg, and U. Gösele, "Self-interstitial and vacancy contributions to silicon self-diffusion determined from the diffusion of gold in silicon," *Appl. Phys. Lett.*, vol. 42, p. 690, 1983.

- [176] W. R. Wilcox and T. J. LaChapelle, "Mechanism of Gold Diffusion into Silicon," *Journal of Applied Physics*, vol. 35, p. 240, 1964.
- [177] D. Yang, R. Yang, J. Zhang, Z. Yang, S. Liu and C. Li, "High efficiency flexible perovskite solar cells using superior low temperature TiO<sub>2</sub>," *Energy Environ. Sci.*, vol. 8, pp. 3208-3214, 2015.
- [178] J. H. Seo, H.-D. Um, A. Shukla, I. Hwang, J. Park, Y.-C. Kang, C. S. Kim, M. Song, and K. Seo, "J. H. Low-Temperature Solution-Processed Flexible Organic Solar Cells with PFN/AgNWs Cathode," *Nano Energy*, vol. 16, pp. 122-129, 2015.
- [179] K. Yoo, J. Y. Kim, J. A. Lee, J. S. Kim, D. K. Lee, K. Kim, J. Y. Kim, B. Kim, H. Kim, W. M. Kim, J. H. Kim, and M. J. Ko, "Completely transparent conducting oxide-free and flexible dye-sensitized solar cells fabricated on plastic substrates," *ACS Nano*, vol. 9, pp. 3760-3771, 2015.
- [180] "Silicon Valley Microelectronics," [Online]. Available: <https://www.svmi.com/wafer-services/wafer-thinning/>. [Accessed 1 December 2018].

## CURRICULUM VITAE

### PERSONAL INFORMATION

Surname, Name : Baytemir, Gülsen  
Nationality : Turkish (TC)  
Date and Place of Birth : 8 July 1985, Ankara  
Phone : +90 312 210 43 31  
E-mail : baytemir@metu.edu.tr

### EDUCATION

| <b>Degree</b> | <b>Institution</b>                   | <b>Year of Graduation</b> |
|---------------|--------------------------------------|---------------------------|
| MS            | METU Physics                         | 2011                      |
| BS            | METU Physics                         | 2009                      |
| High School   | Süleyman Demirel High School, Ankara | 2003                      |

### WORK EXPERIENCE

| <b>Year</b>  | <b>Place</b>  | <b>Enrollment</b>         |
|--------------|---|---------------------------|
| 2017-Present | Center for Solar Energy Research and Applications (GUNAM)                                       | Scientific Project Expert |
| 2015-2016    | School of Electrical, Computer and Energy Engineering, Arizona State University                 | Visiting Scholar          |
| 2010-2017    | METU Department of Physics  | Research Assistant        |
| 2009-2010    | Department of Electrical and Electronics Engineering, Atılım University                         | Teaching Assistant        |
| 2008 Summer  | Sarayköy Nuclear Research and Education Center (SANAEM), Turkish Atomic Energy Authority (TAEK) | Intern                    |

## FOREIGN LANGUAGES

Advanced English, Basic German

## PUBLICATIONS

1. F. Es, G. Baytemir, M. Kulakci and R. Turan “Metal-assisted nano-textured solar cells with SiO<sub>2</sub>/Si<sub>3</sub>N<sub>4</sub> passivation” *Solar Energy Materials & Solar Cells* 160 269–274 (2017), <https://doi.org/10.1016/j.solmat.2016.10.032>
2. G. Baytemir, F. Es, A. S. Alagoz and R. Turan “Radial junction solar cells prepared on single crystalline silicon wafers by metal-assisted etching” *Phys. Status Solidi RRL*, 11: n/a, 1600444 (2017), doi:10.1002/pssr.201600444
3. *The above article was selected and published as the cover page of the journal. Phys. Status Solidi RRL*, 11: n/a, 1770326 (2017), doi:10.1002/pssr.201770326
4. F. Es, G. Baytemir, M. Kulakci and R. Turan “Multi-crystalline silicon solar cells with metal-assisted nano-texturing using HNO<sub>3</sub> as hole injection agent” *Phys. Status Solidi RRL*, 10: 866–869 (2016), doi:10.1002/pssr.201600245
5. S. H. Altinoluk, H. E. Ciftpinar, O. Demircioglu, F. Es, G. Baytemir, O. Akar, A. Aydemir, A. Sarac, T. Akin, and R. Turan, “Light Trapping by Micro and Nano-hole Texturing of Single-crystalline Silicon Solar Cells”, *Energy Procedia* 92, 291-296 (2016), <https://doi.org/10.1016/j.egypro.2016.07.081>
6. G. Baytemir, Y. Sarac, O. Yilmaz, “Kappa K+pi (-) vertex in light cone QCD sum rules”, *Phys. Rev. D* 81 094009 (2010), <https://doi.org/10.1103/PhysRevD.81.094009>
7. V. Takaloo, F. Es, G. Baytemir, and R. Turan, "Nickel-assisted Chemical Etching for Multi-crystalline Si Solar Cell Texturing: A Low-Cost Single Step Alternative to Existing Methods" *Materials Research Express* 5 7 (2018). doi:10.1088/2053-1591/aaceec



8. G. Baytemir, F. Es and R. Turan, “Comparison of Influence of Gold Impurities on the Performances of Planar and Radial Junction c-Si Solar Cells” Manuscript submitted.

9. F. Es, E. Semiz, E. Orhan, E. Genç, G. Kökbudak, G. Baytemir and R. Turan, “Optimization of PERC Fabrication Based on Loss Analysis in Industrially Relevant Environment: First Results from GÜNAM Photovoltaic Line (GPVL)” Manuscript submitted.

## **CONFERENCES/ PRESENTATIONS**

### ***Oral Presentation***

1. NanoTR-12, 12th Nanoscience and Nanotechnology Conference, Gebze, Turkey G. Baytemir, F. Es, and R. Turan “Radial Junction Solar Cells Prepared on Crystalline Si by Metal Assisted Electroless Etching”, June 2016.

### ***Poster Presentation***

1. E-MRS European Materials Research Society, 2017 Fall Meeting, Warsaw, Poland. G. Baytemir, F. Es, and R. Turan, “Radial Junction Solar Cells on Low Quality wafers”, September 2017

2. PVSEC-26, the 26th International Photovoltaic Science and Engineering Conference, Singapore. G. Baytemir, F. Es, and R. Turan, “Radial Junction Crystalline Silicon Solar Cells by Metal assisted Etching”, October 2016.

3. MRS Materials Research Society, 2016 Spring Meeting, Phoenix, Arizona, USA. S. H. Altinoluk, H. E. Ciftpinar, O. Demircioglu, F. Es, G. Baytemir, O. Akar, A. Aydemir, A. Sarac, T. Akin, and R. Turan, “Light Trapping by Micro and Nano-hole Texturing of Single-crystalline Silicon Solar Cells”, April 2016.

4. 30<sup>th</sup> EU PVSEC, 30th European PV Solar Energy Conference and Exhibition, Hamburg, Germany. G. Baytemir, F. Es, and R. Turan, “Radial Junction Solar Cells by Metal Assisted Etching”, September 2015.

5. 29<sup>th</sup> EU PVSEC, 29th European PV Solar Energy Conference and Exhibition, Amsterdam, Netherlands. F. Es, E. H. Ciftpinar, G. Baytemir, E. Ozkol, O. Demircioglu, M. Gunoven, M. Kulakci, and R. Turan, “Nano-Hole Texturing of Multi-Crystalline Silicon Solar Cells”, September 2014.

### **MEMBER OF ORGANIZING COMMITTEE**

1. SolarTR3, Third Turkish Solar Electricity Conference and Exhibition. Ankara, Turkey, April 2015.

2. SolarTR2, Second Turkish Solar Electricity Conference and Exhibition. Antalya, Turkey, November 2012.

3. PV School 2016, International Summer School and Workshop on Photovoltaic Science and Technology, Ankara, Turkey, June 2016.

4. PVCon 2018, International Conference on Photovoltaic Science and Technologies, Ankara, Turkey, July 2018 (<http://pvcon.org/>)

### **HOBBIES**

Dancing, Singing, Movies, Theatre